



HAL
open science

Enregistrement d'Image Déformable en Groupe pour l'Estimation de Mouvement en Imagerie Médicale en 4D

Evgenios Kornaropoulos

► **To cite this version:**

Evgenios Kornaropoulos. Enregistrement d'Image Déformable en Groupe pour l'Estimation de Mouvement en Imagerie Médicale en 4D. Autre. Université Paris Saclay (COMUE), 2017. Français. NNT : 2017SACLC042 . tel-01617929v2

HAL Id: tel-01617929

<https://theses.hal.science/tel-01617929v2>

Submitted on 17 Oct 2017

HAL is a multi-disciplinary open access archive for the deposit and dissemination of scientific research documents, whether they are published or not. The documents may come from teaching and research institutions in France or abroad, or from public or private research centers.

L'archive ouverte pluridisciplinaire **HAL**, est destinée au dépôt et à la diffusion de documents scientifiques de niveau recherche, publiés ou non, émanant des établissements d'enseignement et de recherche français ou étrangers, des laboratoires publics ou privés.

NNT : 2017SACL042

THESE DE DOCTORAT
DE
L'UNIVERSITE PARIS-SACLAY
PREPAREE A
CENTRALESUPELEC

ÉCOLE DOCTORALE N°580
Sciences et Technologies de l'Information et de la Communication
Spécialité de doctorat : Mathématiques & Informatique

Par

M. Evgenios N. Kornaropoulos

Enregistrement d'Image Déformable en Groupe pour l'Estimation de
Mouvement en Imagerie Médicale en 4D

Thèse présentée et soutenue à Châtenay-Malabry, le 20 Juin 2017 :

Composition du Jury :

M Charles A. Cuenod	Professeur, Université Paris Descartes	Président du jury
M Dimitris Samaras	Maître de conférences, Université de Stony Brook	Rapporteur
M Hugues Talbot	Professeur, Université Paris-Est - ESIEE	Rapporteur
Mme Evangelia I. Zacharaki	Maître de conférences, Université de Patras	Examineur
Mme Celine Hundelot	Maître de conférences, CentraleSupélec	Examineur
M Alain Rahmouni	Professeur, Hôpitaux Universitaires Henri Mondor	Examineur
M Nikos Paragios	Professeur, CentraleSupélec	Directeur de thèse

Dedication

Ο άνεμος θα καίει στη γη του Νείλου
μια αρχαία μυρωδιά θα μας μεθά
στον τροπικό όπως θα 'σαι του Καρκίνου
μέσα σου θα γεννιέται μια θεά

*To this motivational drive,
to Elina*

Acknowledgements

First of all I would like to thank my supervisor, Prof. Nikos Paragios, for giving me the opportunity to pursue my research and for his consistent guidance and support throughout my PhD. Then I would like to thank my main collaborator in the last year and a half of my PhD, Dr. Evangelia I. Zacharaki, who couldn't have been a better mentor for me and whom I thank for showing faith in me. Her hard work, working mentality and discipline have always been very inspiring for me.

My warm thanks to Prof. Rahmouni, Dr. Lin and M. Pierre Zerbib for providing me with the medical data, for devoting part of their precious time to discuss with me during my visits to the Centre Hospitalo-Universitaire Henri Mondor, and for responding to all my questions and requests regarding the medical part of my research during the course of my PhD. I would also like to thank my reviewers Prof. Samaras and Prof. Tulbot for spending their valuable time for reviewing my thesis and providing useful comments and suggestions. I would also like to thank Prof. Cuenod and Prof. Hudelot for their role as an examiner. It was wonderful and insightful to have them all as my thesis committee members.

My thanks also go to my former academic supervisors, Prof. Gurcan and Dr. Niazi from Ohio State University, and Dr. Grammalidis from the Centre for Research and Technology (CERTH), Hellas for encouraging me to apply to the specific PhD position in Ecole Centrale de Paris. I would also like to thank my funding agency, the ANR (Agence Nationale de la Recherche): ERC Grant ADAMANTIUS.

I am grateful to all my lab mates (present and past) for providing their selfless support and their presence whenever needed. Specially, I would like to thank my office-mates, Enzo and Puneet, for being so helpful and friendly in the beginning of my stay in Paris and for plenty of technical discussions ever since, Eugene for listening to me and being such a great friend all these four years, Dimitris, Grigoris and Stavros (the pious), for being that nice and fun colleagues, Stavros (the tall) for giving me his feedback on my first results in my research, Maxim and Hari for the discussions we had over numerical analysis, Maria, the Latex guru of the lab, for helping me fixing the format of the manuscript of my first publication, Siddhartha and Mihir for helping me solving some technical issues arising here and there and Rafael for teaching me many programming tricks. My special thanks to

Natalia (CentraleSupélec), Carine (CentraleSupélec) and Alexandra (INRIA) for helping me out with infinitely many French administrative formalities. I am afraid that without their help I would have spent most of my time dealing with paper works.

I would like to thank my gang in Paris, Christo, Gianni, Christina, Elvis, Angie, Maro, Nikola, Ioanna and Foti for all the fun, full of music and dancing moments we have shared, for being there for me when needed and for following me to my crazy traveling plans in the French countryside and beyond. My very special thanks to Elina for everything she's done for me, among which helping me with the translation of the abstract of my thesis from english to french.

Above all, I would like to deeply thank my family, my parents, Niko and Eleni and my brother Michali for their unconditional love and for their faith in me, even when I was doing something quite unconventional.

Contents

List of Figures	ix
List of Tables	xv
1 Introduction	1
1.1 Context	2
1.2 Medical Image Registration	3
1.3 Statement	14
1.4 Background on Diffusion-Weighted MRI	15
1.5 Roadmap	17
1.6 Publications	19
2 Group-wise Medical Image Registration: A Literature Review	21
2.1 Geometric	26
2.2 Iconic	30
2.3 Hybrid	38
2.4 Methods based on Attribute Vectors	38
2.5 Discussion	39
3 Deformable Group-wise Registration Using a Physiological Model: Application to Diffusion-Weighted MRI	43
3.1 Prior Work	45
3.2 Proposed Method	48
3.3 Experimental Validation	56
3.4 Discussion	58
4 Joint Deformable Registration and Diffusion Estimation	59
4.1 Prior Work	61
4.2 Proposed Method	64
4.3 Experimental Validation	73
4.4 Discussion	77

5	Extraction of DW-MR Imaging Biomarkers through the Proposed Registration Methods	79
5.1	Prior Work	80
5.2	ADC Calculation based on a Physiological Model	81
5.3	Results	84
5.4	Discussion	90
6	Conclusion	95
6.1	Contributions	95
6.2	Future Work	96
	Bibliography	99

List of Figures

- 1.1 **Deformable pair-wise image registration [53].** *Left image:* Overlapping between the source (I) and target (J) images, before registration. As it can be observed, the alignment between the images is not perfect. *Right image:* Overlapping between the deformed source image and the target, after registration. The deformable registration algorithm recovered a deformation field $T(x)$ that was applied to the source image, in order to align them. 5

- 1.2 **Discrete labelling in deformable image registration [53].** Different type of sampling strategies for the discrete label space used for image registration: sparse (left image) and dense (right image). Note that every label in this formulation corresponds to a displacement vector (in orange). 9

- 1.3 **Deformation grid superimposed on an image [53].** Deformable registration is formulated as a discrete labeling problem on a grid-graph, superimposed to the source 2D image. The nodes of the graph correspond to the variables of a Markov Random Field, and model the control points of a FFD. The space of plausible deformations is explored by choosing different labelings. 10

- 1.4 **Diffusion of water molecules [95].** *Left image:* This is a drawing of restricted diffusion. Drawing represents 1 voxel of tissue evaluated by Diffusion-Weighted Imaging (DWI) containing cells and blood vessel. The black circles with arrows represent the water molecules within extracellular space, intracellular space, and intravascular space, all of which contribute to measured MR signal. There are two causes of the restriction. One cause is the observed high cellularity, which results into a reduced extracellular space. Moreover the cell membranes are intact, thus they act as barrier to water movement. *Right image:* This is a drawing of free diffusion. Here we observe low cellularity and defective cell membranes. In less cellular environment, relative increase in extracellular space allows freer water diffusion than more cellular environment would. Defective cell membranes also allow movement of water molecules between extracellular and intracellular spaces. 15
- 1.5 **Tissue characterization by diffusion-weighted images [95].** Three diffusion-weighted MR images in 55-year-old man with liver metastasis obtained at different b-values. The patient large heterogeneous metastasis within right lobe of liver. Necrotic center of metastasis (squares) shows attenuation of signal intensity with increasing b-values, indicating less restricted diffusion. By comparison, rim of tumor (rectangles) is more cellular and shows little signal attenuation with increasing b-value. 16
- 1.6 **Apparent diffusion coefficient (ADC) [95].** *Left image:* This simplified schematic shows derivation of ADC. Logarithm of relative signal intensity is plotted on y-axis against values on x-axis. Slope of line fitted through plots is ADC. In this example, slope of line (ADC) is smaller for tumor (*gray line*) than for normal liver (*black line*). *Central and right image:* Here we show a tumor area with low ADC (*gray outline*, which is darker than normal liver with higher ADC values (*black outline*). One can notice that contrast on ADC map is opposite of that seen on diffusion-weighted image. On diffusion-weighted image, tumor showed less signal attenuation and appeared higher signal intensity than normal liver. Both those two images are obtained from the same patient as in Figure 1.5. 18

- 2.1 **Examples of the different approaches in terms of the reference frame in 4D medical image registration.** *Upper-left image:* An example of the eulerian approach followed by De Craene et al. [46] to register a sequence of 3D-US images of the same patient. In that way, the large transformations between remote images in the sequence (denoted by a red arrow) are decomposed as a chain of small and smooth deformations. *Upper-right image:* An example of a G2R lagrangian approach, in which all the 3D MR cardiac images of the sequence are registered to a pre-selected one (the first image of the sequence in this example corresponding to the end-diastolic frame), which acts as the reference frame [121]. *Lower-left image:* An example of a second G2R lagrangian approach in which the reference frame to which all the MR brain images are co-registered is an atlas (generated template) [45]. *Lower-right image:* An example of an IRG group-wise registration with an unknown reference (consensus) space, proposed by Wu et al. [233]. All subjects in the group are connected by the forward transformations g_i (i.e., red solid arrows) to the common space (i.e., a purple circled region), and the backward transformations (i.e., blue dashed arrows) from the common space. The right panel shows how to transform between subjects S_i and S_j 22
- 2.2 **Illustration of the different approaches of spatiotemporal smoothness [138].** *Left image:* B-spline grid with spatiotemporal smoothness. *Central image:* cyclic B-spline grid with spatiotemporal smoothness. *Right image:* B-spline grid with only spatial smoothness. All three schemes can be used in reference time point, consecutive time point (eulerian) and groupwise registration approaches. In the cyclic version, the grid points at the temporal border (open nodes) are direct neighbors. . . . 23
- 2.3 **Illustration of the stack of images used as an input to the "empirical" entropy, which is the objective function in the congealing approach [112].** A pixel stack is a collection of pixels drawn from the same location in each of a set of N images. Here, the i,h pixel from each of six images forms a pixel stack. Since half of the pixels are black and half are white, this corresponds to a Bernoulli random variable with parameter $p = 0.5$. The entropy of such a random variable is 1 bit. 30

-
- 3.1 **Representation of the edges of our proposed MRF-based group-wise registration scheme.** The node and the edge system of all the connected graphs. With brown color we represent the relationship within the grid nodes belonging to each of the deformation fields (intra connections). Finally, the pink edges denote the temporal relationship (which can be either of high-order or a pair-wise connection) between successive deformation fields (inter relationship). 52
- 3.2 **DW images of a patient from the dataset.** An axial slice of the 3D image of a patient, with b values of 50, 400 and 800 s/mm^2 (from left to right). The red contour in the b-value=50 image corresponds to the tumor's contour, as it was drawn by the expert. 56
- 3.3 **Results on three different criteria for validating each method, applied on DW images.** *First row:* Boxplots of statistics (mean) of SSE by fitting the physiological model, MI and NCC respectively. *Second row:* ADC map (same axial slice as in figure 3.1) derived without registration and with the examined registration methods. 57
- 4.1 **The node and the edge system of all the connected graphs.** With green and brown color the relationship within the grid nodes belonging to ADC and each of the deformation field respectively (intra connections). The blue dotted edge represents the dependencies among deformation field and appearance model (coupling relationship), whereas pink edges denote the temporal relationship between successive deformation fields (inter relationship). 68
- 4.2 **The image processing pipeline.** Circles demonstrate each of the computations performed towards computing an ADC map with motion correction. In NoReg case, apparently no registration occurred, therefore the original rather than a deformed version of the DWI sequences was inputted to the diffusion model to compute the \tilde{z}_c or \tilde{z}_v map. 71
- 4.3 **Real data.** An axial slice of the 3D image of a patient, with b values of 20, 50, 150, 400 and 800 s/mm^2 (from left to right). . 73
- 4.4 **Simulated data** An axial slice of the simulated 3D images of the same patient as in the above figure. The very left image is the corresponding slice from the simulated ADC map, whereas next to it from left to right are the slices of the simulated images of b values of 50, 150, 400 and 800 s/mm^2 ("b 20" image was used to simulate the diffusion process). 73

- 4.5 **The SSE with simulated data on retrieved deformation fields and ADC map.** Box plots across population of the average euclidean distance over the DWI sequence size between simulated deformation fields and the inverse deformation fields derived by the examined method (left image) and the SSE between the simulated z_c image and the corresponding one calculated based on registered by the different methods simulated DWI sequences. \tilde{z}_c and \hat{z}_c are the maps compared against the simulated z_c image for the case of JointRef1 and all the rest registration methods respectively. The specific results were acquired using 3 b-values. 75
- 4.6 **Error bars with simulated data on retrieved deformation fields and ADC map over number of b-values.** Same results as in figure 4.5, this time averaged over the entire population and plotted over the size of the DWI sequence (number of b-values). 75
- 4.7 **The fitting error on the physiological model with real data.** Box plots of the (voxelwise computed) mean sum-squared fitting error (left) and each standard deviation (right) across population. The specific results were acquired using 3 b-values in each case. 75
- 4.8 **Error bars over b-values with real data (fitting error on the physiological model)** Plots of the corresponding results in figure 4.7 over the size of the DWI sequence (number of b-values), in which the plot is coloured differently based on the post-processing scenario. 76
- 4.9 **Computed ADC maps by applying each of the examined methods.** Same axial slice of the \tilde{z}_c ADC map derived by equation 4.4 in case of NoReg and equation 4.20 for all the examined registration methods, except the proposed one, JointRef1 (bottom-right), which was computed explicitly by the joint formulation (\hat{z}_c). The red contour on the first image (up-left) denotes the tumor of the patient, delineated by an expert. . . 76
- 5.1 **The overall classification accuracy for each of the examined methods, over the number of b-values.** 85

5.2 **Plots of the mean RMSE of predicting Deauville scores.** In the left we plot the results for predicting $D_{2cycl,real}$. In the middle we plot the results of predicting $D_{end,real}$ using as feature combination the mean value in the tumor region a \mathbf{z}_c image, together with the change of mean in the same image from the onset of the treatment until its end, as well and change in mode of a \mathbf{z}_v image again from the from the onset of the treatment until its end. Finally in the right plot we show the results of predicting $D_{end,real}$, this time using as a feature combination the change in kurtosis and skewness of the histogram computed in the tumor region in a \mathbf{z}_v image, from the study after 2 cycles of therapy until the end of treatment. 90

5.3 **Plots of the R^2 value when predicting Deauville scores.** In the left we plot the results for predicting $D_{2cycl,real}$. In the middle we plot the results of predicting $D_{end,real}$ using as feature combination the mean value in the tumor region a \mathbf{z}_c image, together with the change of mean in the same image from the onset of the treatment until its end, as well and change in mode of a \mathbf{z}_v image again from the from the onset of the treatment until its end. Finally in the right plot we show the results of predicting $D_{end,real}$, this time using as a feature combination the change in kurtosis and skewness of the histogram computed in the tumor region in a \mathbf{z}_v image, from the study after 2 cycles of therapy until the end of treatment. 90

List of Tables

2.1	Group-wise registration (inter – subject) methods for brain atlas construction or assessing diseases on the brain	25
2.2	Automatic organ segmentation based on group-wise registration (inter – subject or atlas – subject)	25
2.3	Group-wise registration (intra – subject) methods for a quantitative analysis of deformable organs	26
2.4	Group-wise methods following an IRG approach	38
4.1	Comparative information on the examined registration methods. Since NoReg is not a method rather than a "scenario", only its additional features (ADC maps computed without registration) are mentioned.	71
5.1	Classification results on patients with HD and NH type of lymphoma, derived by the examined methods using 3 b-values. All the results were derived by the LDA-based classifier in a supervised manner.	85
5.2	Statistical features yielding the highest correlation scores with tumor staging after two cycles of chemotherapy (D_{2cycl}), shown along with their p -values, for the case of each method (change in 75 percentile of tumor region’s histogram in z_c for NoReg and change in kurtosis of tumor region’s histogram in z_v for JointRef1). The last two columns show the correlation between the corresponding predicted Deauville scores using the specific diffusion-based features and the real Deauville scores for the patients.	88
5.3	Results on prediction of Deauville scores after 2 cycles of chemotherapy (D_{2cycl}). Corr.score corresponds to the correlation between predicted staging scores and actual PET-based ones. RMSE stands for root mean squared error after applying linear regression between the values of the mentioned features and Deauville scores, while R^2 corresponds to the coefficient of determination. These results were derived using 4 b-values.	88

-
- 5.4 Statistical features yielding the highest **correlation scores with tumor staging in the end of the treatment** ($D_{end,real}$), shown along with their p -values. The last two columns again show the correlation between the corresponding predicted Deauville scores using the specific diffusion-based features and the real Deauville scores for the patients. 88
- 5.5 Results on **prediction of Deauville scores in the end of treatment** (D_{end}). As in table 5.3, Corr.score corresponds to the correlation between predicted staging scores and actual PET-based ones. RMSE stands for root mean squared error after applying linear regression between the values of the mentioned features and Deauville scores, while R^2 corresponds to the coefficient of determination. Change-1 corresponds to the change in the values between the onset and the end of the treatment, while change-2 corresponds to the change between the study after two cycles and the end of the treatment. These results were derived using 4 b-values. 88

Chapter 1

Introduction

The present work lies at intersection of Medical Image Analysis and Computer Vision. It examines the problem of *motion estimation*, which is a significant challenge in 4D medical imaging (4DMI) and 4D radiation therapy (4DRT). In the former process multiple 3D images of a patient are acquired over time prospectively or retrospectively, in order for the patient motions and changes to be monitored and studied. 4DMI includes volumetric over time CT, MRI, PET, PET/CT, SPECT and US imaging. 4DRT on the other hand, aims to track and compensate for target (lesion) motion during radiation treatment, minimizing normal tissue injury, especially in critical structures adjacent to the target, and/or maximizing radiation dose to the target. Besides possible patient motion, involuntary organs' motion is inevitably present in these processes, producing artifacts and uncertainties in target identification, delineation, and localization.

Manual motion estimation, that would lead to motion correction, from a time series of images is impractical, as it consists of a tedious task. Corresponding landmark positions in time need to be determined and depending on the application of interest the number of required landmarks may be very large. Image registration methods are often applied to automate this process. In case of 4DMI, the goal of an image registration method would be to establish accurate dense spatial correspondences among successive images of the same subject acquired over time and in that way align (ideally simultaneously) all the images into a consensus space. Such an image registration method is characterized as group-wise. Prior knowledge on the way the shape of an organ and/or its appearance profile change(s) over time should be also taken into account during registration. Specifically, due to non-linear physiological motion, non-linear alignment of the images in the sequence becomes necessary, a problem referred to as *deformable image registration*. Along with image segmentation, deformable image registration to directly measure or compensate for local tissue motion, is still one of the most important problems in the field of image processing. The problem becomes even more challenging when a sequence instead of a pair of images

needs to be co-registered simultaneously, as in the case of motion estimation in 4DMI.

In this introductory chapter, we first give a brief description of the context of this work, followed by an introductory section on medical image registration (1.2). Next in section 1.3, after having introduced the main challenges posed by the current technological and methodological advances, we present the main ideas of this work. Then in section 1.4 the medical problem, that motivated the research presented in this thesis, is briefly described. Finally, section 1.5 gives an overview of the work done in the context of this thesis.

1.1 Context

In 4DMI a fourth dimension is introduced beyond the 3D space, which is the time dimension. In this fourth dimension, patient motion and change are recorded. Historically, the time dimension was incorporated into 3D medical imaging through the application of respiration gating soon after the 3D imaging technique was invented and long before the fast 3D imaging techniques with sufficient temporal resolution were available [174, 77, 52, 228, 102, 105]. Then the concept of 4DRT was introduced [186, 184, 119] with the availability of 4D imaging. The span of applications of 4DMI stretches from correcting motion artifacts, studying internal organ motion, and providing clinically meaningful quantitative volumetric image information by pharmacokinetic or physiological models for radiological diagnosis, to treatment planning and treatment delivery in 4DRT [116]. It is by considering this extreme variety of applications that one can understand the importance of 4DMI in medical research and clinical practice. Investigating its limitations and coping with the challenges that have arisen on improving its accuracy, will help in making 4DMI a powerful imaging tool applied efficiently in clinical practice.

The main challenge gradually recognised by researchers working on advancing 4D imaging and 4D conformal radiation therapy techniques is to tackle the effects of organs' motion, mainly due to cardiac motion, respiration, peristaltic motion, digestion, and muscular motion [228, 208, 105]. Due to motion, anatomical structures in consecutive images are misaligned. Various techniques have been developed over the years and implemented in clinical practice, that involve physical intervention, including patient immobilization, breath holding, active breathing control (ABC), breath coaching, as well as real-time intervention by the user (radiologist), such as respiratory gating and respiratory motion tracking, towards removing such motion artifacts. Even if these techniques have enhanced the performance of 4DMI, they were never adequate for achieving high-fidelity images.

Towards this scope, image processing becomes necessary. More specifically, a vast amount of work on developing deformable image registration

methods, that incorporate in their framework mathematical and statistical models that model organs' motion and image intensity variation, has been emerged over the years [175]. Currently however, deformable image registration may have some distance to go before it can be routinely used in the clinic, due to its long iterative optimization (taking several hours) and the difficult validation process.

Among the various modalities included in 4DMI, this work deals with volumetric over time (4D) MRI. MRI can be acquired with different contrast weightings and together these images provide information about the anatomy, function and pathology. Such a piece of information is provided through the computation of parametric maps, that depict meaningful physical or chemical variables that characterize the physical or chemical processes taking place during image acquisition. The values of these variables or so-called quantitative parameters are estimated by fitting a parametric pharmacokinetic or physiological model to a series of contrast-weighted images. These values are estimated in physical units, allowing thus for comparisons between tissue regions and among subjects. Such maps increase the sensitivity of clinical MRI in detecting pathology, by allowing the comparison of measurements in a single subject with normative values acquired in a healthy population, as well as monitoring subtle changes caused by the progression or remission of disease [158]. Examples are Diffusion Tensor MRI (DTI), Dynamic Contrast-Enhanced MRI (DCE-MRI), MR relaxometry (T1 and T2 mapping) and Diffusion-Weighted MRI (DWI). Any parametric model assumes that the same tissue is present at a specific voxel in each of the images. If this is not the case, estimation of the tissue parameters will be corrupted. Therefore, aligning the images prior to parameter estimation is necessary and for this purpose image registration techniques can be employed.

1.2 Medical Image Registration

Image registration is the process of finding the optimal transformation that aligns different imaging data into spatial correspondence, so that after registration, the same anatomic structures occupy the same spatial locations in different images. In general, two or more images are considered. It is a problem that has been studied a lot over the past few decades, as it consists of the building block for a variety of medical image analysis tasks. Image registration methods had been classified by Maintz and Viergever in their influential article of 1998 [130], with the following criteria: (i) dimensionality (spatial or spatiotemporal 2D to 2D, or 2D to 3D, or 3D to 3D), (ii) nature of the registration basis (extrinsic, intrinsic, non-image based), (iii) nature of the transformation (rigid, affine, projective, curved), (iv) domain of the transformation (global, local), (v) degree of interaction (interactive, semi-

automatic, automatic), (vi) optimization procedure (parameters computed or searched for), (vii) modalities involved (mono-modality, multi-modality, modality to model, patient to modality), (viii) subjects involved (intra-subject, inter-subject, atlas), and (ix) objects involved (e.g., brain, heart, breast). Interestingly, the classification of the field introduced in that article is still usable, although some changes have occurred since then.

The main change has been the shift from extrinsic to intrinsic registration. The approach of placing external reference points (fiducial markers), introduced into the images space in identical relationship to patient anatomy, is hardly found anymore and it characterizes only a restricted number of applications, as it often lacks of reliability and induces concomitant errors. The vast majority of the image registration methods nowadays are intrinsic methods that rely on the patient image data only, thus allowing retrospective co-registration. In this doctoral thesis, we are examining only methods classified as intrinsic ones. Furthermore, intensity-based registration methods have gained the primacy among the landmark-based or the surface-based, which were the most often used type of intrinsic registration at that time. Computational hurdles to applying voxel-based registration have rapidly diminished and therefore the full image contents are taken into account instead of relying on segments of image objects that subsequently have to be aligned. Moreover, other worth-mentioning changes since that early literature review is the progress of inter-subject registration and the availability of generic image registration software packages. Other general reviews of the field may be found in [28, 76, 201, 249, 94, 188, 2]. These surveys and reviews deal mostly with 3D to 3D or 2D to 2D image registration. For a survey on slice-to-volume mapping (2D to 3D registration) we refer the interested reader to the thesis of Enzo Ferrante [53].

This section, which consists of an introduction to medical image registration, is divided following the standard structural separation of registration algorithms in three components: (i) a transformation model; (ii) an objective function; and (iii) an optimization strategy.

1.2.1 Transformation Model

The most fundamental characteristic of any image registration method is the type of spatial (or spatio-temporal in case of time-evolved or longitudinal sequences) geometric transformation or mapping needed to properly co-register and align the images. The choice of the geometric transformation is of great importance, especially for the group-wise registration process is due to the fact that it affects the computational efficiency and the richness in terms of description of the method; a good compromise between these two issues is always opted. The transformation model reflects the class of transformations that are desirable or acceptable, and therefore limits the

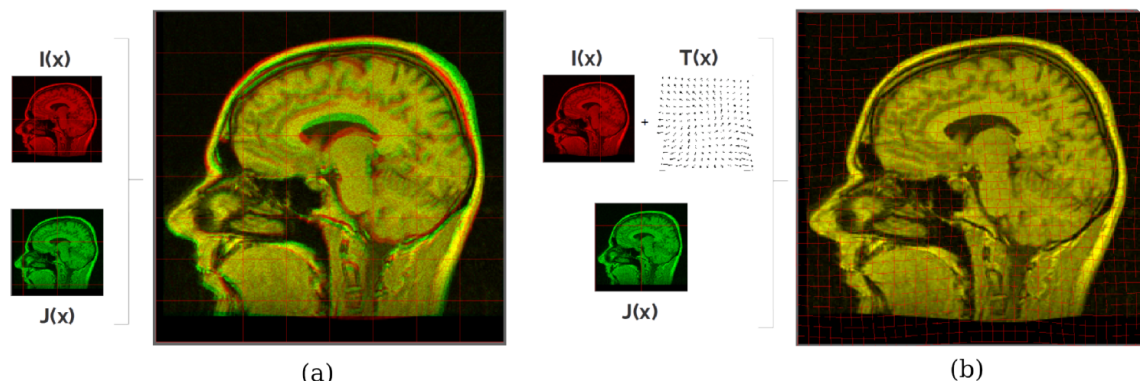


Figure 1.1: Deformable pair-wise image registration [53].

Left image: Overlapping between the source (I) and target (J) images, before registration. As it can be observed, the alignment between the images is not perfect. *Right image:* Overlapping between the deformed source image and the target, after registration. The deformable registration algorithm recovered a deformation field $T(x)$ that was applied to the source image, in order to align them.

solution to a large extent. Transformation models are often characterized by their degrees of freedom, or in other words, the number of parameters the registration estimates through the optimization strategy. Two basic models can be discriminated, rigid and non-rigid transformations. In case of deformations, which belong to the non-linear (non-rigid) class of transformations, they can be further classified according to their theoretical basis [188].

Rigid

The original focus of image registration had predominantly been on correcting for rigid-body motion of brain image volumes acquired at different scanning sessions, often with different modalities. In the "rigid-body" case there are six degrees of freedom (or unknowns) in the 3D transformation: three translations and three rotations. Therefore, they are equivalent to a change from one Cartesian system of coordinates to another one which differs by shift and rotation. The key characteristic of a rigid-body transformation is that the distance between all points in the image is preserved. This kind of transformation model is most of the times applied to longitudinal studies of the brain, as the shape of the human brain changes very little with head movement [196, 247, 166, 217].

Moreover, subject's movement inside the scanner during image acquisition is also considered as a rigid motion. In [183] and [117] a rigid intra-subject alignment of 3D brain images acquired at different (consecutive) time-points is applied as a prior to a non-rigid inter-subject deformation scheme step. The authors note that this step removes variations in patient positioning in the scanner and facilitates the subsequent non-rigid image registration. A rigid groupwise registration approach is also followed in [29] to track the motion of tumors in DCE-MRI sequences, under the assumption that tu-

mors are more rigid than their surrounding tissues, a claim that can be true for solid tumors having higher interstitial pressure than most normal tissues and therefore greater rigidity [147]. That latter assumption though doesn't hold true in case of large tumors. In general, rigid-body registration is preferred in cases where the structures of interest are either bone or are enclosed in bone, as it is the case of the head, and in particular the brain. Rigid body registration is used for other regions of the body in the vicinity of bone (e.g. the neck, pelvis, leg or spine) but the errors are likely to be larger, like in the case of Bidaut and Vallée [21] that applied rigid-body transformation on cardiac dynamic MRI to co-register the images of the sequence. Even if intensity information is used in the framework and the anatomy doesn't change over time (case of intra-subject registration), a simple rigid-body transformation model that assumes only translations isn't an appropriate one for estimating the motion of the heart. As denoted in [41], a rigid registration is not enough in practice to correct for breathing motion. The most convincing reason is the existence of transversal motion.

Non-rigid

The advent of dedicated longitudinal and cross-sectional brain studies soon necessitated the development of more sophisticated methods that are able to detect and measure local structural or functional changes, or group differences. Moving outside of the brain, cine imaging and dynamic imaging required the development of non-rigid image registration to directly measure or compensate for local tissue motion. By non-rigid transformations one refers to those models which perform -at some extent- changes in the structure of the images. These changes vary from simple operations -which can still be modeled using linear (affine) transformations, such as scale, flip or shear- to more complex models that produce local deformations (deformable, initially called curved models).

Linear transformations are the first step towards non-rigid registration. Some registration algorithms increase the number of degrees of freedom by allowing for anisotropic scaling (giving nine degrees of freedom) and skews (giving 12 degrees of freedom). A transformation that includes scaling and skews as well as the rigid body parameters is referred to as affine, and has the important characteristics that it can be described in matrix form and that all parallel lines are preserved (affine deformations map parallel lines to parallel lines). A rigid body transformation can usefully be considered as a special case of affine, in which the scaling values are all unity and the skews all zero. Affine and rigid-body transformations can be conveniently represented using homogeneous matrices, these are 4-by-4 matrices for 3-D to 3-D mappings. The use of an affine transformation rather than a rigid body transformation does not greatly increase the applicability of image registration, as there are not many organs that only stretch or shear. Tis-

sues usually deform in more complicated ways. There are, however, several scanner introduced errors that can result in scaling or skew terms, and affine transformations are sometimes used to overcome these problems, an approach followed by many studies prior to the application of a deformable registration scheme [121, 210, 19, 176, 12, 235, 232, 82, 126, 211, 127]. In fact Crum et al. [43] point out that some approaches like in [86], that opt for a non-rigid registration, wrongly assume that good affine registration already exists for the population.

However, for most organs in the body many more degrees of freedom are necessary to describe the tissue deformation with adequate accuracy. Even in the brain, development of children, lesion growth or resection can make an affine transformations inadequate and deformable registration becomes necessary. The term deformable (as opposed to linear or global) is used to denote the fact that the observed signals are associated through a non-linear dense transformation, or a spatially varying deformation model. The problem consists of recovering a local transformation that aligns two or more signals that have in general an unknown relationship both in the spatial and in the intensity domain. In certain situations the deformation model is known, e.g., the geometrical distortion of the imaging system, but in most cases it is unknown. Therefore the number of parameters to be estimated can vary a lot and reach up to millions, when non-parametric dense transformations are considered. Increasing the dimensionality of the state space results in enriching the descriptive power of the model. This model enrichment may be accompanied by an increase in the model's complexity which, in turns, results in a more challenging and computationally demanding inference. A review on non-rigid registration can be found in [135, 78, 188].

1.2.2 Objective Function

In the simple case of *pairwise image registration*, which involves only two images, one image is usually referred to as source or moving image, while the other is referred to as target or fixed image. The goal then is the estimation of the optimal spatial transformation that maps homologous locations from the target physiology to the source physiology, by minimizing an energy cost function. Let the source image be denoted by $I : \Omega_I \subset \mathbb{R}^d \mapsto \mathbb{R}$, while the target image by $J : \Omega_J \subset \mathbb{R}^d \mapsto \mathbb{R}$, with $d = 2, 3$. The source image undergoes a transformation $\mathcal{T} : \Omega_I \mapsto \mathbb{R}^d$. The transformation at every position $x \in \Omega$ (Ω depicting the image domain) is usually defined using a dense deformation field $D : \mathbb{R}^d \mapsto \mathbb{R}^d$ (relative with respect to the current position), mapping every position $x \in \Omega$ from image I to its corresponding position $\mathcal{T}(x)$ in image J :

$$\mathcal{T}(x) = x + D(x) \tag{1.1}$$

Then the optimal transformation is achieved by means of an energy minimization problem:

$$\operatorname{argmin}_{\theta} \mathcal{M}(I, J \circ \mathcal{T}(\theta)) + \mathcal{R}(\mathcal{T}(\theta)). \quad (1.2)$$

We see that the cost function is the combination of two terms; \mathcal{M} is the data dissimilarity function that quantifies the level of alignment between the two images under the influence of transformation \mathcal{T} parameterized by θ , whereas \mathcal{R} regularizes the transformation, by assigning high cost to undesirable transformations, e.g. high local stretching or bending, or folding of transformation.

Regularization accounts for the ill-posedness of the problem of registration. In the case of rigid-body registration the regularization term is omitted, but in case of non-rigid and especially non-affine (non-linear) registration this term is very important. Regularizing the transformation is important not only to tackle the difficulty associated with the ill-posedness of the problem, but also due to the aim to favor specific properties in the solution that the user requires. Especially for biomedical applications, imposition of specific constraints that may be applied to the transformation, such that it exhibits special properties, are of great importance. Such properties include, but are not limited to inverse consistency, symmetry, topology preservation and diffeomorphicity. A wealth of methods have enforced diffeomorphic mappings, inspired mostly by the classical Demons approach of Vercauteren et al. [213], who had first proposed a variant of Thirion's algorithm [205] endowed with the diffeomorphic property. In brief, a dense deformation field is optimized using local image forces, alternated with Gaussian smoothing of the deformation field for regularization. Another classical popular pair-wise registration method assuring symmetry is the consistent image registration by Christensen and Johnson [36], in which a linear-elastic constraint is considered on both the forward and the inverse transformation. Finally, the symmetric log-diffeomorphic demons [212] combines diffeomorphism and symmetry principles.

1.2.3 Optimization Strategy

The aim of optimization is to infer the optimal transformation(s) that best (co-)align(s) the images of the population/sequence according to an objective function comprising a matching term and a regularization term (see above subsection 1.2.2). As a consequence, the choice of the optimization methods impacts the quality of the obtained result.

Optimization methods may be separated into two main categories based on the nature of the variables that they try to infer: i) continuous, and ii) discrete. The first class of methods solves optimization problems where the variables assume real values. On the contrary, methods in the second class

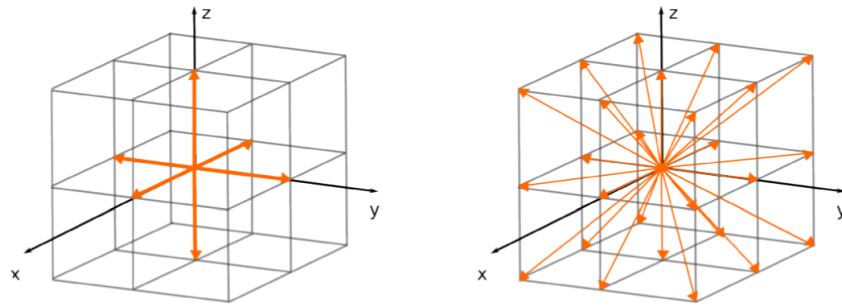


Figure 1.2: Discrete labelling in deformable image registration [53].

Different type of sampling strategies for the discrete label space used for image registration: sparse (left image) and dense (right image). Note that every label in this formulation corresponds to a displacement vector (in orange).

solve problem the variables take values from a discrete set. Both classes share the constraint of being dependent on the nature of the objective function and the structure to be optimized. Heuristic and metaheuristic don't have this constraint, though they do not enjoy theoretical guarantees regarding the optimality of the solution.

Continuous

In the vast majority of the medical image registration methods, the deformation variables are assumed to be real values and the objective function is designed in a continuous formulation, while continuous optimization methods are employed. In this case, the objective function should be differentiable, which consists of a basic constraint on using continuous optimization methods. The latter ones estimate the optimal parameters following an update rule of the following form:

$$\theta_{t+1} = \theta_t + \alpha_t g_t(\theta_t) \quad (1.3)$$

where θ is the vector of parameters of the transformation, t indexes the number of iteration, α_t denotes the step size or gain factor, and g defines the search direction. The way the previous parameters is chosen to be computed distinguishes the different optimization methods existing of this class. There exist various optimization methods, the most popular class being the gradient descent methods. We refer the interested reader to the survey of Sotiras et al. [188] for an overview of the various classes and sub-classes of continuous optimization methods.

Discrete

Over the last years, discrete methods and graphical models, have been employed to address many vision tasks [150], including deformable registration [58], through the use of a particular class of graphical models, the Markov

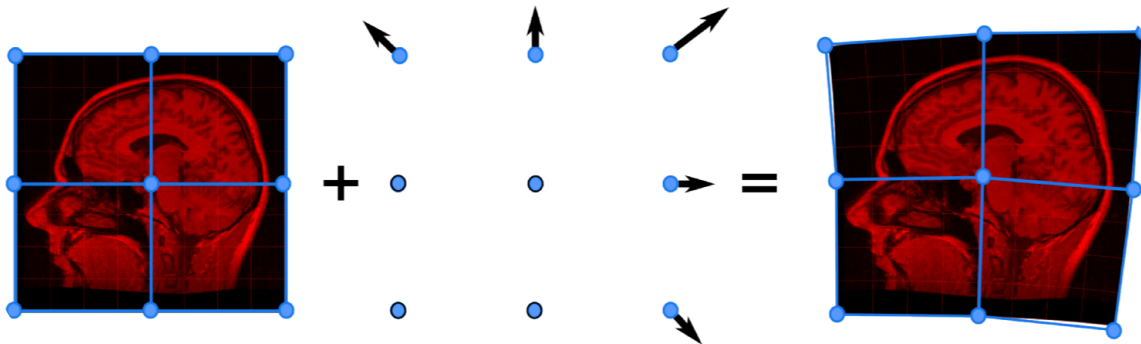


Figure 1.3: Deformation grid superimposed on an image [53].

Deformable registration is formulated as a discrete labeling problem on a grid-graph, superimposed to the source 2D image. The nodes of the graph correspond to the variables of a Markov Random Field, and model the control points of a FFD. The space of plausible deformations is explored by choosing different labelings.

Random Fields (MRF) [219]. Such an approach is a simple yet robust and efficient way to model the problem. MRF is a powerful modeling tool, that corresponds to an undirected graph G encoding a probability distribution governed by the local independence assumption (also known as local Markov or markovian property). Each node of this graph represents a variable from the probability distribution. Dependence among the variables is modeled using the graph neighboring system, meaning that two variables are dependent of each other if and only if there is an edge between them. This dependency can be extended from order two to any order, through the concept of clique. A clique is defined as a set of fully connected nodes; therefore, all the variables represented by nodes in a given clique depend on each other. The Markov property imposes that a node is independent of any other node given all its neighbors. This holds for any distribution that can be represented by a MRF.

Formally, a MRF is an undirected graph $G = \langle V, E \rangle$, where V is a set of nodes (every node $i \in V$ is associated to a variable $x_i \in X$ representing a control point) and E is a regular grid (2D or 3D depending on the dimensionality of the images). The neighboring system can be either a 4-connected (sparse) or a 8-connected (dense) one in case of 2D registration, and a 6-connected or a 26-connected one in case of 3D registration (where edges connecting nodes along the z axis are added to the standard system for the 2D case). The edges $(i, j) \in E$ are used to impose smoothness on the deformation field and render the problem well posed.

The label space L consists of labels $l_i \in L$ associated to d -dimensional displacement vector $d_{l_i} \in \mathcal{R}^d$ (i.e. the integer label l_i could be seen as an index value for the displacement vector d_{l_i}). Several strategies can be used to discretize the space. Two common approaches are the so-called dense and sparse sampling (illustrated in figure 1.2). When we assign a label l_i to a node i , the control point p_i is moved according to the displacement vector d_{l_i} .

A labeling Γ assigns one label l_i to every node $i \in V$. Recall that every discrete label l_i is associated to a d -dimensional displacement vectors d_{l_i} . Thus, D^Γ is defined as the set formed by the displacement vectors associated to the labeling Γ . Hence, by considering different labelings Γ , one can explore a discretized version of the naturally continuous space of deformation fields (see example in Figure 1.3). For example, let us consider a simple 2D label space formed by 5 labels $L = \{0, 1, 2, 3, 4\}$. We assign to every label a vector of length 1 in each direction (according to the sparse sampling shown in figure 1.2 together with the null vector). Therefore, the vectors associated to every label would be: $d_0 = (0, 0)$, $d_1 = (1, 0)$, $d_2 = (0, 1)$, $d_3 = (-1, 0)$, $d_4 = (0, -1)$. If we are dealing with a graph of 6 nodes, then the labeling $\Gamma = \{1, 3, 3, 2, 1, 2\}$ is interpreted as the following control point based representation of the displacement field $D^\Gamma = \{d_1, d_3, d_3, d_2, d_1, d_2\}$.

The search across this space is guided by the minimization of the MRF energy defined as:

$$E(\Gamma; G, F) = \sum_{p \in V} g_p(l_i) + \sum_{(i,j) \in E} f_{i,j}(l_i, l_j) \quad (1.4)$$

where Γ is a labeling assigning one label l_i to every node $i \in V$, G are the unary potentials playing the role of data (or matching) terms and F are the pair-wise terms acting as regularizers of the estimated deformation field. The MAP inference problem (a discretized version of the continuous formulation from equation 1.2, where $G = g_i(\cdot)_{i \in V}$ is associated to data terms M and $F = f_{ij}(\cdot, \cdot)_{(i,j) \in E}$ to regularization terms R) is therefore defined as:

$$\hat{\Gamma} = \underset{\Gamma}{\operatorname{argmin}} E(\Gamma; G, F) = \underset{\Gamma}{\operatorname{argmin}} \sum_{i \in V} g_i(l_i) + \sum_{(i,j) \in E} f_{i,j}(l_i, l_j) \quad (1.5)$$

The data term measures the matching quality (according to the similarity measure) between the deformed source image I and the target image J , given the displacement vectors. Any matching criterion, i.e. iconic, geometric, hybrid, feature vector-based, can be considered. The data term is the driving force of the optimization process. However, even if the matching criterion is optimally minimized, the resulting deformation field could be erroneous from geometrically view point. The regularization term plays a key role in this process, since it imposes geometrical and smoothness constraints towards anatomically realistic solutions. It is defined as a pairwise term acting on the two labels (displacement vectors) assigned to neighbor nodes. Using pairwise terms, one can encode different smoothness constraints, such as the standard Pott's model (penalizes deviations in the displacement assignment), truncated absolute or quadratic difference (penalize the magnitude of the vectors difference up to a bound), approximated curvature penalty (approximates a second order derivative of the displacement field) or the

distance preserving approach (penalizes changes in the distances between neighboring control points with respect to their initial position) [56]. Let us illustrate, for example, the distance preserving approach, defined as the ratio between the current position of the control points p_i, p_j and their original position $p_{o,i}, p_{o,j}$.

$$f_{i,j}(l_i, l_j) = \frac{\|(p_i + d_{l_i}) - (p_j + d_{l_j})\|}{\|(p_{o,i}) - (p_{o,j})\|}. \quad (1.6)$$

As mentioned, alternative definitions could be considered for this term, depending on different constraints and domain specific restrictions.

The final dense deformation field \hat{u} is interpolated from the set of displacement vectors $u^{\hat{\Gamma}}$ associated to the parameters $\hat{\Gamma}$, i.e. an interpolation strategy acting on the displacement of these control points is used to reconstruct the final solution. Given a set of control point displacements $D = d_1, \dots, d_k$, the dense deformation field $D(x)$ used in equation 1.1 is reparameterized as:

$$D(x) = \sum_{p=1}^k \eta_p(x) d_p, \quad (1.7)$$

and the transformation T becomes:

$$T(x) = x + \sum_{p=1}^k \eta_p(x) d_p, \quad (1.8)$$

where η_p is the weighting function corresponding to control point p . It determines the influence of a control point p_j to the image point x - the closer the image point the higher the influence of the control point. The actual displacement of an image point is then computed via a weighted sum of control point displacements. A dense deformation of the image can thus be achieved by manipulating a few control points and in general by moving the grid's control points, one ends up deforming the images. The parametrization of the deformation field leads naturally to the definition of a set of discrete deformation elements. Instead of seeking a displacement vector for every single image point, only the displacement vectors for the control points need to be sought. A common choice to define these weighting factors is the use of B-splines, resulting in the well-known Free Form Deformation (FFD) model, popularized in the medical image registration community by Rueckert et al. [173]. They adopt a regular grid as parametric model. Every control point contributes locally to the interpolation function. Other interpolation models like Thin-Plate Splines (TPS), proposed by Bookstein [24], could be adopted. TPS minimize the bending energy assuming infinite boundary conditions. Through the use of TPS a smooth transformation is generated. The local support for deformations and inherent computational efficiency make FFDs a good choice to deal with deformable image registration in a discrete scenario.

A common strategy to improve the accuracy of the method and increase its capture range consists in using a pyramidal approach. It allows a progressive search space exploration, while keeping low complexity. The idea is to start with displacement vectors with important distance and progressively reduce their spread, centering them around the current solution. It is clear that increasing the number of labels to infinity will converge to a continuous formulation. Since this is intractable from computational perspective [57], the idea behind this approach is to iteratively compose several deformation fields, while refining the grid of nodes and the label space, so that big as well as small local deformations are captured. At every iteration a fixed label space and constant number of grid nodes are considered, MAP inference for equation 1.5 is performed, while the resulting deformation field is composed with the previous one.

As presented above, deformable image registration was formulated as MAP inference problems, which can be solved through discrete optimization. Discrete optimization of MRFs is, in general, an NP-hard problem [185]. However, in special cases, it can benefit from very efficient solutions. The trivial brute force algorithm (i.e. trying all possible combination of labels for each and every variable) has an exponential complexity that makes such an approach unsuitable. More efficient algorithms have been developed during the last two decades which boosted the use of graphical models in the field of computer vision. They can be classified in three main categories according to Kappes et al. [91]: (i) polyhedral and combinatorial methods, (ii) message passing methods and (iii) move-making algorithms.

The first ones solve a continuous linear programming (LP) relaxation of the discrete energy minimization problem. The central idea is to relax the integrality condition of the variables in order to simplify the problem. Once the integrality constraint is relaxed, standard linear programming methods can be applied to solve the optimization problem, and rounding strategies are used to recover the integral solution. Examples of such approaches are Linear Programming Relaxations over the Local Polytope, Quadratic Pseudo Boolean Optimization (QPBO) [168] and Dual Decomposition [97].

On the other hand, message passing methods, are optimization methods in which messages are calculated and propagated between nodes in a graph. This propagation can be seen as a re-parametrization of the original problem aiming to establish special properties in the re-weighted function that makes inference easier. Examples are the standard Loopy Belief Propagation (LBP) [143] and Three Re-weighted Belief Propagation (TRBP) [218].

Finally, Max-flow and move-making algorithms make use of the well know max-flow min-cut [26] algorithm from graph theory, which can optimally solve some instances of discrete energies. These methods are usually combined with greedy strategies that iteratively minimize over the label space by solving a sequence of max-flow min-cut sub-problems. Examples are α -

expansion, $\alpha\beta$ swap [27] and FastPD [99] algorithms. Simpler move-making algorithms not using max-flow, but still applying the strategy of starting with an initial labeling and iteratively moving to a better one until a convergence criterion is met, are the classical Iterated conditional modes (ICM) [17] and its generalization Lazy Flipper [7]. An overview of the work that has been done in the area of inference algorithms on graphical models, as well as, their use to address the fundamental problem of biomedical image analysis, can be found in [149].

1.3 Statement

The vast range of potential applications as well as the technological advances create a dynamically changing environment that poses important challenges. Correspondence estimation algorithms must be computational efficient, operate even on real-time constraints, and highly versatile. Moreover, especially in clinical settings, the solution they provide should exhibit certain desired properties to facilitate or even allow for reliable subsequent processing.

The main reason that fuels the need for efficiency is the fact that the volume of acquired data grows with a fast rate, with medical imaging becoming a standard clinical practice. A second challenge is revealed if we consider either the vast range of problems to be tackled or the new imaging devices introduced in the clinical practice resulting in images with different properties. In its essence, the problem is always the same, establishing correspondences between two or more images. Thus, one should expect that an appropriate solution to it should be versatile enough to be used for any of the previous applications or image modalities. This underlines the need for modularity with respect to the main components of the algorithms.

The broad purpose of this thesis is to develop novel methods to perform group-wise deformable image registration, in order to tackle the problem of recovering correspondences among volumetric over time medical images in an efficient and modular way. To respond to the needs advocated earlier, efficient approximation schemes have been devised to achieve a good balance between accuracy and efficiency. In an effort to render the proposed algorithms both more efficient and modular, discrete optimization techniques based on a Markov Random Field formulation of the problem have been chosen.

On top of developing group-wise deformable registration methods, we also demonstrate how motion correction contributes to the extraction of meaningful imaging biomarkers in DWI. DWI provides functional information (i.e. diffusivity of water molecules) and is able to highlight both oncological and non-oncological lesions throughout the entire body [106]. DWI could add complementary information to the current state-of-the-art imaging technique in lymphoma patient management. To this end, we are seeking to

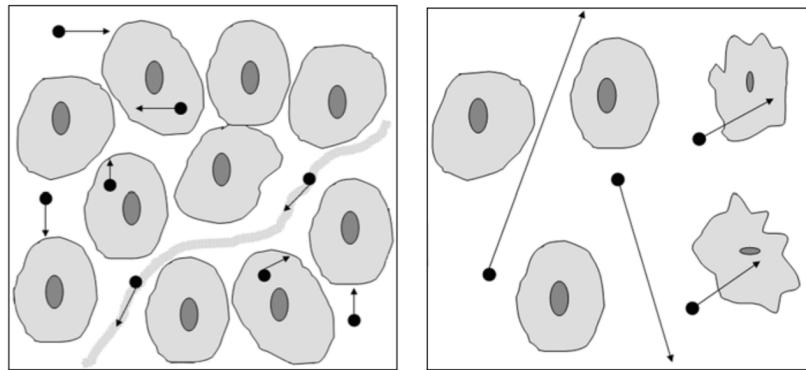


Figure 1.4: Diffusion of water molecules [95].

Left image: This is a drawing of restricted diffusion. Drawing represents 1 voxel of tissue evaluated by Diffusion-Weighted Imaging (DWI) containing cells and blood vessel. The black circles with arrows represent the water molecules within extracellular space, intracellular space, and intravascular space, all of which contribute to measured MR signal. There are two causes of the restriction. One cause is the observed high cellularity, which results into a reduced extracellular space. Moreover the cell membranes are intact, thus they act as barrier to water movement. *Right image:* This is a drawing of free diffusion. Here we observe low cellularity and defective cell membranes. In less cellular environment, relative increase in extracellular space allows freer water diffusion than more cellular environment would. Defective cell membranes also allow movement of water molecules between extracellular and intracellular spaces.

extract meaningful image-based quantitative parameters, depicted as parametric maps, which could be promoted to imaging biomarkers in case they could provide us with structural and physiological information to characterize lymphomas and/or assess therapy efficacy with prognostic quality with regard to the long-term clinical outcome [171]. Such parametric maps are susceptible to motion artifacts occurring during image acquisition, resulting in misregistration of the images obtained while changing the sensitivity of the MR scanner to diffusion [3, 108]. Thus, retention of the spatial information derived by a parametric map requires a step of motion correction prior to its computation [95]. We are focusing on the calculation of the Apparent Diffusion Coefficient (ADC) map, which quantifies the diffusion of water molecules within tissue, and specifically, we are interested in examining its potential to quantitatively characterize residual lymphoma masses.

1.4 Background on Diffusion-Weighted MRI

Imaging biomarkers are important tools for the detection, classification and staging of cancers, as well as for the assessment of the patient's response to the provided therapy and the detection of tumor reoccurrence [171]. In case of lymphoma patients, [^{18}F]fluorodeoxyglucose (FDG)-positron emission tomography (PET), has been established as the state-of-the-art biomarker for response assessment at the end of treatment [89, 35], as well as an early prognostic tool for predicting patient outcome in aggressive lymphomas [68]. However, its main caveat, the risk of a false-positive diagnosis due

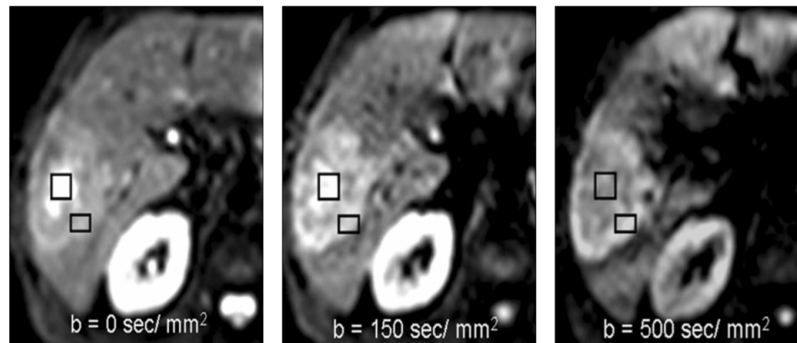


Figure 1.5: Tissue characterization by diffusion-weighted images [95].

Three diffusion-weighted MR images in 55-year-old man with liver metastasis obtained at different b-values. The patient large heterogeneous metastasis within right lobe of liver. Necrotic center of metastasis (squares) shows attenuation of signal intensity with increasing b-values, indicating less restricted diffusion. By comparison, rim of tumor (rectangles) is more cellular and shows little signal attenuation with increasing b-value.

to a non-specific inflammatory effect, sets in question its usefulness for various lymphoma subtypes. Moreover, PET imaging is associated with a non-negligible radiation dose, which is of particular concern for younger patients, because of the risk of radiation-induced secondary malignancies.

Meanwhile, over the last years, DWI has been the subject of research with promising results. DWI is a non-invasive functional imaging technique that explores the extra-, intra-, transcellular and intracapillary motion of water molecules in the body, as a result of their internal thermal energy [155]. In contrast to the case of a container outside the body, water movement in biological tissues is not entirely random (Brownian), as it is modified and limited by interactions with cell membranes and macromolecules, thus it depends on the microenvironment of the diffusing water molecules. The degree of this restriction is inversely correlated to the tissue cellularity and the integrity of cell membranes (see Figure 1.4). The sensitivity of the DWI sequence to water diffusion is varied by changing a parameter called b-value, which is proportional most of the times to the amplitude of the applied diffusion-sensitizing (bipolar) gradients around the 180° refocusing pulse (also known as the Stejskal–Tanner sequence [193]), but it can also change due to an alternation on the duration or the time intervals between the gradients.

DWI had initially been applied only to the evaluation of intracranial diseases [246, 51], but the advent of fast imaging sequences like echo planar imaging (EPI) and parallel imaging techniques allowed for faster acquisition of DW images with less motion artifacts, revealing great potential in cancer and bone marrow imaging of the body [110, 47], achieving some very promising preliminary clinical results [145]. On top of that, the introduction of whole-body diffusion-weighted imaging with background body signal suppression (DWIBS) using free breathing and Short-tau inversion recovery (STIR), yielded

high resolution 3D PET-like whole body images, that lead to immediate localization of metastases and primary tumors, like lymphomas [202], [214]. Because of their high cellularity and elevated nuclear-to-cytoplasm ratio, lymphomas have relatively high signal intensity on DWI compared to normal tissues. Thus, nodal and extra-nodal localizations of lymphoma show on DWI higher signal intensity than normal tissues but also than other pathological tissues like metastatic lymph nodes by carcinoma. The afore-mentioned functional information about lymphomas is different than the one provided by FDG-PET imaging, in which glucose metabolism is quantitatively reflected [106].

Whole-body diffusion DWI using DWIBS is mostly evaluated qualitatively by observing the relative attenuation of signal intensity on inverted-gray images with at least two b-values; one with $0s/mm^2$, that has a high signal-to-noise ratio (SNR) and gives a better estimation of the tissues' morphology and a second that depends on the type of lesion to be detected (for example $800-1000s/mm^2$ is considered the proper range for detecting cellular solid tumors showing relatively high signal intensity at that range) [95]. Tissues' appearance changes as we move to higher b-values, i.e. the image becomes darker, however this effect varies in different tissues, depending on their diffusivity (see an example in Figure 1.5). In addition to qualitative anatomical information, the ADC can be derived, which has been examined for lesion characterization. The ADC reflects the gradient of water diffusivity in the body. It is computed at each voxel and displayed as a parametric map (ADC map). The word "apparent" is added because other factors than random diffusion may influence the mobility of water (see Figure 1.6). The ADC is independent of magnetic field strength and can overcome the effects of T2 shine-through (hyperintensity on high b-values caused by high proton density and not increased cellularity), thus allowing more meaningful assessment of results.

1.5 Roadmap

The remainder of this thesis is organized into five chapters. In Chapter 2 a literature review on group-wise image registration for motion estimation/correction in spatiotemporal (4D) medical images is provided. Chapter 3 covers the introduction of our deformable group-wise registration method for motion correction. In that work, the deformable registration problem is formulated using Markov Random Fields (MRF) and the deformation fields were calculated such that an exponential model of diffusion could best explain the data. The problem is solved in an efficient one-shoot optimization. Next, in Chapter 4 the previous method is extended and endowed with the incorporation of the simultaneous, to the deformation fields, computation of the ADC map, based on spatial smoothness constraints. The assumption

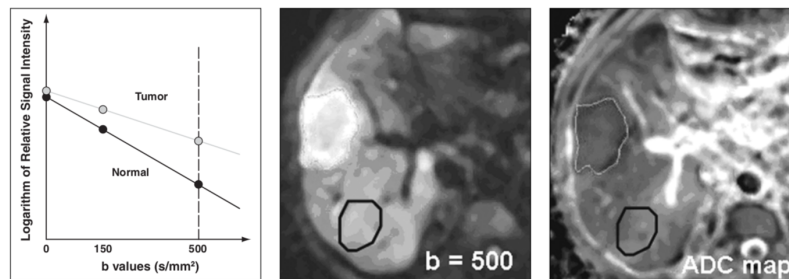


Figure 1.6: Apparent diffusion coefficient (ADC) [95].

Left image: This simplified schematic shows derivation of ADC. Logarithm of relative signal intensity is plotted on y-axis against values on x-axis. Slope of line fitted through plots is ADC. In this example, slope of line (ADC) is smaller for tumor (*gray line*) than for normal liver (*black line*). *Central and right image:* Here we show a tumor area with low ADC (*gray outline*, which is darker than normal liver with higher ADC values (*black outline*). One can notice that contrast on ADC map is opposite of that seen on diffusion-weighted image. On diffusion-weighted image, tumor showed less signal attenuation and appeared higher signal intensity than normal liver. Both those two images are obtained from the same patient as in Figure 1.5.

in that work is that the ADC values should not vary a lot within the same tissue. So in contrast to any previous work, the ADC map is not computed by voxel-wise curve fitting from the warped images, but by accounting for dependencies between neighboring voxels. Furthermore, temporal consistency (smooth transition over the deformation fields for increasing b-values) is imposed by an additional term in the MRF formulation. Then in Chapter 5 the effect of image registration on the potential of diffusion-based parameters to characterize lymphomas based on their types and level of malignancy (disease's stage), as well as assess or predict tumor's resistance to therapy (treatment response) is examined. The thesis is concluded in Chapter 6 with a discussion over the work presented in this manuscript, while suggesting different research directions for the future.

1.6 Publications

Published in International Conferences

1. *Deformable group-wise registration using a physiological model: application to Diffusion-Weighted MRI*; **E. N. Kornaropoulos**, E. I. Zacharaki, P. Zerbib, C. Lin, A. Rahmouni, N. Paragios; In IEEE International Conference on Image Processing (ICIP) 2016.
2. *Optimal estimation of diffusion in DW-MRI by high-order MRF-based joint deformable registration and diffusion modeling*; **E. N. Kornaropoulos**, E. I. Zacharaki, P. Zerbib, C. Lin, A. Rahmouni, N. Paragios; In Workshop of Biomedical Image Registration (WBIR) 2016.

Published in a Journal

1. *Histopathological image analysis for centroblasts classification through dimensionality reduction approaches*; **E. N. Kornaropoulos**, M. Khalid Khan Niazi, Gerard Lozanski, Metin N. Gurcan; In Cytometry Part A, 85(3), 242-255, 2014 - Wiley Online Library.

Under Submission to a Journal

1. *Deformable Registration in Diffusion-Weighted MRI Reveals Correlation with PET in Staging of Lymphomas*; **E. N. Kornaropoulos**, E. I. Zacharaki, P. Zerbib, C. Lin, A. Rahmouni, N. Paragios.

Chapter 2

Group-wise Medical Image Registration: A Literature Review

In the previous chapter, the problem of motion estimation in spatiotemporal (4D) medical images was introduced, while we argued on the necessity to be tackled with group-wise image registration. Given an image set $\mathbf{I} = \{I_i | i = 1, \dots, m\}$, the ultimate goal of group-wise image registration is to find a set of transformations $\mathbf{T} = \{T_i | i = 1, \dots, m\}$ that would establish correspondences between the anatomy at different time points. Such image sets are mainly used in studies of volumetric dynamic imaging (DTI, DCE-MRI, DWI etc.), or follow-up studies or longitudinal studies. The output of the image registration method should be a set of registered images $\tilde{\mathbf{I}} = \{\tilde{I}_i | i = 1, \dots, m\}$. Specifically, image I_i is wrapped to the common space, following the corresponding deformation T_i . After all images have been aligned in the common space, any quantitative analysis can be performed with a greater accuracy than if no registration had taken place. Ideally, a homology between more than two images is found simultaneously. Besides the afore-mentioned applications, group-wise image registration is also applied to register the anatomy of different subjects in case of inter-subject registration towards an atlas construction or in case of a group study analysis.

Similarly to pair-wise registration, the objective function in group-wise registration quantifies the level of alignment between the images, and it is typically used to guide the optimization process of the transformation model. Depending on the nature of information exploited in the matching process, the methods are most of the times classified as geometric (methods that use a sparse set of salient image locations to guide the registration, known as landmarks), iconic (those that use voxel/pixel intensities to quantify similarity), or hybrid methods (those that combine the afore-mentioned strategies in an effort to get the best of both worlds). An alternative to the previous approach was proposed by Shen and Davatzikos [182], in which attribute vectors, i.e. a set of geometric moment invariants (GMIs) defined on each

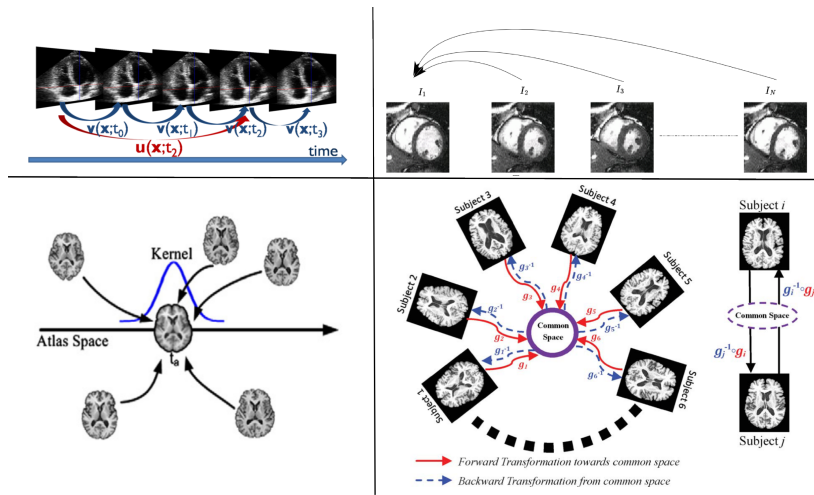


Figure 2.1: Examples of the different approaches in terms of the reference frame in 4D medical image registration.

Upper-left image: An example of the eulerian approach followed by De Craene et al. [46] to register a sequence of 3D-US images of the same patient. In that way, the large transformations between remote images in the sequence (denoted by a red arrow) are decomposed as a chain of small and smooth deformations. *Upper-right image:* An example of a G2R lagrangian approach, in which all the 3D MR cardiac images of the sequence are registered to a pre-selected one (the first image of the sequence in this example corresponding to the end-diastolic frame), which acts as the reference frame [121]. *Lower-left image:* An example of a second G2R lagrangian approach in which the reference frame to which all the MR brain images are co-registered is an atlas (generated template) [45]. *Lower-right image:* An example of an IRG group-wise registration with an unknown reference (consensus) space, proposed by Wu et al. [233]. All subjects in the group are connected by the forward transformations g_i (i.e., red solid arrows) to the common space (i.e., a purple circled region), and the backward transformations (i.e., blue dashed arrows) from the common space. The right panel shows how to transform between subjects S_i and S_j .

voxel in an image and calculated from tissue maps, were used to assess image similarity. We follow this classification to make a structural separation of the group-wise methods reviewed in this chapter.

In the same time the matching criterion indicates the reference frame (geometry) to which each image is transformed. The decision on the reference frame is very crucial in 4D medical image registration. The reference frame is the coordinate system assumed to be the common space to which all the images of the set should be co-registered. There is a variety of approaches on this issue. We distinguish two basic approaches, the eulerian approach, in which all deformations are described with respect to the neighboring time point, and the lagrangian approach, in which deformations are described with respect to a chosen reference frame/image, also called template or target image. The latter approach can be further discriminated into methods that select a specific reference image from the image sequence, those that generate a template or atlas of anatomy through the use of population statistics, to which all the images in the set are registered, and those that regard the desired consensus space as unknown and instead they seek for it with the aid of an objective, global (concerning all the images of the sequence) function, based on which the optimal deformation for each image

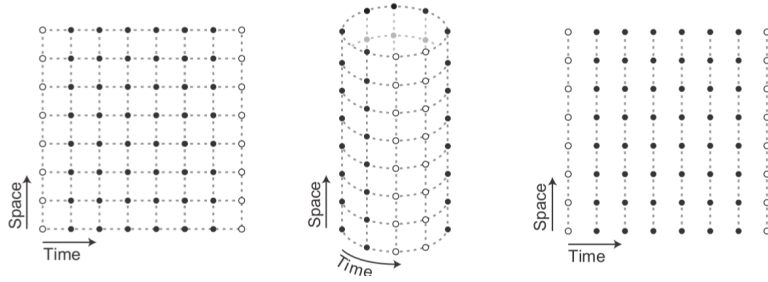


Figure 2.2: Illustration of the different approaches of spatiotemporal smoothness [138].

Left image: B-spline grid with spatiotemporal smoothness. *Central image:* cyclic B-spline grid with spatiotemporal smoothness. *Right image:* B-spline grid with only spatial smoothness. All three schemes can be used in reference time point, consecutive time point (eulerian) and groupwise registration approaches. In the cyclic version, the grid points at the temporal border (open nodes) are direct neighbors.

is estimated. The Implicit Reference Group-wise registration will be for the rest of the thesis denoted as IRG, while any of the first two sub-classes of the lagrangian approach will be denoted as G2R, from Group-to-Reference.

The most common approach is the G2R, in which each time one image is deformed to the reference frame based on an objective function like the one of equation 1.2. The final solution is given by iterating over the number of images. Thus, G2R registration consists of an approximation of a group-wise scenario, being driven by pair-wise registration to attain a group-wise registration. The downside of the G2R approach is that the result of the registration depends on the choice of reference image. IRG registration on the other hand is the correct implementation of a group-wise registration method, being template-free and thus unbiased. Therefore most of the times, an IRG registration, in which all images are co-aligned simultaneously, is preferable.

An IRG registration needs a global (concerning more than two) objective function, through which the optimal parameters of all the transformations could be inferred simultaneously. There have been proposed various global objective functions for an IRG registration, but one could distinguish two general formulations characterizing this approach. In one case, the objective function consists of a metric \mathcal{M} that has as an input all the parameters, together with a regularization term \mathcal{R} for each transformation:

$$\operatorname{argmin}_{\theta_1, \dots, \theta_m} \mathcal{M}(s_1 \circ \mathcal{T}_1(\theta_1), \dots, s_m \circ \mathcal{T}_m(\theta_m)) + \sum_{i=1}^m \mathcal{R}(\mathcal{T}_i(\theta_i)). \quad (2.1)$$

Then a second approach would be to use instead a pair-wise similarity metric under a summation over all images:

$$\operatorname{argmin}_{\theta_1, \dots, \theta_m} \sum_{i=1}^m \sum_{j, j < i} \mathcal{M}(s_i \circ \mathcal{T}_i(\theta_i), s_j \circ \mathcal{T}_j(\theta_j)) + \sum_{i=1}^m \mathcal{R}(\mathcal{T}_i(\theta_i)). \quad (2.2)$$

In Figure 2.1 we illustrate the differences between the afore-mentioned approaches through images found in articles following the corresponding approach. Finally, existing methods using a Lagrangian transformation model either take or don't take into account the temporal smoothness of the deformations, a constraint termed spatiotemporal smoothness (see also Figure 2.2 for an illustration). There is a vast amount of applications of group-wise registration techniques, following either the eulerian approach or one of the lagrangian approaches, to perform various tasks in the field of Medical Image Analysis. The vast majority of the proposed methods has been applied on brain images to perform tasks such as the group analysis of brain images of different anatomies towards either atlas-construction [87, 19, 250, 153, 38, 176, 224, 50, 235, 85, 225, 232, 117] or assessing diseases on the brain based on mono-modal registration [131, 210, 183, 196, 12, 132, 14, 69, 221, 40, 233, 86, 234, 43, 245, 178], as well as on multi-modal registration [146, 191, 217]. Table 2.1 shows the basic characteristics of these inter-subject group-wise registration methods. Moreover, automatic brain segmentation based on brain atlases has been also examined by various studies [10, 236, 82, 4], summarized over Table 2.2. Besides the brain, other organs have been studied through group-wise registration, such as the skeletal muscle calf [189], the heart in terms of cardiac motion [164, 227, 46, 198, 170] and automatic heart segmentation based on atlases of the heart [121, 127], the lung again in terms of motion [92, 23, 165, 31], and automatic segmentation [239] and the liver [243]. Moreover, motion correction has been applied on quantitative MR images towards an accurate computation of a parametric map of perfusion [21, 247, 230, 115, 71, 229, 125, 126, 41], or water diffusion [81, 211, 67], or of the diffusion of a contrast agent in colorectal cancer [20] and in breast cancer [237], and finally in Dynamic Contrast-Enhanced MRI (DCE-MRI) [29, 138, 72]. Table 2.3 shows the basic characteristics of group-wise registration methods applied on deformable organs outside of the skull. Finally, in Table 2.4, the main approaches towards IRG-based group-wise registration (discussed in the rest of this chapter) are presented.

The aim of this chapter is to provide an overview of advances in group-wise medical image registration, with a main emphasis on methods dealing with motion estimation in 4D medical images, as the overall scope is to derive useful conclusions that would aid us in optimally designing our approach towards motion correction in DWI. Even if studies on inter-subject group-wise registration towards atlas construction or group study analysis are not of our primary interest, some *classic* papers on the field, that have greatly influenced the advance of the ideas in group-wise image registration, are still mentioned. In the same time, even if our primary interest is group-wise registration, for the completeness of the presentation, references to pair-wise methods are also included as many of the motion estimation methods are

Table 2.1: Group-wise registration (*inter – subject*) methods for brain atlas construction or assessing diseases on the brain

Method	Transformation Model			Objective Function			Reference Frame			Optimization		
	Rigid	Affine	Deform.	Geom.	Icon.	Feat. (GMI)	G2R (population)	G2R (average)	IRG	Cont.	Discr.	Heurist.
Marsland et al. [131]		✓		✓			✓			✓		
Joshi et al. [87]			✓		✓				✓	✓		
Bhatia et al. [19]			✓		✓				✓	✓		
Cootes et al. [38]		✓		✓					✓	✓		
Seghers et al. [176]			✓		✓		✓			✓		
Twining et al. [210]		✓		✓						✓		
Shen and Davatzikos [183]	✓	✓				✓	✓					✓
Studholme and Cardenas [196]	✓				✓				✓	✓		
Park et al. [153]		✓			✓		✓			✓		
Zöllei et al. [250]		✓			✓				✓	✓		
Balci et al. [12]			✓		✓				✓	✓		
Wang et al. [224]			✓	✓					✓	✓		
Marsland et al. [132]		✓		✓			✓			✓		
Durrleman et al. [50]	✓				✓			✓		✓		
Baloch and Davatzikos [14]			✓			✓(OMS)	✓			✓		✓
Hamm et al. [69]			✓		✓		✓			✓		
Wang et al. [221]			✓	✓					✓	✓		
Wu et al. [235]		✓	✓			✓			✓	✓		✓
Orchard and Mann [146]		✓	✓		✓				✓	✓		
Jia et al. [85]			✓		✓		✓			✓		
Wang et al. [225]			✓			✓			✓			✓
Cootes et al. [40]		✓		✓				✓				✓
Wu et al. [232]			✓		✓			✓		✓		
Liao et al. [117]		✓	✓		✓				✓	✓		
Wu et al. [233]			✓		✓	✓			✓	✓		✓
Jia et al. [86]			✓		✓		✓			✓		
Wu et al. [234]			✓		✓	✓			✓			✓
Spiclin et al. [191]			✓		✓				✓	✓		
Wachinger and Navab [217]	✓				✓				✓	✓		
Crum et al. [43]			✓		✓		✓			✓		
Ying et al. [245]			✓		✓		✓			✓		
Shakeri et al. [178]			✓		✓		✓				✓	

Table 2.2: Automatic organ segmentation based on group-wise registration (*inter – subject* or *atlas – subject*)

Method	Images	Transformation Model	Objective Function	Reference Frame			Optimization	
				G2R (population)	G2R (average)	IRG	Cont.	Discr.
Baillard et al. [10]	3D MR (brain)	non-linear	iconic	✓			✓	
Lorenzo-Valdés et al. [121]	3D MR (cardiac)	"	"		✓		✓	
Wyatt and Noble [236]	3D MR (brain & cardiac)	"	"	✓			✓	
Iglesias et al. [82]	"	"	"				✓	
Alchatzidis et al. [4]	"	"	"				✓	
Shakeri et al. [177]	"	"	"				✓	✓

pairwise-driven; a template image is either selected or generated, which drives the group-wise registration through a series of pair-wise registrations between the template and each member of the image set. Moreover, the vast majority of the methods mentioned in this chapter are dealing with 3D images (the space domain Ω_i of image $I_i(x)$, with $x \in \Omega_i$ is \mathbf{R}^3), as for medical imaging the mapping is usually 3D to 3D (most of the medical data are acquired through tomographic techniques) and most of the examined methods are designed to work on such datasets. However, algorithms built for 2D image registration are still mentioned.

Table 2.3: Group-wise registration (intra – subject) methods for a quantitative analysis of deformable organs

Method	Images	Study	Transf. Model	Reference Frame			Optimization
				G2R (sequence)	G2R (generated)	IRG	
Bidaut and Vallée [21]	cardiac dynamic MRI	perfusion	rigid	FPC			continuous
Rao et al. [164]	"	cardiac motion	non-linear	end-diastolic			"
Wierzbicki et al. [227]	"	"	"	"			"
Kaus et al. [92]	4D lung CT	lung motion	"	end-inspiration			"
Xiaohua et al. [237]	DCE-MRI (breast cancer)	breast segmentation	"	earliest image			"
Buonaccorsi et al. [29]	DCE-MRI (WB cancer)	parametric map	rigid	"	synthetic ref.		"
Boldea et al. [23]	4D lung CT	lung motion	non-linear	eulerian	end-exhale ref.		"
Reinhardt et al. [165]	"	"	"	"	"		"
Castillo et al. [31]	"	"	"	"	"		continuous (nD+t)
De Craene et al. [46]	3D-US	cardiac motion	"	eulerian	"		"
Sundar et al. [198]	4D MRI	"	"	"	"		"
Sotiras et al. [189]	2D MR skeletal muscle calf	compute mean image	"	"	"	✓	heuristic
Zhang et al. [247]	MR brain perfusion	perfusion	rigid	"	"	✓	discrete
Wollny et al. [230]	myocardial perfusion MRI	perfusion	non-linear	"	synthetic ref.		continuous
Xue et al. [239]	4D lung CT	lung segmentation	"	random image	mean image		"
Roche [166]	fMRI	correct of slice timing	rigid	"	"		continuous (nD+t)
Metz et al. [138]	DCE-MRI (WB)	motion correction	non-linear	"	"	✓	"
Li et al. [115]	myocardial perfusion MRI	perfusion	"	"	pseudo groundtruth		continuous
Yigitsoy et al. [243]	4D CT/MRI (lung,liver)	compute mean image	"	"	"	✓	"
Hamrouni et al. [71]	cardiac dynamic MRI	perfusion	affine	FPC	"		continuous
Bhushan et al. [20]	DCE-MRI (colorectal cancer)	parametric map	non-linear	"	"	✓	"
Wollny et al. [229]	myocardial perfusion MRI	perfusion	"	"	synthetic ref.		"
Mahapatra [125]	cardiac dynamic MRI	"	non-rigid	"	"	✓	"
Mahapatra [126]	"	"	"	"	"	✓	continuous (nD+t)
Cordero-Grande et al. [41]	"	"	non-linear	"	"	✓	continuous
Huizinga et al. [81]	qMRI	parametric map	"	"	"	✓	"
Hamy et al. [72]	DCE-MRI (WB)	motion correction	"	"	mean image		"
Veeraraghavan et al. [211]	DWI	parametric map	non-rigid	b-value=250s/mm ²	"		"
Guyader et al. [67]	"	"	non-linear	smallest b-value	"		"
Royuela-del Val et al. [170]	cardiac cine MRI	cardiac motion	"	diastolic frame	"		"
Mahapatra et al. [127]	cardiac dynamic MRI	perfusion	non-rigid	"	"	✓	"

In all the studies the nature of information in the objective function was iconic, except for Sundar et al. [198] that used geometric moment invariant (GMI) features. Moreover, FCP stands for first-pass curve, qMRI for quantitative MRI, whereas with (nD+t) we denote the study in which spatiotemporal regularization took place.

2.1 Geometric

Geometric approaches aim to recover image structure by registering the images to a common geometric space through the minimization of a matching criterion that takes into account information on landmarks or meshes (point sets with connectivity information). Various ways have been proposed to detect points of interest, mostly in 2D images and less in the case of 3D images. The images should contain sufficient details to facilitate point detection, while the landmarks are assumed to be placed in salient image locations which are considered to correspond to meaningful anatomical locations. The underlying assumption is that saliency in the image level is equivalent to anatomical regions of interest. We refer the interested reader to a book by Goshtasby [63], where point-detectors and descriptors are extensively studied. Once the landmarks or the meshes have been defined, the next step would be the design of a strategy to achieve spatial correspondence among the shapes found in the images.

Geometric methods can be classified into those that establish solely the correspondences, those that infer only the spatial transformations and methods that infer both. In the the first class, the spatial correspondences among the images are known a priori and the method needs to assign every landmark from one image to another one in another image. Such a matching could be either performed by descriptor distance [139] or by formulating the

problem as graph matching [113, 220, 178]. These methods are useful when they are used in combination with an interpolation-based transformation model to estimate dense displacements between the two images. Hybrid registration (see later in this section) is another case where such methods are of interest, as one uses the sparse geometric correspondences along with an iconic criterion to improve the estimation of the spatial transformation. Regarding group-wise registration, a method of this class could be designed or used following a G2R scenario.

The second class of methods concern those that infer the spatial transformation that, when applied, will co-align the sets of landmarks. In case correspondences are known, the popular Procrustes analysis for shape analysis might for example be applied [60, 39]. A drawback of Procrustes analysis is the fact that it gives a solution that consists only of translating, rotating and scaling. On the other hand, if the correspondences are not known, the problem becomes more challenging, and the developed methods should be robust to missing correspondences and outliers. In the same time, this is the most common scenario in the various studies, therefore a significant effort has been given to develop efficient solutions on this issue. Shapes can be described by multiple unlabeled point-sets of unequal cardinality and their distributions can be modelled by Gaussian mixture models (GMMs), by assuming that features are independent and identically distributed [169]. In such a case, without knowing explicitly the point correspondences, non-rigid registration can be achieved through the use of divergence measures between probability distributions formed around point sets. Specifically, the Jensen-Shannon (JS) divergence and the CDF-based Jensen-Shannon divergence between the feature point-sets have been used as cost functions to be minimized in order to obtain the non-rigid deformation. Wang et al. [224] followed such a strategy to tackle the problem of the simultaneous IRG registration of multiple point sets. Given m probability distributions $P_i(\theta_i)$, where the parameter of the transformation θ in this case being a set of points $\{\theta_i \in R^d, i \in \{1, \dots, m\}\}$, d being the dimensionality of the image, the JS divergence of $P_i(\theta_i)$ is defined by:

$$\mathcal{M}(P_1(\theta_1), \dots, P_m(\theta_m)) = H(\sum \pi_i P_i(\theta_i)) - \sum \pi_i H(P_i(\theta_i)), \quad (2.3)$$

where $\pi = \{\pi_1, \dots, \pi_m | \pi_i > 0, \sum \pi_i = 1\}$ are the weights of the probability distributions $P_i(\theta_i)$ and $H(P_i(\theta_i))$ is the Shannon entropy. The drawback of this approach was that the problem could not be solved in closed-form. Instead, a computationally and memory demanding estimation based on the law of large numbers was required. In subsequent works, Wang et al. alleviated this shortcoming by trying both the generalized L_2 -divergence [222], as well as a new divergence measure called the Jensen-Renyi [221], which is a generalization of the Jensen-Shannon divergence being based on Renyi Entropy [73], both of which allow for a closed-form solution with an IRG approach.

The Jensen-Renyi global metric is defined as:

$$\mathcal{M}(P_1(\theta_1), \dots, P_m(\theta_m)) = H_\alpha(\sum \pi_i P_i(\theta_i)) - \sum \pi_i H_\alpha(P_i(\theta_i)), \quad (2.4)$$

where $H_\alpha(P_i(\theta_i))$ is the Renyi entropy. In the case of the generalized L_2 -divergence, the global metric becomes:

$$\mathcal{M}(P_1(\theta_1), \dots, P_m(\theta_m)) = \sum_{i=1}^m \pi_i L_2(P_i(\theta_i), P(\theta_1, \dots, \theta_m)), \quad (2.5)$$

where $P(\cdot)$ is the convex combination of the m probability densities, $P(\theta_1, \dots, \theta_m) = \sum \pi_i P_i(\theta_i)$. In both works, feature points corresponding to identifiable landmarks on heart wall boundaries were automatically extracted and tracked [200]. Any of the three afore-mentioned divergence metrics used as a global objective function for an IRG geometric registration is closer in formulation to equation 2.2. The thin-plate spline (TPS) was chosen to represent a regularized deformation towards a non-rigid group-wise registration. TPS has been also used to induce smooth deformations among cardiac 3D CT and MR images [227]. However, TPS are well-known to have some shortcomings, such as that the transformation from one image domain to another is not inverse consistent. Regarding the optimization scheme used to find the optimal transformation parameters in the approaches followed by Wang et al., the gradient of each divergence criterion with respect to the transformation parameters was estimated each time in order a gradient-based method (quasi-Newton) to be used.

Another way to perform non-rigid registration of shapes and points without caring to establish correspondences is by using signed distance functions to adopt a representation of the geometric information. In this case, the geometric primitives (e.g., landmarks or shapes) are assigned to zero distance, while the rest of the image elements are assigned a signed value based on their euclidean distance from the geometric primitives. Based on this representation, the optimal transformation can be estimated by performing standard intensity-based registration. Huang et al. [80] embedded shapes to the higher dimensional space defined by the signed distance transform and used Mutual Information as the matching criterion to align them, performing a G2R 2D registration. On the other hand, the correspondences and the transformation can be simultaneously estimated through the use of iterative schemes, where one component is estimated, and then the other component is refined based on this estimation. Maybe the most well-known method with this characteristic is the iterative closest point (ICP) method proposed by Besl and McKay [18], that estimates correspondences between pairs of points in the source and target shapes based on proximity. However, ICP optimization might get stuck in local minima due to wrongly assumed correspondences. Several methods trying to increase the robustness and ac-

curacy of the algorithm for free form deformation (see corresponding section in [188]). Any of these pair-wise methods could be incorporated in a G2R group-wise approach.

A very different geometric registration approach has been followed by researchers of the group of Imaging Science and Biomedical Engineering in the University of Manchester, mostly to cope with large population variation, i.e. they were designed mainly for inter-subject registration towards the creation of statistical deformable models, like anatomical atlases of organs. Such atlases can be used in medical image interpretation, where image registration can help in tasks as diverse as anatomical atlas matching and labeling, image classification, and data fusion. To this end, statistical deformable models of shape and appearance, the "Active Shape Model" and the "Active Appearance Model" were created, [209, 44, 40], with the objective function derived from the Minimum Description Length (MDL) coding approach [132]. The formulation of the global function in this case is based on the total description length. Actual description lengths are computed using the fundamental result of Shannon [181], which states that if there are a set of possible, discrete events $\{A\}$ with associated encoding-model probabilities $\{P(A)\}$, then the optimum code length required to transmit the occurrence of event A is given by:

$$\mathcal{M}_A = -\ln P_A \quad \text{nats}, \quad (2.6)$$

where *nats* is the analogous unit to the bit, but using a base of e rather than base 2. The total (global) description length (\mathcal{M}_{total}) is related to transmitting a discrepancy Δs between each image and the atlas, defined on the reference space, a discrepancy calculated according to the image histogram [209]. The authors used the clamped-plate spline (CPS), and an efficient spline based on the piece-wise linear interpolation of movements across a tessellated set of knotpoints in either 2D or 3D, in order to achieve non-rigid transformations. A simple gradient descent-based optimisation scheme for the nodes was used – points are moved singly to estimate the gradient direction for the objective function, but moved all at once using a line search.

Geometric approaches have been also followed in studies for motion correction in 4DMI, such as the study of morphological changes towards disease or pathology prediction through computing the distance between pairs of different motion trajectories (G2R approach) [200]. Furthermore, lung motion has been studied through the use of geometric group-wise registration, by recovering landmarks' trajectory [31] via compressible flow [79], as well as tracking the motion trajectories of junction structures and using the sum of normalized cross-correlation with subtracting means as the objective function, measured between each image in the sequence and a reference frame. [238]. A G2R lagrangian approach was also followed in both these works, where the maximum (end) exhale frame and the maximal

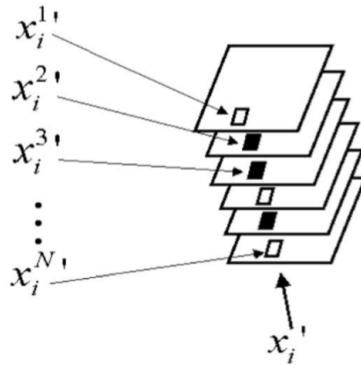


Figure 2.3: Illustration of the stack of images used as an input to the "empirical" entropy, which is the objective function in the congealing approach [112].

A pixel stack is a collection of pixels drawn from the same location in each of a set of N images. Here, the i th pixel from each of six images forms a pixel stack. Since half of the pixels are black and half are white, this corresponds to a Bernoulli random variable with parameter $p = 0.5$. The entropy of such a random variable is 1 bit.

inhale phase were chosen as reference frames respectively.

2.2 Iconic

Iconic methods, often referred to as either voxel-based or intensity-based methods, quantify the alignment of the images by evaluating an intensity-based criterion over the whole image domain. Devising an appropriate criterion is an important and difficult task. The criterion should be able to account for the different physical principles behind the acquisition of the images and thus for the intensity relation among them. Moreover, the properties of the similarity function (e.g., its convexity) may influence the difficulty of the inference and thus the quality of the obtained result. Especially for IRG registration, the definition of a global similarity cost is a very challenging task since on one hand, such a metric should be scalable and effective and on the other hand, global similarity metrics don't expand easily from pair-wise intensity-based metrics. The vast majority of group-wise medical image registration methods are using an intensity-based criterion, with the ones derived by information theory being the most popular ones, such as mutual information (MI) [226, 215, 37, 124] and its normalized version (NMI) [197]. A thorough survey on mutual-information-based registration of medical images can be found in [160].

One of the first IRG intensity-based registration methods was the congealing framework introduced by Miller et al. [140]. Congealing is a nonparametric technique for factoring, or separating, a set of images into sets of approximately independent "ingredients" or causes. It had been initially efficiently applied to binary digit recognition [112], a problem in

which there is shape variability within and between classes, and in general when variability occurs mostly in brightness or color or when any other form of structured but continuous variation of a parameter occurs. Congealing achieves its goal by reducing the variability in a set of images or other vectors, via minimizing the quantity

$$E = \sum_{i=1}^K \hat{H}(x_i), \quad (2.7)$$

the sum of the pixel(or voxel)-stack so-called "empirical" entropies, by transforming a set of images of a class (K being the total number of pixels/voxels in the image). For the simplest case of a set of binary (black and white) images, \hat{H} is defined as:

$$\hat{H}(x_i) = -\left(\frac{N_0}{N} \log_2 \frac{N_0}{N} + \frac{N_1}{N} \log_2 \frac{N_1}{N}\right), \quad (2.8)$$

where N_0 and N_1 are the number of occurrences of 0 (black) and 1 (white) in the binary-valued pixel stack (N denotes the total number of images in the set, see figure 2.3). In the end, the optimal set of transformations applied on the image set is the one that minimizes equation 2.7. The first to adapt the congealing framework to a population of grayscale-valued 3D brain images of different patients towards population atlas creation and without introducing any bias (IRG approach) were Zöllei et al. [250], who proposed an approximation of the total sum of voxel-wise entropies, with randomly selected locations in the data coordinate space being selected for evaluation. The transformation model was an affine one and an iterated stochastic gradient-based update mechanism (similar to that of [226]), that made the group-wise registration computationally efficient, was designed in a multi-resolution framework. Balci et al. [13] extended this method by including free-form deformations to the deformable registration of a group of brain images. An IRG registration was proposed by Wachinger and Navab [217], who performed simultaneous registration by accumulating pairwise estimates (APE) for the similarity estimation. The authors showed a strict mathematical deduction of APE from a maximum-likelihood framework and established a connection to the congealing framework. This is only possible after an extension of the congealing framework with neighborhood information. Moreover, efficient gradient-based optimization strategies for APE were developed. All these methods for simultaneous registration are not designed for motion estimation, and consequently, do not take temporal information into account. Bystrov et al. [30] tried to address both aspects, temporal smoothness and reference image selection, but the method is limited to local motion trajectories, whereas [243] proposed an IRG registration, with the same objective function as in [217], but which can cope with large deforma-

tions, while it imposes spatiotemporal smoothness on the deformations.

Another popular IRG registration framework was first introduced by Bhatia et al. [19], who proposed the NMI as the similarity criterion for comparing N images. Due to the fact that such a comparison would require an N -dimensional histogram, which for a large numbers of images would become computationally infeasible, one arbitrary image is chosen to act as an intensity, but not as an anatomical, reference. All pairs of intensities, comprising the voxel intensity in the reference and the corresponding intensity in each image, are added to the same joint histogram. Prior to Bhatia et al. method, Studholme et al. [195, 196] had proposed an IRG registration that simultaneously aligns the group of images to a common space using high-dimensional non-rigid registration. A metric of local measure of self-information (entropy-based) of the observed set of intensities at a given location is used to drive the local deformation. The cost function is optimized with the aim of maximizing the similarity between images, while penalizing displacement from the average shape. The drawback of that work was the fact that a weighting parameter to specify the influence of the penalty term needed to be chosen explicitly, which biases how well the constraint is satisfied. Bhatia et al. [19] alleviated that limitation by constraining the definition of the reference frame, without though giving primacy to any image. This was achieved by requiring that the sum of the displacement fields add to zero:

$$\sum_{n=1}^N \mathcal{F}_n(x) = 0. \quad (2.9)$$

The objective function is solved using Rosen's Gradient Projection Method [123], which is comparable to the method of steepest descent for unconstrained optimization. The afore-mentioned constraint inspired [138] to incorporate into their IRG registration method the following constraint on the deformation fields:

$$\frac{1}{N} \sum_{n=1}^N \mathcal{F}_n(x) = x, \quad (2.10)$$

which denotes that the average deformation should be restricted to be the identity transformation. The authors opted to cope with motion correction on dynamic medical imaging data. To this scope, the authors employed a lagrangian $nD+t$ B-spline transformation model in which both spatial and temporal smoothness are taken into account. The similarit metric used minimized the intensity variances over time, while a constrained optimization using stochastic gradient descent method with adaptive step size estimation was incorporated in their framework. The same constraint as in [138] on the transformations was also imposed by Cordero-Grande et al. [41] to simultaneously co-align a sequence of perfusion cardiac 3D MR images, while a new sparsity-promoting metric was proposed. A gradient descent procedure

was used here too to find the optimal solution to their objective function.

The last three afore-mentioned IRG approaches had focused on the small deformation setting, in which arithmetic averaging of displacement fields is well defined. Joshi et al. [87] developed a unbiased group-wise registration method to be used in the large deformation diffeomorphic setting. The authors induced a symmetric metric on the space of diffeomorphisms by using a Sobolev norm via a partial differential operator L on the velocity field v , as a similarity metric. Besides this metric, their objective function included a regularization term on the velocity to meet the criteria for diffeomorphism. The optimization was based on the Euler–Lagrange equations derived by [120]. A similar IRG method to the one of Joshi et al. was later presented by Geng et al. [55], who used a similar objective function with the difference lying on how the transformation is parameterized and how the transformations were regularized. Geng et al. used a Fourier series to parameterize the transformations, while a linear elastic model was used in the place of the regularization term, in order to achieve the derivation of small deformations. The authors argue that, though large deformation registration approach provides more degrees of freedom for registration than a small deformation model, it increases the complexity and computational requirements, which may not be necessary in order to answer a particular scientific question. In any case, the choice of using a small or large deformation model should depend on the application.

In general the problem of large deformation registration mainly concerns researchers working on inter-subject registrations, i.e. towards anatomical atlases creation. In such works, a similarity metric that has been proposed is the length of the geodesic path that connects "similar" images of the population, defined as a weighted sum of the intensity difference and the smoothness measure of the velocity field. The geodesics are commonly computed on the manifold of diffeomorphic transformations [9, 87], an approach that is though computationally expensive and which might induce geodesics that do not represent valid anatomies. Hamm et al. [69] on the other hand, compute the geodesics on the manifold of the observed anatomical variations from the data through a learning scheme, which turned to give a better visualization of the data structure and allowed the authors to choose an optimal template among the samples. Learning the manifold of the observed anatomy might be a useful approach towards motion correction in longitudinal or follow-up studies in 4DMI.

Another IRG registration method, applicable on multi-modal registration was proposed by Orchard and Mann [146]. More specifically, the authors opted to register simultaneously images acquired from different sources. Their method is based on clustering in the joint intensity scatter plot (JISP). The density distribution of the scatter points in JISP is estimated first and then images are deformed in such a way so that the dispersion of the scat-

ter plot is minimized. Density estimation of the clusters is modeled as a Gaussian mixture model (GMM), and is established iteratively using an estimation-maximization (EM) method. Moreover, a Newton-type optimization scheme was used. A drawback of that work was that only rigid and linear transformations were considered, which limits its application mainly to brain images. By incorporating a deformable model, such a metric could be potentially applied on spatiotemporal 4D images, when their intensity profile varies through time due to the physiological/chemical process evolving during image acquisition. Another IRG registration method applied on a group of images from different modalities was proposed by Spiclin et al. [191] too. In that work, correspondences across the images are modeled by the gradient-based joint density function (JDF) of the co-occurring image intensities, which explains the statistical dependence among the image intensities. More specifically, the so-called tree-code registration method is proposed for registering a group of multimodal images that estimates the JDF through an efficient hierarchical subdivision of the joint intensity space (JIS). Although registration based on the minimization of joint entropy had already been proposed, they follow a hierarchical intensity-space subdivision scheme to efficiently approximate the high-dimensional JDF and the joint entropy by the Parzen kernel method, as well as they use the Hilbert kernel that captures all important features of the JDF, avoiding thus the need to tune the kernel bandwidth parameters. Non-linear registration was attained using TPS.

Very recently, a task-specific IRG approach has been presented. In a study for quantitatively and automatically assessing the response to chemoradiotherapy for patients with colorectal cancer, Bhushan et al. [20] exploited that intensity changes in dynamic contrast-enhanced MRI (DCE-MRI) are expected to behave according to a low-dimensional pharmacokinetic (PK) model (Tofts pharmacokinetic model [207]). Therefore they designed their objective function based on this model, under the assumption that the set of the observed images is obtained when the original image, derived by the PK model, is deformed (due to patient-motion) and then subjected to some noise process, modeled with a Gaussian distribution. The similarity criterion in the end was an sum squared error over the image domain between the transformed with the inverse transformation observed image and the original image defined by the PK model. Without knowing though the model's physiological parameters of interest at each voxel, they designed a joint PK model fitting and estimation of the deformation field within a Bayesian setting, by maximizing the joint posterior probability P of the deformation \hat{u} applied to each dynamic time frame, and the PK parameters $\hat{\Theta}$ that best explain the observed data:

$$[\hat{\Theta}, \hat{u}] = \underset{\Theta, u}{\operatorname{argmax}} P(\Theta, u | X_0, Y, \sigma), \quad (2.11)$$

where X_0 denotes the image before contrast agent injection, Y denotes the image formation model, and σ is a noise parameter. Equation 2.11 was solved by computing the derivatives of the second part of the equation with respect to Θ and u , in a Gauss-Newton optimization framework. The afore-mentioned the diffeomorphic deformation framework based on the LogDemons approach [212] was followed to deform the images, where the transformation that needs to be applied to each image is parametrized by a stationary velocity field instead of a displacement field. That work was actually an advanced version of the original rigid registration approach with an embedded PK model [29] to a deformable registration, in order to accommodate localized intensity differences due to contrast agent uptake.

Furthermore, Zheng et al. [248], examining a G2R registration method to co-align DCE-MRI sequences, argued too against the use of a classic intensity-based similarity metric, like the sum squared distance (SSD), since due to the temporal intensity changes in DEC-MR data, the shrinking/expanding problem of tumor can inevitably happen [203]. Instead the authors propose any robust estimation function [70], while they chose the Lorentzian estimator for their method:

$$\rho(t) = \log(1 + (t/\sigma)^2/2), \quad (2.12)$$

where σ is a scale parameter to control the function's shape. SSD might be an appropriate metric for mono-modal registration, however in case of DCE-MRI, it assigns a high "weight" to the outlying measurements corresponding to the temporal intensity changes. Deformations are driven more by the unreliable intensity differences, leading to the shrinking/expanding problem in registration. In contrast, the Lorentzian function is more forgiving about the outlying measurements, reducing the driving force from the temporal intensity changes.

Another task-specific IRG registration method has been proposed for studies dealing with registration of brain perfusion images. More specifically, for a perfusion study, the voxel-wise intensity profile over time is modeled as a function of time $f(t)$ and spatial correspondence among images acquired on instances different can be found through measuring the smoothness of that function. Subsequently its smoothness can be measured by the total quadratic variation $\int_0^{t_n} (f'(t))^2 dt$, assuming $f(t)$ is continuously differentiable. That concept was proposed by Zhang et al. [247], who approximated the total quadratic variation as $E = \sum_{n=1}^N \sum_{k=1}^K [I_i(\mathcal{T}_n(x_k)) - I_{n'}(\mathcal{T}_{n'}(x_k))]^2$, where $n' = n - 1$ or $n' = N$ for $n = 1$. The Levenberg-Marquardt method was used for optimization. A limitation of that work was the fact that, since it was designed for brain perfusion images, only affine transformations were allowed. Later Mahapatra et al. extended that initial work to a non-rigid IRG registration framework on their studies on 4D cardiac perfusion images [128, 125, 127]. Besides the increase in the number of degrees of freedom for the transformation model, the authors proposed also a different objective function, in which

both the first and second derivatives are used for the entire image sequence.

On the other hand, an eulerian approach was followed by De Craene et al. [46] to register spatiotemporal 3D ultrasound (3D-US) images. The authors used a deformable model, referred to as Large Diffeomorphic Free Form Deformation (LDFFD), to recover longitudinal strain curves from healthy and Left-Bundle Branch Block (LBBB) subjects. In LDFFD, a set of Free-Form Deformations (FFD), each one capturing the motion between consecutive image frames, is jointly optimized to obtain the consistent temporal transformation that maximizes the joint alignment of all images in the sequence. This strategy ensures that the transformation at each time step is coherent with the transformation of previous temporal phases, and consequently increases the robustness of the alignment procedure. The authors argue that by decomposing the transformation as a chain of smooth deformations with a small magnitude, the invertibility of each transformation is ensured, provided that the temporal resolution of the input image sequence is satisfactory. In term of the similarity criterion, the image metric gradient was estimated between consecutive images. Such a metric requires the computation of the derivative of the displacement field at spatial samples of the fixed image domain with respect to all transformation parameters, here defined as parametric Jacobian. This computation of the parametric Jacobian is a key component of their algorithm since it introduces a coupling between the different time steps and enables the optimization of all transformation parameters simultaneously. This coupling raises from the fact that acting on the transformation parameters at a given time step modifies the transformation of the evaluated point at all subsequent instants. A version of the quasi-Newton BFGS optimizer [180] that uses less memory (L-BFGS) was used for optimizing their objective function.

All the afore-mentioned iconic registration methods use the raw images to calculate the similarities among the different instances of the image sequence. However, particularly for motion estimation in volumetric dynamic imaging, an alternative approach has been proposed and it is based on separating motion from contrast enhancement before registration. Melbourne et al. introduced an algorithm named progressive principal component registration (PPCR) that gradually removes misalignments [136, 137]. The method is based on the iterative use of principal component analysis (PCA) combined with a standard registration algorithm such as multi-resolution FFD [142]. In PCA, contrast changes are assumed to appear in the more significant principal components and motion in the less significant. This was used to create a synthetic motion-free set of target images using a limited number of principal components that correspond to contrast enhancement (G2R approach). Then a similar approach using robust principal component analysis (RPCA) this time was proposed by Hamy et al. [72] to cope with motion correction due to respiration in Dynamic Contrast Enhanced (DCE-)

MRI. Their hypothesis is that RPCA coupled with a registration algorithm based on residual complexity minimization [144] provides more accurate registration of DCE time series. A possible flaw of these two afore-mentioned ideas is the fact that there is no guarantee that the local changes caused by contrast enhancement can be correctly identified in the more significant principal components in the presence of motion. For example, a small translation at one of the time points might not be identified through the correlation or the covariance matrix (the approach should be more valid in case of small local deformations).

PCA was also used for data decomposition recently for the development of a non-rigid IRG registration method by Huizinga et al. [81]. The goal of their method was to compensate for motion in spatiotemporal 4D MRI, also referred to as quantitative MRI in their paper. A correlation matrix of the datapoints in the model is defined and subsequently, dimensionality reduction is applied on the dataset, based on this correlation matrix. Then a dissimilarity measure is proposed based on the idea that when motion is present in the images, the data no longer adheres to the presumed acquisition model and the eigenvalue spectrum of the correlation matrix changes. No regularization on the transformation was accounted for, while minimization of the similarity metric was achieved with gradient-based optimizers. Their method proved to be superior to a similar IRG registration approach based on MI only on one of the three datasets examined, maybe mainly due to the fact that the proposed dissimilarity metric is based on the selection of an optimal number of eigenvalues capturing the highest percentage of data variance, which is use-defined and thus highly subjective.

Close to the concept of applying dimensionality reduction on the raw data, Milles et al. [141] used Independent Component Analysis (ICA) to compensate rigid heart motion in perfusion scans. More recently, Wollny et al. [229] investigated the use of ICA to decompose data prior to registration in free breathing cardiac MRI. In this case too, the objective is to remove motion elements to form a synthetic target time-series. The method performed better than the one published by the same author earlier, that was based on exploiting the quasiperiodicity in motion correction of free-breathing myocardial perfusion MRI [230]. Still the performance of the method in [229] heavily depends on the ability of ICA algorithm to create synthetic reference images that are related to motion, in order to be used in the registration framework as templates, as well as the fact that it is a supervised method.

What all the afore-mentioned methods have in common is the fact that they used continuous, gradient-based optimization to reach the global minimum of their objective function. Sotiras et al. [189] approached the problem of group-wise registration with a discrete formulation, that enables different deformation models and matching criteria to be used in a straightforward manner. The deformation fields were modeled by cubic Hermite splines,

Table 2.4: Group-wise methods following an IRG approach

Objective	Characteristic	Studies
Congeealing (minimize sum of voxel-wise entropies)	iconic,continuous	Miller et al. [140], [250], [112], [243], [217]
Penalize displacement with a weight from the average shape	"	Studholme and Cardenas [196]
Penalize displacement from the average shape	"	Bhatia et al. [19],[12]
Average deformation be restricted to identity transformation	"	Metz et al. [138], [41]
Large diffeomorphic deformations	"	Joshi et al. [87]
Small deformations through a linear elastic model	"	Geng et al. [55]
Increase gradient-based JDF (multi-modal registration)	"	Spiclin et al. [191]
Dispersion of JISP be minimized (multi-modal registration)	"	Orchard and Mann [146]
Intensity profile smooth (1 st derivative) over time	"	Zhang et al. [247]
Intensity profile smooth (1 st and 2 nd derivative) over time	"	Mahapatra [125], [126], [127]
Decrease fitting to a model error	"	Bhushan et al. [20]
Decreases distance to presumed acquisition model (PCA)	"	Huizinga et al. [81]
Global statistical compactness with locally smooth deformations	iconic,discrete	Sotiras et al. [189]
Decrease Minimum Description Length (MDL)	geometric,continuous	Twining et al. [209]
Decrease JS divergence	"	Wang et al. [224], [221]
Matching forward and inverse transformations	GMI's,heuristic	Sundar et al. [198],[233],[234]

while they used Markov Random Fields (MRF) to model the dependencies among the the deformation fields and the observations (images), reflected on an MRF-based energy formulation, which consisted of their objective function and had an entropy estimator based on spacings [25] as its similarity criterion. Their objective function was solved by an an efficient linear programming method [101]. Moreover, by imposing hard constraints to the allowed deformations [172], the diffeomorphic property was addressed in their method. Alchatzidis et al. [4] proposed a multi-atlas segmentation using graph-based deformable registration. An adaptive co-registration and segmentation of brain tumors where the sampling resolution of the label space is adapted according to the image content is proposed in [152].

2.3 Hybrid

Hybrid methods opt to take advantage of the useful features of both iconic and geometric approaches, while deminishing the limitations that both have by not relying completely on any of these approaches. In recent years, hybrid landmark- and intensity-based registration (LBR and IBR respectively) has been proposed to register lung images [244]. A multiresolution framework was designed. On each level, LBR is first performed. The resulting transformation is then used as the starting point to guide IBR in which the transformation is refined based on matching the intensity patterns of the images (sum of squared local tissue volume difference). The authors followed a lagrangian G2R approach.

2.4 Methods based on Attribute Vectors

Another popular approach to image matching is through the use of attribute vectors (Geometric Moment Invariants) [182]. Considering that the accuracy

and robustness of correspondence detection depends on how effectively the image descriptor can capture the local and global properties of the given point, it is desirable that these descriptors are scale and rotation invariant. In some organs, such as the heart, that don't have many geometrically discernible points, most local descriptors, such as intensity and gradient information, fail to capture the uniqueness of a given voxel. A morphological signature is thus attributed to each point, the attribute vector, for the purpose of minimizing the ambiguity in image matching and correspondence detection during the deformable registration procedure. The motivation is that a rich enough attribute vector will be able to differentiate between voxels that would be considered the same based only on their intensity information. Thus, fewer local minima will be present and better accuracy may be achieved. To further reduce the effect of the local minima, they proposed a hierarchical scheme that approximates successively the objective function through the use of an increasing number of voxels where the matching is evaluated.

Sundar et al. [198] extended the initial work of Shen et al. to IRG registration for cardiac motion estimation. A vector of geometric attributes was attached to each point on a surface model of the anatomical structure. Each attribute vector reflected the geometric properties of the underlying structure from a local scale (e.g., curvature), to a global scale and matching reflected spatial relationships among distant surface points. Their objective function included two image attribute similarity terms, one defined on the forward transformation measuring the similarity of attribute vectors between each point in the sequence, and a similar second similarity term defined the inverse transformation to ensure correct matching between points in different sequences. Moreover, temporal consistency and spatial smoothness were enforced by two additional constraints on the objective function. A continuous optimization scheme that doesn't require the calculation of any derivative is employed to solve for the optimal parameters of the deformation model [65]. Another group-wise registration based on attribute vectors was also proposed by Wu et al. [235] towards brain atlas construction, but their approach is characterized as G2R as the a subject image closest to the mean of the initial affine registered images is selected as the reference one (exemplar).

2.5 Discussion

In this chapter, an overview of the group-wise image registration methods designed for and applied on medical images over the last twenty years was given. The previous analysis can act as a roadmap to guide our efforts towards proposing computational efficient and versatile group-wise registration algorithms for motion correction in quantitative MRI. Let us first discuss

how our goals influence our choices regarding the deformation model, the objective function and the optimization strategy. All three choices have an impact upon the qualities of the resulting registration algorithm.

Efficiency depends on the following aspects: the number of deformation parameters, the computational cost on the evaluation of the objective function and the convergence properties of the optimization strategy. Apparently the fewer considered parameters, the lesser the computational burden to infer them would be. The complexity of the objective function relates directly to the computational performance of the algorithm. Complex functions requiring computationally expensive calculations will slow down the response. A fast converging optimization strategy is required to restrict the number of cost evaluations.

Versatility is also conditioned upon the number of deformation parameters, the nature of the objective function and the variety of energy forms the optimizer can handle. The number of degrees of freedom is a bound for the expressive power of the deformation model and it has a direct impact upon the deformations that may be recovered and thus restricts the problems the registration algorithm can treat successfully. Different problems call for different objective functions to account for the relation between different intensity distributions. A universally applicable objective function does not exist. The optimization method is constrained by the nature of the objective function it can handle. The ideal optimizer should be able to deal with a variety of objective functions.

Having described the desirable characteristics our group-wise registration method should possess, we identify a number of issues we have to take into account while designing such a method.

Rigid versus non-rigid transformation models: As mentioned in chapter 1, for most organs besides the brain deformable image registration becomes necessary. However, rigid registration intra-subject can be applied prior to deformable registration to compensate for subject's movement inside the scanner during image acquisition. As far as the deformation model is concerned, we favor interpolation based models. By controlling directly the parameterization of the deformation model, we can choose the minimum number of degrees of freedom that is needed to recover the deformations of the problem at hand. Thus, we can achieve the best compromise between computational efficiency and versatility. In addition, the local spatial influence of the deformation parameters allows for the design of efficient approximative schemes for the cost calculations. Finally, hard constraints in grid-based models ensure the diffeomorphicity of the deformation, a key property that we desire our algorithm to exhibit.

Diffeomorphic property: Since our objective is to correct for patient motion during a single scan, it would be natural to assume that there should be no change in topology when we apply the deformations. In other words,

assume that each image in a set should contain the same structures, and hence there should be a unique and invertible one-to-one correspondence between all points on each pair of images; we would expect all deformations to be invertible and smooth. This suggests that the correct representation of warps is one that will not "tear" or fold the images. For these reasons, we have chosen to use the diffeomorphic deformation framework.

Regarding the reference frame: G2R approaches through the selection of a statistical atlas are more popular on brain studies where spatial correspondences can be interpreted, i.e. one could know whether a mapping denotes a specific organ or tissue or an abnormality. However, in 4DMI where the main purpose of registration is to correct for motion, an IRG approach should be preferable over a G2R, as it is unbiased though challenging in terms of computational cost. For example, Geng et al. [55] compared these two approaches and showed that the IRG technique, with the small deformation elastic model, provides better transformations compared to reference-based methods in terms of smaller within-group variance after registration.

Regarding the nature of information: Geometric registration is robust with respect to the initial conditions and the existence of large deformations. The solution of the registration problem is obtained in a relatively straightforward way once landmarks have been extracted. However, locating reliable landmarks is an open problem and an active topic of research. Most importantly, the sparse set of directly obtained correspondences gives rise to the need for extrapolation. Interpolation then results in a decrease in accuracy as the distance from the landmarks increases. The interest regarding geometric methods has decreased during the past decade. Those limitations hinder apparently the development of hybrid methods too. Nevertheless, geometric methods constitute a reliable approach for specific applications. On the other hand, iconic approach has the potential to better quantify and represent the accuracy of the estimated dense deformation field. Nonetheless, it comes at the cost of increased computational expense. Where geometric methods use a small subset of image voxels to evaluate the matching criterion, iconic methods may use them all. Moreover, due to the fact that salient points are not explicitly taken into account by the matching criterion, the important information they contain is not fully exploited to drive the registration. In addition, initial conditions greatly influence the quality of the obtained result due to the non-convexity of the problem. Nevertheless, iconic group-wise registration methods have become very popular as the computational power has been increased over the years. Moreover, sometimes it is definitely an advantage to use all the relevant signal intensity information intrinsically available in the images. The main benefits of direct intensity-based metrics are their easy implementation, the computational efficiency, and the satisfactory results in intra-subject, intra-modality registration. Finally, registration method based on attribute vectors use a heuristic optimization scheme, with

no guarantees on the convergence to a global optimum, restricting thus their use.

Continuous versus discrete methods: As far as the optimization strategy is concerned, we opt for discrete optimization methods. Discrete methods have several advantages when compared with continuous approaches for image registration. First, discrete algorithms are inherently gradient-free, while most part of continuous methods require the objective function to be differentiable. Gradient-free methods do not require computation of the energy derivative. Therefore, it may be applied to any complex energy function (allowing the user to define its own similarity measures in case of registration problems). In other words, they are modular with respect to the objective criterion enlarging the range of applications, the registration algorithm can cope with. The only requirement is that this function must be evaluated in a variety of possible discrete labelings. Second, continuous methods are quite often prone to be stuck in local minima when the functions are not convex. In case of discrete methods, even complicated functions could potentially be optimized using large neighbor search methods exhibiting good convergence rates. The main limitation of discrete approaches is the discretization of the continuous space. Discrete optimization methods are limited with respect to the structures they can optimize. Being able to cope only with discrete structures, they may lack precision. Nonetheless, smart sampling of the solution space may alleviate this precision issue while and in addition boost their efficiency. Last but not least, parallel architectures can be used to perform non-sequential tasks required by several discrete algorithms (such as message calculation in LBP) leading to more efficient implementations. By using a discrete label space we can explicitly control its range and resolution, while in continuous models it is not clear how this type of information can be used to constraint the solution.

Chapter 3

Deformable Group-wise Registration Using a Physiological Model: Application to Diffusion-Weighted MRI

In the end of the previous chapter we drew the generic lines regarding our choices with respect to the deformation model and the optimization scheme. However the question of an appropriate objective function, as well as the optimal strategy in terms of defining a reference frame is still open.

The previous study enables us to draw a few conclusions. First of all, regarding the objective function, in cases where the intensity profile of the tissue on the image changes in time, as in DWI, information theoretic metrics might fail as they lack spatial context and their estimation is problematic. Because of that, the consideration of local anatomical structures could be helpful, such as the employment of geometric features to retain structural details throughout the course of registration, i.e., 3D moment invariants, encapsulated in the form of attribute vectors, to describe the anatomical structure in the vicinity [235]. However, in DWI the intensity range in images acquired by a high b-value (b-value $> 100s/mm^2$) is significantly reduced, as one can notice in Figure 3.1. Thus geometric features are difficult to be extracted accurately on those raw images. On the other hand, knowing the physics behind the image acquisition process, one could exploit the fact that intensity changes are expected to behave according to a low-dimensional acquisition model. Finally, local evaluations of similarity measures are advantageous as they render the optimization more robust to local intensity changes provoked by imaging artifacts.

Furthermore, regarding the reference frame, an explicit choice of a specific image (preferably the first image in the sequence) to use it as a template should be a valid strategy for certain applications, such as the case of motion

correction in dynamic MRI. This latter assumption is motivated by the fact that the images in such an image sequence are acquired sequentially, in a short period of time, from the same patient. Therefore, we wouldn't expect them to differ drastically in terms of the underlying anatomic structure (we expect local, non-linear rather than global, linear transformations to have been occurred). Using one of the images in the sequence as a template reduces the dimensionality of the feature space in which the objective function and the optimization are computed. In the same time though, a computationally efficient group-wise registration scheme without the need of choosing a reference image would be even more appropriate, as it avoids the undesired introduction of bias with respect to the a priori chosen template, though being challenging.

Based on the above conclusions, our first remark urges us to believe that the matching criterion should be based only on a model that best describes the physics of the image acquisition protocol. Embedding such a model into dynamic image registration directly results in corrected parameters of interest. Moreover, we are interested in examining the potentiality of designing a group-wise registration scheme without the need of choosing a reference template while being computationally efficient. We therefore propose an unbiased template-free IRG registration method, in which all the images in the sequence are deformed and registered into an unknown consensus space. We aim at finding the optimal deformation fields of the diffusion-weighted magnetic resonance (DW) images using a temporal constraint, related to the diffusion process, as well as a smoothness penalty on the deformations. These entities are modeled subsequently by Markov Random Fields (MRF) and solved by an efficient discrete optimization technique. The latent variables of the model are m -deformations (B-spline polynomials) of the images, which are obtained using the discrete formulation introduced in [57]. The deformation variables are connected with the observations towards ensuring meaningful temporal correspondence among the DW images. They are also inter-connected in order to decrease the cost of comparisons between individual images. This latter inter-connection is due to a high-order dependency among the images, relative to the physiological process taking place during image acquisition. Our work was inspired by the approach of [189]. The main difference between the two approaches is found in the encoding of the global similarity of the population. A statistical compactness criterion has been used in [189], whereas we incorporate within the registration process a physiological model representing the temporal intensity change. This intensity modeling step removes the ambiguity during the search of anatomic correspondences and thus increases the mapping accuracy.

In the remainder of this chapter, we present our first group-wise registration method that destines for motion compensation in DWI. Our method is modular and could be also used in other 4D MRI sequences, by incorporating

a different global similarity metric, which can be straight-forward. In the first section of this chapter, a review on the existing registration methods on 4D MRI is presented. Then in section 3.2, we are presenting the proposed deformable group-wise image registration method, designed to be used for registering dynamic images in 4D MRI. More specifically, we are going to discuss how to formulate the registration problem as energy minimization by considering discrete deformation elements and show that we can optimize the previous energy in a discrete optimization setting. In 3.3 the experimental validation is presented. Finally, in section 3.4, a discussion concludes the chapter.

3.1 Prior Work

There is a great amount of work on this specific problem, with most of the published methods been mentioned in the previous chapter already. However, we would like in the section to summarize their main differences and limitations. One of the first approaches was the work of Bidaut and Vallée [21], who used the end-exhale image of a sequence of myocardial perfusion MRI as a reference image to which all the rest were registered, however the fact that rigid transformation was assumed to model the complex motion of the heart is a significant limitation of that early work. Rigid-body transformation was assumed also by [247] to correct for motion in brain perfusion MR images. On the other hand, Huizinga et al. [81] proposed a groupwise non-rigid registration method, which could be applied for motion compensation in various time-resolved MRI datasets. They exploited that intensity changes are expected to behave according to a low-dimensional acquisition model, which they claim is typically the case in time-resolved MRI. By assuming every time a specific acquisition model that could predict the intensity variation in time for the specific dataset, their method was applied to modified Look-Locker inversion recovery (MOLLI) T1 mapping in an infarcted porcine myocardium, black-blood variable flip-angle (VFA) T1 mapping in the carotid artery region, and ADC mapping in the abdomen. In each case, a correlation matrix of the datapoints in the model is defined and subsequently, dimensionality reduction (through PCA) is applied on the dataset, based on this correlation matrix. Then a dissimilarity measure is proposed based on the idea that when motion is present in the images, the data no longer adheres to the presumed acquisition model and the eigenvalue spectrum of the correlation matrix changes. Regarding the deformation field they used a B-spline transformation model that could account for the non-rigid deformations. However, their method proved to be superior to a similar group-wise registration approach based on MI only on one of the three datasets (MOLLI), maybe mainly due to the fact that the proposed dissimilarity metric is based on the selection of a optimal number

of eigenvalues capturing the highest percentage of data variance, which is use-defined and thus highly subjective.

Hamy et al. [72] also used PCA for motion correction, but they used PCA in another way, in order to obtain the low-rank data components, whereas they used a residual complexity measure for registration. The iterative use of PCA combined with a standard registration algorithm was first introduced by Melbourne et al. [136, 137]. The concept is that in PCA, contrast changes are assumed to appear in the more significant principal components and motion in the less significant. However, the ability of PCA to disentangle motion from contrast enhancement depends on the nature of motion, e.g. the periodic motion of free breathing can appear in the more significant principal components along with contrast changes. Milles et al. [141] used Independent Component Analysis (ICA) to compensate rigid heart motion in perfusion scans. More recently, Wollny et al. [229] investigated the use of independent component analysis to decompose data prior to registration in free breathing cardiac MRI. In this case too, the objective is to remove motion elements to form a synthetic target time-series. The method performed better than the one published by the same author earlier, that was based on exploiting the quasiperiodicity in motion correction of free-breathing myocardial perfusion MRI [230]. Still the performance of the method in [229] heavily depends on the ability of ICA algorithm to create synthetic reference images that are related to motion, in order to be used in the registration framework as templates, as well as the fact that it is a supervised method.

In the same line, several pieces of work address this intensity variation problem by using an enhancement-driven synthetic sequence to specify the target image for all the frames. In Buonaccorsi et al. [29] and Adluru et al. [1] the intensity-time curve at each pixel is fitted to a dynamic contrast-enhanced MRI model [206]. Accordingly, the observed sequence is rigidly registered to the resultant synthetic series which is assumed to be free of motion. These model-based registration methods have the limitations that the fitting is complex and an input function of the contrast agent concentration in the arterial supply is required. Stegmann and Larsson [192] proposed to register perfusion sequence by using Cluster-aware Active Appearance Model which is built from an annotated training set. Towards defining a more appropriate target image for group-wise registration in myocardial perfusion MRI, Li et al. [115] estimate a pseudo ground truth of the image sequence. Their goal was to compute a reference sequence that would have been acquired without being affected by motion or noise during acquisition. To this end, they use segmentation information to impose spatiotemporal smoothness on the ground truth image. The main limitation though of their method lies on the iterative optimization scheme, that increased computational complexity. Thus, on one hand introducing the pseudo ground truth overcomes the intensity variation problem, on the other hand though, the

energy functional of non-rigid registration is not minimized in one attempt, but in an iterative coarse-to-fine manner. Spatiotemporal smoothness was also taken into account by Metz et al. [138] in their proposed group-wise registration method. The authors consider a Lagrangian $nD + t$ B-spline transformation model. The similarity metric used minimized the intensity variances over time and constrained optimization using stochastic gradient descent method with adaptive step size estimation was incorporated in their framework. Regarding the constraints on the deformations, the popular zero average displacement constraint was taken into account [19, 12].

The most popular metric for registering images with different intensity distribution is probably the Normalized Mutual information (NMI) [124, 173]. Hamrouni et al. [71] proposed an efficient, unsupervised group-wise registration method for cardiac perfusion MRI (p-MRI) exams based on novel kNN-estimators of Shannon information measures between high-dimensional first-pass curve (FPC) distributions. However, they assumed an affine motion in their experiments, while cardio-thoracic motions are more complex. The use of a non-rigid deformation model is more appropriate and that would increase the demand on computational efficiency. Zheng et al. [248] developed a new method based on FFD in order to register breast images. In this approach a Lorentzian estimator is used as a similarity measure, combined with a reformulation of the energy function minimization using linear programming. An interesting new sparsity-promoting metric for group-wise elastic registration in cardiac perfusion MRI was recently proposed by Cordero-Grande et al. [41], which according to the authors it can be understood as a compromise between a pairwise sequential registration and a pure group-wise registration (i.e., one in which the order of the metric samples is not considered in the metric design).

In terms of calculating specifically an ADC map without motion artifacts, thus working on a DWI data set, two group-wise registration methods have been proposed in [67] and [211]. However, the registration process in the former is based on pair-wise connections between the images, whereas in the latter one the proposed group-wise registration requires prior structure segmentation, making it a not fully-automated framework. Furthermore, both methods use mutual information criterion for image similarity, without taking into account the intrinsic intensity changes in DW-MRI due to the diffusion process. Finally, in both these studies, group-wise image registration and ADC parameter estimation were treated as two separate problems.

To conclude this literature review, it is worth mentioning that in all the afore-mentioned studies, the group-wise approach yielded always better results than the pair-wise one, whenever such a comparison was made.

3.2 Proposed Method

Let us consider m images $\{s_1, \dots, s_m\}$, where each image is described by intensity values $s_i(x)$, with $x \in \Omega_i$, Ω_i being the domain of image s_i (\mathbf{R}^3). We are looking for a set of transformations $T = \{T : x_R = T_i(x_i), i = \{1, \dots, m\}\}$ which map mutually corresponding points from the m -image spaces to the same point of a reference frame Ω_R . This mapping aims to correct deformations due to anatomical differences or motion, in order to identify intensity differences in time due to change in the measured quantity. The reference pose would then correspond to the consensus geometrical space, in which the ADC map resides.

As mentioned in the discussion part of the second chapter, we opt for an interpolation-based transformation model and a discrete optimization strategy. In the same time, we want to incorporate into the registration framework a physiological model that describes the change of the measured physiological quantity in time. In this section, we introduce in the energy formulation the deformation and the physiological model and decompose the continuous problem in discrete entities.

3.2.1 Physiological Model

We assume that the intensity values of the images depend mainly on the amount of signal loss occurred during the application of the two equal rectangular gradients before and after the 180° -refocusing pulse [15]. The relation between the signal attenuation expressed by the signal intensity \hat{s} and the diffusion of the water molecules in a microscopic level is well known to be exponential [111]. Having acquired the images with high b-values ($> 50s/mm^2$), we can assume that our diffusion-weighted data are insensitive to vascular capillary perfusion and diffusion is the only type of motion present, thus the ADC is equal to the water diffusion [95]. Therefore the relation between ADC and the signal intensity at each voxel location can be modeled as:

$$\hat{s}_i(x) = e^{-b_i \cdot ADC(x)} \quad (3.1)$$

where b_i is the b value used for the acquisition of image \hat{s}_i . In case of m b-values images, the ADC can be calculated as the slope of a line fitted on the plot of the logarithm of the relative signal intensities of the tissue against the b-values. The ADC would then be:

$$ADC(x) = \frac{\sum_{i=1}^m (b_i - \bar{b})(y_i(x) - \bar{y}(x))}{\sum_{i=1}^m (b_i - \bar{b})^2} \quad (3.2)$$

where $y_i = \ln s_i$ and \bar{b} , \bar{y} the mean b-value and mean of $\ln s$ respectively.

3.2.2 Deformation Graph-based Model

We used the popular Free Form Deformations transformation model, described in subsection 1.2.3 of the first chapter, to parametrize each transformation $T(x)$ by a linear combination of K control points, weighted using cubic B-splines. In the end, we have m uniformly distributed grids of control points over the image domain (one corresponding to each 3D image).

3.2.3 Temporal Global Comparison

The first term of the objective criterion to be minimized is the global term that relates to the exponential fitting error of the physiological model. We introduce the following global measurement towards group-wise registration in DWI:

$$E_{data}(T_1, \dots, T_m) = \iiint_{\Omega_R} \rho(s_1(T_1^{-1}(x)), \dots, s_m(T_m^{-1}(x))) \quad (3.3)$$

with ρ being the metric used to assess a global cost for any displacement that causes an increase on the exponential fitting error of the physiological model, among the images in the sequence. The key idea behind the proposed dissimilarity measure is that, when motion is present in the images, the data no longer adheres to the presumed afore-described physiological model. Therefore, the intensity values of the deforming images at corresponding coordinate locations are expected to fit better on the physiological model than the corresponding values of the unregistered sequence. In that way, we impose consistency on the computation of the physiological model. It should be expected that as the images are jointly aligned, the derived optimal pose would express more accurately the diffusion process, enabling the computation of more accurate ADC maps. More specifically, we propose the sum of squared errors of prediction (SSE) for the global measurement towards global registration in DW images. In that case the metric ρ would be:

$$g(s_1, \dots, s_m) = \sum_{i=1}^s (s_i - \hat{s}_i)^2 \quad (3.4)$$

where \hat{s}_i is calculated by equation 3.1 for the current estimate (fitted values) ADC. Such an objective function introduces the inverse transformation, that is challenging from theoretical and practical point of view when referring to deformable deformation. An alternative criterion that can be considered is using the forward transformations and measuring the similarity of the images on the intersection of the deformed images, or

$$E_{data}(T_1, \dots, T_m) = \int \dots \int_{\Omega_1 \cup \dots \cup \Omega_m} \phi(T_1(x), \dots, T_m(x_m)) \rho(s_1(T_1(x_1)), \dots, s_m(T_m(x_m))) dx_1, \dots, dx_m \quad (3.5)$$

where ϕ is a Dirac-driven function whose role is to define which voxel corresponds to the same position at the reference pose defined as follows: $\prod_{i,j} \in [1, m] \times [1, m] \delta_\alpha(|x_i - x_j|)$.

3.2.4 Deformation Smoothness Constraints

Medical images capture properties of spatially continuous anatomical structures, therefore it is natural to assume that the deformation applied to them should be locally smooth. Opposite to the former cases, this constraint should be applied to each grid separately. This constraint can be defined on the grid as

$$E_{smooth}(T_1, \dots, T_m) = \sum_{i=1}^m \iiint_{\Omega_i} \psi(\nabla T_i(x_i)) dx_i \quad (3.6)$$

where ψ is a convex function imposing smoothness.

The optimal parameters of the deformation should be determined through the minimization of an objective function being composed of the above terms. The complete term associated with the registration problem is then defined as the sum of the data and smoothness term, or

$$E_{TOTAL} = E_{data} + E_{smooth}. \quad (3.7)$$

Recovering the deformation parameters is challenging due to the high dimensional parameter space and the non-convexity of E_{TOTAL} . The most common way to obtain the transformation parameters is through the use of a gradient-descent method in an iterative approach. Given an initial guess, one then updates the estimate according to the following formula $[T^i = T^{i-1} - \delta_t \frac{E_{TOTAL}}{\partial T}]$. However such a process doesn't guarantee the recovery of the global minimum and it is computationally inefficient. Moreover, it involves the derivative of the similarity metric with respect to the transformation parameters and therefore it is model and matching criterion dependent. Graphical models and the off-the-shelf discrete optimization methods being associated to them can address the above mentioned constraints.

3.2.5 Objective Function: MRF-based Energy Formulation

In order to be able to use discrete optimization schemes, the deformation space should be quantized. Let $\Theta = d^1, \dots, d^q$ be a quantized version of a plausible deformation field, then a discrete set of labels $\mathcal{L} = l_1, \dots, l_q$ can be corresponded to it. A label assignment l_p^ξ , where $\xi \in 1, \dots, q$, to a grid node p is associated with displacing the node by the corresponding vector $d^{l_p^\xi}$. If a

label is assigned to every node we get a discrete labeling l . The displacement field associated with a certain labeling l becomes $D(x) = \sum_{p \in G} \eta_p d^{l_p}$.

By applying this quantization of the deformation space one would like to reformulate the problem as a discrete multi-labeling problem. A common model for representing such problems are Graphical Models and MRFs. For every control point in the deformation grid superimposed onto image s_i , there is a node p_i that represents its displacement ($p_i \in \mathcal{V}$, with \mathcal{V} denoting the set of all nodes that encode the latent variables). In the context of group-wise registration for motion correction in DWI, the graphical model will involve two types of dependencies. The first one relates to the fitting error of the physiological model and is applicable only on cliques connecting nodes on different grids (high-order, inter-image dependency). This global cost is the most challenging case, due to the fact that in order to be properly determined it requires higher order cliques. The adoption of higher order cliques is possible within MRFs, however their use decreases significantly their computational efficiency. For this reason, we consider an approximation of the global cost described later. We avoid the use of high-order cliques and instead convert the high-order term to singleton and pair-wise cliques. Finally, the second type of dependencies relates to the smoothness constraint and is applicable only on edges connecting nodes on the same grid (pair-wise, intra-image dependency) (see Figure 3.2).

The main challenge of discrete optimization methods is the quantization of the search space since it seeks for a compromise between computational complexity and the ability to capture a good minimum. This can be achieved through a compositional approach, where the final solution is obtained through successive optimization problems with respect to the deformation increment towards minimizing the objective function (Glocker et al. [57]). Thus, by keeping the set of the labels in a reasonable size it becomes possible to approximate the optimal solution in an efficient way.

Energy terms: The constructed graph is associated with an energy, consisting of three terms, a global unary term and two pairwise terms:

$$\begin{aligned}
 E_{MRF}(T_1 \circ G_1, \dots, T_m \circ G_m) &= \lambda_{global} \sum_{i=1}^m \sum_{p \in G_i} V_p(l_p) \\
 &+ \lambda_{inter} \sum_{i=1}^m \sum_{p \in G_i} \sum_{q \in (N(p) \setminus G_i)} V_{pq}(l_p, l_q) \\
 &+ \lambda_{intra} \sum_{i=1}^m \sum_{p \in G_i} \sum_{q \in (N(p) \cap G_i)} V_{pq}(l_p, l_q)
 \end{aligned} \tag{3.8}$$

where $V_p(\cdot)$ are the unary potentials, $V_{pq}(\cdot, \cdot)$ are the pair-wise potentials and N represents the connectivities of the nodes (see a representation of the edges in figure 3.1). Three different constants, λ_{global} , λ_{inter} and λ_{intra} are used to

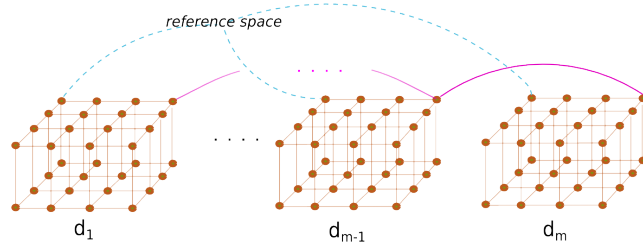


Figure 3.1: Representation of the edges of our proposed MRF-based group-wise registration scheme. The node and the edge system of all the connected graphs. With brown color we represent the relationship within the grid nodes belonging to each of the deformation fields (intra connections). Finally, the pink edges denote the temporal relationship (which can be either of high-order or a pair-wise connection) between successive deformation fields (inter relationship).

weight the three different types of potentials. The optimal values of the aforementioned weights were empirically determined in a brute force approach. The optimization of such an energy is non-convex, however the optimizer we used provides guarantees for an almost optimal solution to such an NP-hard MRF problem [101].

Global Unary Term: We approximate a global cost for the deformations by assuming that for each node p of a given deformation field/image s_i , the rest of the images do not get deformed within the current iteration. This assumption is considered for all nodes and for all deformation fields within a given iteration, an assumption that is common in minimizing graphical models through expansion moves. In this case, the cost of a deformation depends only on the label of this node:

$$V_{p_i}^t(l_{p_i}) \approx \int \dots \int_{\Omega_1 \cup \dots \cup \Omega_m} \hat{\omega}_{p_i}(x_i) g(s_1(T_1^{t-1}(x_1)), \dots, s_i(T_i^t(x_i)), \dots, s_m(T_m^{t-1}(x_m))) \quad (3.9)$$

where $\hat{\omega}(\cdot)$ is the support function that determines the contribution of the point x on image i to the unary potential of the control point p of the corresponding grid i . By $g(\cdot)$ we define the metric used to assess a global cost for each possible displacement l of a control point.

As mentioned earlier, the objective criterion we propose to be minimized for the case of DWI registration, is the sum squared exponential regression fitting error among the images in the sequence, in order to impose consistency on the computation of the physiological model. It should be expected that as the images are jointly aligned, the derived optimal pose would express more accurately the diffusion process, enabling the computation of more

accurate ADC maps. In that case the metric g would be:

$$g(s_1, \dots, s_m) = \sum_{i=1}^m (s_i - \hat{s}_i)^2 \quad (3.10)$$

where \hat{s}_i is calculated by equation 3.1 for the current estimate (fitted values) ADC.

Inter-image Pair-wise Term: We consider a second term related to the observations, meaning the intensities of the images, that aims to reduce the outlier effect. To this end, local pair-wise comparisons between members of the population are examined too. We assume that two images (for example images i and j) are allowed to be deformed, while the rest $m - 2$ remain static within the current iteration. The SSE criterion is used to calculate the cost of a deformation, as expressed by the following pair-wise term:

$$\begin{aligned} V_{p_i q_j}(l_{p_i}, l_{q_j}) &\approx \int \cdots \int_{\Omega_1 \cup \cdots \cup \Omega_m} \omega_{p_i}(x_i) \\ &[(s_1(T_1^{t-1}(x_1)) - f(x_1))^2 + \cdots + (s_i(T_i^t(x_i)) - f(x_i))^2 \\ &+ (s_j(T_j^t(x_j)) - f(x_j))^2 + \cdots + (s_m(T_m^{t-1}(x_m)) - f(x_m))^2] \\ &dx_1 \cdots dx_i dx_j \cdots dx_m \end{aligned} \quad (3.11)$$

The inter-image pair-wise comparisons are performed only between the immediate neighbors in the temporal domain.

Deformation Smoothness Constraints: In order to impose local smoothness to the deformation fields, we used the same smoothness constraint used in [189], which is performed by penalizing the magnitude of displacement vector differences. This constraint was applied to neighboring nodes that belong to the same deformation field assuming a 26-nodes intra-image connectivity.

3.2.6 Optimization and implementation details

Once the objective function is defined, the optimal solution can be obtained by performing inference via Maximum a posteriori (MAP) estimation, which in a discrete MRF model it is equivalent to minimizing the MRF energy, as the afore-mentioned ones. The solution will be a set of optimal deformations $\hat{d}_1, \dots, \hat{d}_m$ defined as:

$$\hat{d}_1, \dots, \hat{d}_m = \arg \min_{d_1, \dots, d_m} E_{MRF} \quad (3.12)$$

Discrete optimization of MRFs is, in general, an NP-hard problem [185]. However, in special cases, it can benefit from very efficient solutions. The trivial brute force algorithm (i.e. trying all possible combination of labels

for each and every variable) has an exponential complexity that makes such an approach unsuitable. More efficient algorithms have been developed during the last two decades which boosted the use of graphical models in the field of computer vision [91]. In our work, we used an algorithm of discrete optimization, that has is based on principles from linear programming and primal dual strategies, while at the same time generalizes α -expansion (FastPD, [101]). FastPD can be classified as both a max-flow and move-making algorithm, as well as an message passing method. The former class of discrete optimization algorithms make use of the well know max-flow min-cut [26] algorithm from graph theory, which can optimally solve some instances of discrete energies. These methods are usually combined with greedy strategies that iteratively minimize over the label space by solving a sequence of max-flow min-cut sub problems. On the other hand, in message passing methods, messages are calculated and propagated between nodes in a graph. This propagation can be seen as a re-parametrization of the original problem aiming to establish special properties in the re-weighted function that makes inference easier. One of the main advantages of FastPD is its modularity/scalability, since it deals with a much wider class of problems than α -expansion, being an order of magnitude faster while providing the same optimality guarantees when performing metric labeling [100].

FastPD solves a serie of max-flow min-cut problems on a graph. In that sense, it is similar to α -expansion which also performs MAP inference on multi-label problems by solving successive binary max-flow min-cut problems. The main difference between these approaches is the construction of the graph where max-flow min-cut algorithm is applied. α -expansion constructs the binary problem by restricting the label space, so that the only options for a given variable are to remain in its current assignment, or to take a label α (which varies in every iteration). Instead, FastPD constructs these binary problems by performing a Linear Programming Relaxation (LPR) of the integer program that represents the discrete MRF formulation. It builds upon principles drawn from the duality theory of linear programming, applying the well known primal-dual schema to the relaxed version of the MRF integer programming formulation.

For the sake of clarity, let us explicitly show how we can cast a standard MAP inference problem on a pairwise MRF as an integer program [98]. We

define the following integer program:

$$\begin{aligned}
\min \quad & \beta_{unary} \sum_{i=1}^m \sum_{p \in G_i} \sum_{l \in \mathcal{L}} V_{unary}(l_p) y_p(l_p) \quad + \\
& \beta_{inter} \sum_{i=1}^m \sum_{p \in G_i} \sum_{q \in (N(p) \setminus G_i)} \sum_{l \in \mathcal{L}} V_{inter}(l_p, l_q) \lambda_{pq}(l_p, l_q) \quad + \\
& \beta_{intra} \sum_{i=1}^m \sum_{p \in G_i} \sum_{q \in (N(p) \cap G_i)} \sum_{l \in \mathcal{L}} V_{intra}(l_p, l_q) \lambda_{pq}(l_p, l_q)
\end{aligned} \tag{3.13}$$

s.t.

$$\sum_{l \in \mathcal{L}} \lambda_p(l_p) = 1 \quad \forall p \in G_i \tag{3.14}$$

$$\sum_{l_p \in \mathcal{L}} \lambda_{pq}(l_p, l_q) = \lambda_q(l_q) \quad \forall l_q \in \mathcal{L}, \forall p \in G \wedge q \in (N(p) \setminus G_i) \tag{3.15}$$

$$\sum_{l_q \in \mathcal{L}} \lambda_{pq}(l_p, l_q) = \lambda_p(l_p) \quad \forall l_p \in \mathcal{L}, \forall p \in G \wedge q \in (N(p) \setminus G_i) \tag{3.16}$$

$$\sum_{l_p \in \mathcal{L}} \lambda_{pq}(l_p, l_q) = \lambda_q(l_q) \quad \forall l_q \in \mathcal{L}, \forall p \in G \wedge q \in (N(p) \cap G_i) \tag{3.17}$$

$$\sum_{l_q \in \mathcal{L}} \lambda_{pq}(l_p, l_q) = \lambda_p(l_p) \quad \forall l_p \in \mathcal{L}, \forall p \in G \wedge q \in (N(p) \cap G_i) \tag{3.18}$$

$$\lambda_p(\cdot), \lambda_{pq}(\cdot, \cdot) \in 0, 1 \tag{3.19}$$

In this formulation $\lambda_p(\cdot)$ and $\lambda_{pq}(\cdot, \cdot)$ are indicators for the discrete labels l_p assigned to each node p , used to linearize the MRF energy. A binary variable $\lambda_p(l_p)$ is equal to 1 when node p chooses label l_p . The same holds for the pairwise case $\lambda_{pq}(\cdot, \cdot)$. Equation 3.14 guarantees that every variable is labeled with only one label at a time, while equations 3.15 to 3.18 keep consistency between variables $\lambda_p(\cdot)$ and $\lambda_q(\cdot)$. This integer formulation is still an NP-hard problem, given the integrality constraint expressed in equation 3.19. Therefore, this integer program becomes a standard linear program when this constraint is relaxed, by allowing variables $\lambda_p(\cdot)$ and $\lambda_{pq}(\cdot, \cdot)$ to take continuous positive values.

The aforementioned linear program task is used by FastPD as the primal problem, while the dual of the resulting LP is used as the FastPD dual problem. Then, the primal-dual schema is iteratively applied. At every iteration, a max-flow min-cut problem is solved, improving both primal optimality and dual feasibility. FastPD provides good balance between efficiency and accuracy and that's the reason it was chosen as the optimization scheme for optimizing the afore-described energy.

Our algorithm follows a coarse-to-fine process that first estimates pa-

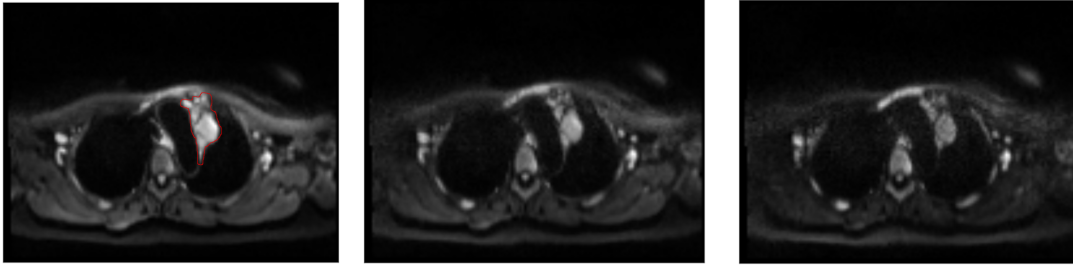


Figure 3.2: DW images of a patient from the dataset.

An axial slice of the 3D image of a patient, with b values of 50, 400 and 800 s/mm^2 (from left to right). The red contour in the b-value=50 image corresponds to the tumor's contour, as it was drawn by the expert.

rameters at a coarse spatial image resolution level and then updates the solution to a finer resolution level. We applied a multi-resolution scheme with 3 resolutions levels; two levels in which the joint problem is solved and one at full image resolution in which only the appearance model is optimized, keeping the previously obtained deformation fields fixed. The rationale behind this multi-resolution approach is that we want to adopt the grid size to the information content (frequencies) of the modeled variables, i.e. a sparse grid for the deformation model to cope with potential rigid transformations, a mid-level grid for local deformation and global intensity variations and a last dense grid for local intensity changes. Finally, regarding the run-time performance of the method, all the experiments were computed on a 8-cores machine (3.6 GHz processing power) with a memory requirement of 4 GB.

3.3 Experimental Validation

In order to validate the proposed registration method, we used a data set provided by the Centre Hospitalier Universitaire Henri-Mondor, France. The data set consisted of 3D images of twenty-five (25) different patients with lymphoma, scanned with a 3 Tesla MRI scanner using 3 b values: 50, 400 and 800 (s/mm^2). Therefore, the sequence of the images to be registered was always of size 3 ($m = 3$) per patient (see figure 3.1 as an example of such a sequence belonging to one patient). Both male and female patients were included. The image size was 130x106x22 for every patient, with a pixel resolution of 2.46x2.46 mm^2 in the axial plane and 5 mm^2 in the z-axis. Each image had been manually annotated by experts to indicate the contour of the tumor.

We compared the proposed method against two other modelling criteria: the sum of absolute intensity differences (SAD), which is appropriate when the intensity values of the deforming images come from the same distribution (under the presence of noise), and an entropy-based criterion, applicable in multimodal image registration. These two criteria were implemented in Eq.(3.9) and Eq.(3.11). Specifically, for the latter criterion, the entropy

estimator based on spacings [25] was used in Eq.(3.9), whereas mutual information (MI) was used in the inter-images comparisons (Eq.(3.11)).

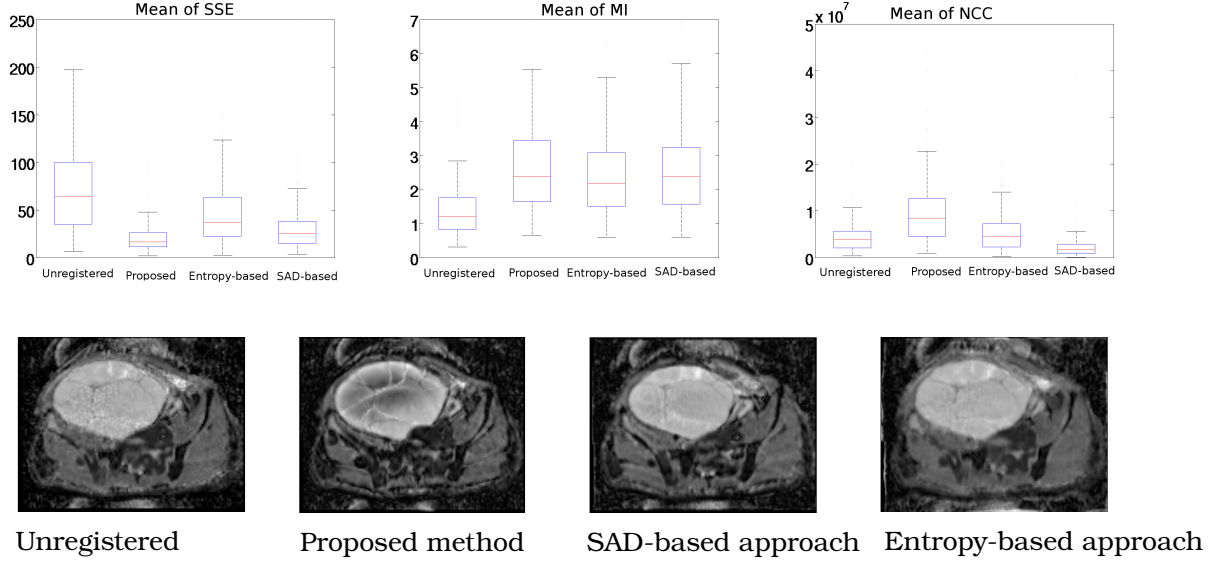


Figure 3.3: Results on three different criteria for validating each method, applied on DW images. *First row:* Boxplots of statistics (mean) of SSE by fitting the physiological model, MI and NCC respectively. *Second row:* ADC map (same axial slice as in figure 3.1) derived without registration and with the examined registration methods.

The performance of the seven registration approaches was quantitatively assessed by examining three different validation criteria: the fitting to the diffusion model error, meaning the sum squared error (SSE) between the fitted, by the diffusion model (see Eq.1) and the real data, the MI and the normalised cross-correlation (NCC), averaged across pairs of the population. The mean SSE is computed as: $SSE_{mean} = \frac{1}{|\Omega|} \sum_{x \in |\Omega|} (\hat{s}_t(\mathbf{x}) - \mathbf{s}_t(\mathbf{x}))^2$, in case of unregistered images and $SSE_{mean} = \frac{1}{|\Omega|} \sum_{x \in |\Omega|} (\hat{s}_t(\mathbf{x}) - \mathbf{s}_t(\mathbf{x}) \circ \mathbf{D}_t(\mathbf{x}))^2$ in case of the registration methods, where $\hat{s}_t(\mathbf{x})$ the fitted value. The standard deviation of SSE is computed as: $SSE_{std} = \frac{1}{|\Omega|} \sum_{x \in |\Omega|} ((\hat{s}_t(\mathbf{x}) - \mathbf{s}_t(\mathbf{x})) - SSE_{mean})^2$, in case of unregistered images and $SSE_{std} = \frac{1}{|\Omega|} \sum_{x \in |\Omega|} ((\hat{s}_t(\mathbf{x}) - \mathbf{s}_t(\mathbf{x}) \circ \mathbf{D}_t(\mathbf{x})) - SSE_{mean})^2$ in case of the registration methods. The proposed method outperformed the two other registration implementations in all three validation criteria, irrespectively of the similarity criterion used within the other frameworks. This result can be justified by the fact that the other methods do not use the right data term that models the temporal intensity change; thus a sub-optimal solution is reached. Moreover, in order to qualitatively evaluate the results, the ADC map is shown for the same axial view of the patient used in figure 3.2, as derived by the three registration scenarios, as well as without registration (common in clinical practice). It can be seen that the ADC map calculated after registering the DW-MR images with our proposed method

reveals anatomical structure and highlights the spatial tissue heterogeneity. Part of our current work includes the simulation of diffusion-weighted images, which will allow us to better validate and compare the different approaches.

3.4 Discussion

In this paper, we propose a novel deformable group-wise registration method that derives an optimal representation for shape and intensity change towards more accurately estimating the underlying pathology. Experimental results on DW images demonstrate that the derived by this approach ADC map preserves structure, as it can be seen inside the big cyst superior to the tumor shown in Figure 3.8, and reveals tissues boundaries (tissue heterogeneity, anatomical structure). Moreover, based on the quantitative results presented in the previous section, one can conclude that the best performing methods are actually those that use the fitting to the diffusion model criterion in their formulation. A limitation of the proposed method is that it doesn't examine simultaneously the interaction among all the deformation fields of the population towards a global consistency on the physiological model. Such a global term would require the adaptation of high order inter-image cliques. Therefore, a group-wise registration method that includes high-order dependencies among the images would be a promising research direction for future work.

Chapter 4

Joint Deformable Registration and Diffusion Estimation

In the previous algorithm, we didn't impose any spatial constraint on the computation of the parametric map. It should be expected though that the values of the measured parameter do not vary a lot within the same tissue. The physiological model presented in the previous chapter doesn't guarantee within tissue spatial smoothness. When noise is present in the image sequence, not only registration might not be able to cope with it, it might be even affected by that source of noise and result in a sub-optimal local deformation on the relevant anatomic region. The elimination of such outliers on a parametric map is crucial due to the fact that they might bias any statistical analysis performed on ROIs on the map, based on which tissues/tumors could be characterized.

As in the case of segmentation and registration, the problems of group-wise registration and quantized parameter estimation in time-evolved image sequences, such as in quantified MRI, are traditionally approached individually. However, the accuracy of one is of great importance in influencing the success of the other. In order to accurately quantify the physiological process during image acquisition, we propose and present in this chapter a joint deformable registration and appearance model computation framework, that simultaneously registers the spatiotemporal images and models the spatiotemporal physiological process. The key idea behind a simultaneous parameter estimation is that registration and physiological parameter estimation can naturally benefit a great deal from each other. We define a deformation and an appearance model: the deformation model maps each one of the m spatiotemporal images in a common space (the quantitative parameter's space), whereas the appearance model describes the signal intensity related to the quantitative parameter, which in the current paradigm is the diffusion of water molecules that takes place during DWI acquisition. The unknown variables of the combined deformation and appearance model correspond to a $m + 1$ -layer graphical model, m layers that represent the

m 3D deformation fields, one for each DW image, and an extra layer for the parameter of the appearance model, namely the 3D ADC map. The latent deformation variables are obtained using the discrete formulation introduced in [57]. The layers are interconnected in order to achieve consistency between the predicted diffusion (by the appearance model) and the diffusion calculated by the registered DW images. Each deformation field depends thus on the appearance model. Spatial smoothness constraints on the parameters of the appearance model and the deformations are imposed through pairwise interactions. Moreover, the m layers deformation fields have pairwise interconnections (based on proximity of b-values) towards imposing smoothness on the change of deformation through time (the images sequence is acquired with increasing b-values).

Our approach is very close to the work of Bhushan et al. [20] on jointly estimating the pharmacokinetic parameter and co-aligning DCE-MR images, with the main difference being the fact that no spatial smoothness was imposed in that work (the prior distributions on deformation and pharmacokinetic parameters are uninformative), while they applied a continuous optimization scheme (Gauss-Newton optimization), instead of a discrete one, as it is the case in our work. It also lies between frameworks of concurrent segmentation and registration [236], [242], [151], [5] and image reconstruction and modeling [163], [154]. The main difference of our approach with respect to the concurrent segmentation and registration works is that, our ADC variables are continuous and have unique values on a voxel-wise basis, whereas segmentation labels are discrete and common within regions. In that sense, methods for image reconstruction [163] and denoising [159] are closer to our approach; those however are defined in a single spatial domain and do not require deformable image registration. On the other hand, methods for recovering appearance change and motion in image sequences target a similar goal, but they account usually for global motion or smooth deformations, as well as systematic changes in appearance exhibiting spatial or temporal structure that can be modeled [22]. Intensity changes in domain-specific cases are captured by learning models using training examples. Such training images are not available in our case where the tumor appears in different areas of the body.

By elaborating more on concurrent segmentation and registration frameworks, we aim at finding the optimal deformation fields of the DW images together with the optimal ADC values in a one-shot optimization approach. Alchatzidis et al. [5] proposed a joint group-wise registration and segmentation method for brain atlas selection, but they optimized the deformation fields iteratively, whereas Sotiras et al. [189] didn't include a segmentation layer in their group-wise, one-shot registration method. In our case the one-shot optimization problem imposes additional challenges. To this end, linear programming and duality [101] is used to determine the optimal solu-

tion to the joint problem. It is also worth to mention that our framework is modular with respect to the registration/annotation grid and can be adapted to the application domain. Finally, to the best of our knowledge, we are the first to propose a DWI registration scheme that optimizes explicitly the derived ADC map. Very recently, two other works of DWI registration were published [67], [211] aiming at computing the ADC without motion artifacts. Guyader et al. [67] examined the influence of pairwise registration on the ADC calculation, while Veeraraghavan et al. [211] proposed a group-wise DWI registration method that requires structure segmentation, thus is not completely automated. Both methods (i) use mutual information criterion for image similarity which is less appropriate than the fitting error to a diffusion model we are using. (ii) calculate the motion for each image independently without considering temporal consistency (smooth transition in time) and (iii) extract the ADC by voxel-wise curve fitting from the warped images without accounting for spatial constraints.

In the remainder of this chapter, a review on joint estimation approaches on various medical image analysis studies is presented in 4.1. Then in section 4.2, we are going to discuss how to formulate the joint problem as a Bayesian MAP estimation, based on which we are going to discuss how to formulate the problem as energy minimization by considering discrete deformation elements and parametric values. Furthermore, the experimental validation is presented in section 4.3. In section 4.4, a discussion concludes the chapter.

4.1 Prior Work

A typical Medical Image Analysis framework consists of various tasks, since an optimal interpretation of medical images requires an integration of the medical images. Integration (or image fusion) consists most of the times of two steps: (co-)registration and integrated display (or presentation, or visualization), where the registered monomodality/multimodality information is rendered. This second step implies some form of image segmentation or classification, whereas in case of tumor or organ detection, a detection task is incorporated into this step. Moreover, in case the examined imaging is subject to high temporal noise, e.g. Time-of-Flight Imaging [16], image denoising is desired within the general framework too. Finally, in the case of 4D dynamic imaging, the corresponding integrated display step is the computation of an image of the estimated quantized parameter, based on which cancer/tissue characterization is performed. Therefore, parametric image reconstruction towards removing potential outliers from the image that would hinder the accuracy of any statistical analysis on such an image, is often desirable, a task closely related to denoising, image segmentation and boundary finding.

With notable exceptions, the afore-mentioned tasks have been treated as separate problems in medical imaging research, though it is often the case that the solution to one impacts the solution to the other(s). However, over the recent years a great amount of studies have been undertaken that jointly estimate the optimal solution of the different tasks involved. The vast majority of those studies deal with integrating registration and organ segmentation. Combined segmentation and registration has potential applications in a number of areas; essentially wherever both processes have previously been performed sequentially. Examples include the registration of brain atlases towards brain segmentation [241, 10, 242, 236, 223, 161, 157, 49, 240, 190, 61, 62, 151, 4, 6, 82, 177, 179], joint registration of dynamic 4D images and tissues segmentation of images of various organs, such as the breast [237], the heart [129, 127], the kidney [251] and the lung [239], motion estimation and shape identification [187], joint registration (mapping from the atlas to the image space), segmentation (anatomical labelmap), and intensity correction (image inhomogeneities) [162], simultaneous non-rigid registration, segmentation, and tumor detection [122], jointly estimation of motion and the pharmacokinetic parameter in DCE-MRI [20], as well as joint registration and CT image denoising [16].

The most preferable approach to the joint solution among the afore-mentioned studies, is the computation of a maximum a posteriori (MAP) joint estimate of registration and another parameter, i.e. segmentation, quantized parameter etc. Such an estimate of the unknown quantities had been initially used in Bayesian image restoration [64]. That first approach could be described as follows: suppose $X = \{x_{ij}, i = 1, \dots, m; j = 1, \dots, n\}$ represents a true but unobservable 2D image, where x_{ij} measures the color/gray-level/intensity of the pixel of the i^{th} row and j^{th} column. The available data are Y , a version of X distorted by noise (e.g. additive Gaussian noise) and/or some other form of distortion. Then in a Bayesian image restoration method, one would seek to maximize $p(X|Y)$, the probability density for X , given Y [54], where $p(X|Y)$ is proportional to $p(Y|X)p(X)$. The likelihood term, $p(Y|X)$, models the distortion process and the prior, $p(X)$, is chosen to represent prior knowledge, usually about local dependence or spatial correlation within the image. Introduced by Geman and Geman [54], Markov Random Fields (MRF) are most of the times used as priors in the Bayesian formulation, to represent spatial information in the image. Based on the Hammersley-Clifford theorem that implies that any probability measure that satisfies a Markov property is a Gibbs measure for an appropriate choice of (locally defined) energy function, the prior probability $p(X)$ can be expressed as $p(X = x) = \frac{1}{Z(\beta)} \exp(-\beta E(x))$, where x is the state the image X can be (equivalently the random variable X having value x) and β is a parameter which controls the "peakiness" of the distribution and can be interpreted as the inverse of the temperature in statistical mechanics. Moreover, $E(x)$ is an

energy function to be expressed as a weighted sum of clique potentials. MAP formulation (and Bayesian approach in general) had been acknowledged for being well-suited to restoration, particularly for handling general forms of spatial degradation. In the same time though, it was also computationally demanding, the number of possible intensity images is L^M , where L denotes the number of allowable gray-levels and M is the number of pixels or voxels in the image, which ruled out any direct search, even for small images, while some assumptions on the image and degradation model became necessary. Geman and Geman [54] gave an ingenious but computationally demanding solution, through the use of simulated annealing [93] and the Gibbs sampler. Due to that computational burden, annealing methods - despite their theoretical guarantees with respect to the attained solution - had later no practical use.

That initial work of Geman and Geman [54] inspired researchers to apply the Bayesian framework to restore medical images, such as PET images [33, 42, 114], as well as to use it for joint parameter estimation, such as joint non-rigid registration and tissues segmentation [236, 161, 237, 122, 20]. The joint problem is casted as a problem of MAP estimation of the segmentation labels $\mathcal{S} = [S_1, \dots, S_n]$, transformations \mathcal{T} given n datasets I_1, \dots, I_n and the solution is posed using MRFs. The Bayesian problem may be stated for two datasets I_1 and I_2 as:

$$P(\mathcal{S}, \mathcal{T} | I_1, I_2) = \frac{P(I_1, I_2 | \mathcal{S}, \mathcal{T})P(\mathcal{S}, \mathcal{T})}{P(I_1, I_2)} \quad (4.1)$$

If data independence is assumed, then $P(I_1, I_2) = P(I_1)P(I_2)$, which, for consistency, implies $P(\mathcal{S}_1, \mathcal{S}_2, \mathcal{T}) = P(\mathcal{S}_1)P(\mathcal{S}_2)P(\mathcal{T})$. To determine \mathcal{S}_1 , \mathcal{S}_2 and \mathcal{T} is by following MAP estimation problem:

$$(\hat{\mathcal{S}}, \hat{\mathcal{T}}) = \operatorname{argmax}_{\mathcal{S}, \mathcal{T}} \log P(\mathcal{S}, \mathcal{T} | I_1, I_2) \quad (4.2)$$

In general, this results in a system of equations for which there is no analytical solution. The most common way to compute the MAP estimate is by adopting an instance of the expectation maximization (EM) algorithm [?], In that way, the estimation of the parameters is improved by iterating between the Expectation-Step (E-Step) and Maximization-Step (M-Step) [161, 62]. On the other hand, Wyatt and Noble [236] used the Iterated Conditional Modes (ICM) algorithm [17] to get a MAP estimate of their joint registration and segmentation problem, which ensured quick convergence to a local minimum (| 4–8 iterations). Gradient-based methods have also been applied in various joint MAP estimation problems [237, 122, 20].

A discrete formulation of the joint registration and segmentation estimation problem has also been designed by Parisot et al. [151] for segmenting gliomas, as well as by Alchatzidis et al. [4] and more recently by Shakeri et al.

[177, 179] for segmenting sub-cortical structures of the human brain with the use of atlases. Alchatzidis et al. [4] took into account discriminatively learned through Random Forest voxel likelihoods, used as priors for the segmentation labels, while in Shakira et al. work, Fully-Convolutional Neural Network (F-CNN) segmentation priors were incorporated into the Bayesian framework, deriving better in comparison to the Random Forest-based priors. All the afore-mentioned works with a discrete formulation were based on the initial work of Glocker et al. [58] on deformable graph-based image registration. Dual Decomposition (DD) [97] was applied in [4], while FastPD [101] was applied in [151, 177, 179], both offering global optimality guarantees.

Finally, besides the popular MAP estimate, three more estimates have been found in the literature for joint parameter estimation. Gooya et al. [61, 62] defined the solution to the problem of joint segmentation registration and atlas parameter estimation as the maximum of the conditional likelihood of the observed images, while EM was used to iteratively optimize the estimation of the parameters. Then in studies in which segmentation is approached through edge detection, the Ambrosio-Tortorelli approximation of Mumford-Shah model, which is traditionally used for image segmentation, has been modified so that the new functional can also estimate the spatial transformation between images [74, 49]. The goal in this case, is to find the transformations that match the edge sets that can be computed in the images. The functional is minimized by finding a zero crossing of the variation. A geometric variational approach (active contours) was followed by Yezzi et al. [241, 242] too to identify similar curves in images that are related by mapping (registration). Then [10] proposed a strategy for the segmentation of brain from volumetric MR images which integrates 3D segmentation and 3D registration processes. The segmentation process is based on the level set formalism. A variational approach was followed by Bauer et al. [16], which combines the two highly intertwined tasks of denoising a time-of-flight (ToF) image and registration of the ToF surface of the thorax with the corresponding surface extracted from CT data. Last but not least, Iglesias et al. [82] use variational expectation maximization (VEM) and the Demons registration framework in order to efficiently jointly identify the most probable segmentation and registrations of T1-weighted brain scans, guided by a set of proton density (PD) MRI atlases.

4.2 Proposed Method

Let us again consider a sequence of m DW images, each one described by intensity values $s_t(x), t = 1, \dots, m$, with $x \in \Omega_t, \Omega_t \in \mathbf{R}^3$. On top of that, let's consider an extra image $z(x)$ with $x \in \Omega_z$ which represents the ADC template corresponding to the previous image sequence. This ADC template is regarded as the reference frame of an optimal alignment among the DW images.

We therefore seek for two results: a set of deformations $D = \{D : x_R = D_t(x_t), t = \{1, \dots, m\}\}$ which map mutually corresponding points from the m -image spaces to the same point of the reference frame Ω_z and the optimal - in terms of spatial consistency and smoothness - ADC values that can be calculated when all m -images are mutually aligned. The proposed registration algorithm is based on the assumption that, motion's instantiation can be attributed to the acquisition of the first DW image, i.e. the one with the smallest b-value (s_1 image); s_1 is considered as the reference image, to which image space all the rest of the sequence should be mapped and D_1 is regarded zero. This latter assumption is motivated by the fact that the images are acquired sequentially, in a short period of time, from the same patient. Therefore, we wouldn't expect them to differ drastically in terms of the underlying anatomic structure (we expect local, non-linear rather than global, linear transformations to have been occurred). This joint mapping and ADC refinement aims at (i) correcting deformations due to (local) organ deformations or motion, (ii) ensure temporal consistency in the diffusion process and (iii) impose spatial consistency on the deformation fields and the derived ADC map. The appearance model used for the calculation of the ADC, as well as the deformation model, are jointly optimized to define the reference pose. In the following section, the problem formulation is presented, first for the case of negligible deformations and then for all possible deformations.

4.2.1 Appearance (diffusion) model

In DWI, we assume that the intensity values of the images depend mainly on the amount of signal loss occurred during the application of two equally rectangular gradients before and after the 180° -refocusing pulse [15]. The relation between the signal attenuation expressed by the signal intensity s and the diffusion of the water molecules in a microscopic level is known to be exponential [111]. Having acquired the images with high b values ($> 50s/mm^2$), we can assume that the DW images are insensitive to vascular capillary perfusion and diffusion is the only type of motion present, thus the ADC is equal to the water diffusion [95]. Therefore the relation between the ADC (referred to with the letter z) and the signal intensity s can be modeled as:

$$\mathbf{s}_t = \mathbf{s}_1 e^{-(\mathbf{b}_t - \mathbf{b}_1) \cdot \mathbf{z}} \quad (4.3)$$

where \mathbf{s}_t and b_t the image intensity vector and b-value at instant t respectively, \mathbf{s}_1 the signal attenuation for the smallest b value (b_1) and \mathbf{z} is the ADC vector (all vectors are linearized 3D matrices). Denoting with \mathbf{y}_t the natural logarithm of the image vector \mathbf{s}_t , the relation between the image vector and the ADC can be expressed as:

$$\mathbf{y}_t = -\mathbf{b}_t \mathbf{z} + \mathbf{b}_1 \mathbf{z} + \mathbf{y}_1 + \mathbf{n}_t \quad (4.4)$$

where \mathbf{n}_t the noise vector. We are assuming noise to be zero mean i.i.d., thus the multivariate pdf of \mathbf{n}_t is given by:

$$P(\mathbf{n}_t) = \frac{1}{(2\pi)^{\frac{M}{2}} \sigma_n^M} \exp\left\{-\frac{1}{2\sigma_n^2} \mathbf{n}_t^T \mathbf{n}_t\right\} \quad (4.5)$$

where M the size of the linearized noise vector and σ_n^2 denotes the variance of the noise process. If all m DW images are perfectly aligned, the standard way of estimating ADC is by calculating the slope of a line fitted on the plot of the logarithm of the relative signal intensities of the tissue against the b-values:

$$\mathbf{z} = \frac{\sum_{i=1}^m (\mathbf{b}_i - \bar{\mathbf{b}})(\mathbf{y}_i - \bar{\mathbf{y}})}{\sum_{i=1}^m (\mathbf{b}_i - \bar{\mathbf{b}})^2} \quad (4.6)$$

where $\bar{\mathbf{b}}$, $\bar{\mathbf{y}}$ the mean b-value and mean of the natural logarithm of the image vector respectively. We approach the calculation of \mathbf{z} using the Maximum a Posteriori (MAP) technique:

$$\hat{\mathbf{z}} = \underset{\mathbf{z}}{\operatorname{argmax}} \mathbf{P}(\mathbf{z} | \mathbf{y}_1, \dots, \mathbf{y}_m) \quad (4.7)$$

From Bayes' rule, equation 4.7 can be written as:

$$\hat{\mathbf{z}} = \underset{\mathbf{z}}{\operatorname{argmax}} \frac{\mathbf{P}(\mathbf{y}_1, \dots, \mathbf{y}_m | \mathbf{z}) \mathbf{P}(\mathbf{z})}{\mathbf{P}(\mathbf{y}_1, \dots, \mathbf{y}_m)} \quad (4.8)$$

Since the denominator is not a function of \mathbf{z} , it does not influence their estimation and therefore can be ignored. Taking the log probability of posterior probability:

$$\begin{aligned} \hat{\mathbf{z}} = \underset{\mathbf{z}}{\operatorname{argmax}} \{ & [\log \mathbf{P}(\mathbf{y}_1, \dots, \mathbf{y}_m | \mathbf{z}) \\ & + \log \mathbf{P}(\mathbf{z})] \} \end{aligned} \quad (4.9)$$

Next we solve equation 4.9 assuming there is no deformation between the DW images.

From equation 4.9, since \mathbf{n}_t 's are assumed to be independent:

$$\begin{aligned} \hat{\mathbf{z}} = \underset{\mathbf{z}}{\operatorname{argmax}} \{ & [\log \prod_{t=1}^m \mathbf{P}(\mathbf{y}_t | \mathbf{z}) \\ & + \log \mathbf{P}(\mathbf{z})] \} = \underset{\mathbf{z}}{\operatorname{argmax}} \{ [\sum_{i=1}^m \log \mathbf{P}(\mathbf{y}_i | \mathbf{z}) \\ & + \log \mathbf{P}(\mathbf{z})] \} \end{aligned} \quad (4.10)$$

Since noise is assumed to be i.i.d. Gaussian, from equations 4.4 and 4.5 we have:

$$\begin{aligned} \mathbf{P}(\mathbf{y}_1, \dots, \mathbf{y}_m | \mathbf{z}) = & \\ & \left[\sum_{t=2}^m \log \frac{1}{(2\pi\sigma_n^2)^{\frac{M}{2}}} \exp\left\{-\frac{\|\mathbf{y}_t + \mathbf{z}(\mathbf{b}_t - \mathbf{b}_1) - \mathbf{y}_1\|^2}{2\sigma_n^2}\right\} \right] = \\ & \sum_{t=2}^m \frac{-\|\mathbf{y}_t + \mathbf{z}(\mathbf{b}_t - \mathbf{b}_1) - \mathbf{y}_1\|^2}{2\sigma_n^2} - \frac{M}{3} \log(2\pi\sigma_n^2) \end{aligned} \quad (4.11)$$

Substituting equation 4.11 in equation 4.10 we obtain:

$$\begin{aligned} \hat{\mathbf{z}} = & \\ & \underset{\mathbf{z}}{\operatorname{argmax}} \left\{ \left[\sum_{t=2}^m \frac{-\|\mathbf{y}_t + \mathbf{z}(\mathbf{b}_t - \mathbf{b}_1) - \mathbf{y}_1\|^2}{2\sigma_n^2} \right. \right. \\ & \left. \left. + \log \mathbf{P}(\mathbf{z}) \right] \right\} \end{aligned} \quad (4.12)$$

The derivation of a solution for ADC based on equation 4.12 is the first contribution of our work, in which the ADC can be calculated based on the data (DW images) and some prior knowledge about context dependencies on ADC map values, acting as regularization constraints.

4.2.2 Joint appearance and deformation model

Assuming now that some motion has occurred during the acquisition process of the DW images, equation 4.3 takes the form:

$$\mathbf{y}_t \circ \mathbf{D}_t = -\mathbf{b}_t \mathbf{z} + \mathbf{b}_1 \mathbf{z} + \mathbf{y}_1 + \mathbf{n}_t \quad (4.13)$$

where \mathbf{D}_t denotes the deformation field that maps \mathbf{s}_t to the ADC template space. In this case, we would like to compute the $m-1$ deformation fields that would bring the m DW images to a common reference space in which the ADC map can be accurately estimated. Let's denote the geometric deformation that maps the DW image \mathbf{s}_t to the common (ADC) space with $\mathbf{D}_t(\mathbf{x}) = \mathbf{x} + \mathbf{d}_t(\mathbf{x})$, where \mathbf{d}_t is the displacement field of image \mathbf{s}_t . The joint posterior probability for the appearance model parameters and the set of displacement fields $[\mathbf{d}_2, \dots, \mathbf{d}_m]$ is given by:

$$\begin{aligned} \mathbf{P}(\mathbf{d}_2, \dots, \mathbf{d}_m, \mathbf{z} | \mathbf{y}_1, \dots, \mathbf{y}_m) = & \\ \frac{\mathbf{P}(\mathbf{y}_1, \dots, \mathbf{y}_m | \mathbf{d}_2, \dots, \mathbf{d}_m, \mathbf{z}) \mathbf{P}(\mathbf{d}_2, \dots, \mathbf{d}_m, \mathbf{z})}{\mathbf{P}(\mathbf{y}_1, \dots, \mathbf{y}_m)} & \end{aligned} \quad (4.14)$$

The random fields \mathbf{d}_t and \mathbf{z} are once again assumed to be statistically independent, as they refer to three independent processes. Therefore, the joint

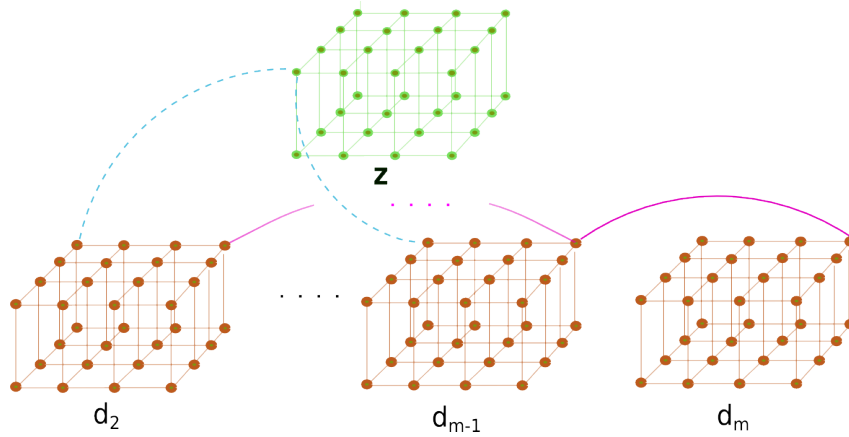


Figure 4.1: The node and the edge system of all the connected graphs.

With green and brown color the relationship within the grid nodes belonging to ADC and each of the deformation field respectively (intra connections). The blue dotted edge represents the dependencies among deformation field and appearance model (coupling relationship), whereas pink edges denote the temporal relationship between successive deformation fields (inter relationship).

MAP solution could be derived similarly as in the previous section, resulting in the following optimization problem:

$$\begin{aligned} \hat{\mathbf{z}}, \hat{\mathbf{d}}_2, \dots, \hat{\mathbf{d}}_m = & \\ \operatorname{argmax}_{\mathbf{z}, \mathbf{d}_2, \dots, \mathbf{d}_m} \{ & \left[\sum_{t=2}^m \frac{-\|\mathbf{y}_t \circ \mathbf{D}_t + \mathbf{z}(\mathbf{b}_t - \mathbf{b}_1) - \mathbf{y}_1\|^2}{2\sigma_n^2} \right. \\ & \left. + \log \mathbf{P}(\mathbf{z}) + \log \mathbf{P}(\mathbf{d}_2, \dots, \mathbf{d}_m) \right] \} \end{aligned} \quad (4.15)$$

The latter equation for computing a joint solution for ADC and deformation fields, using some priors on context dependencies on \mathbf{z} and deformation fields, is the second contribution of our work.

4.2.3 Objective Functions: MRF-based Energy Formulations

We formulate our joint DWI registration and ADC modeling problem using MRF. We opt for constructing simultaneously with registering the images the ADC map, while image s_1 is considered as the reference one. For the rest of the thesis, we will refer to the proposed method as *JointRef1*.

Energy Formulation of JointRef1:

The joint model now is parameterized by a set of m isomorphic grid graphs $G = \{G_2, \dots, G_{m+1}\}$, the first $m - 1$ being superimposed onto the corresponding DW image, whereas the last grid graph is superimposed onto the ADC map (z_c image) that we want to compute. The label set for the displacements is a

quantized version of the 3D displacement space, whereas the label set for the ADC map are quantized versions of the ADC intensities.

For every control point in each grid i there is a node p that represents either its displacement if the grid is a deformation grid or the ADC value in case of the last grid ($p \in \mathcal{V}$, with \mathcal{V} denoting the set of all nodes on a grid that encode the latent variable). The nodes in the graph are connected with a set of edges \mathcal{E} that encode the interactions between the deformation and the ADC variables. In the end, the displacement of a voxel x of the image will be determined by the control point's displacements and the influence of each control point on x , which is given by cubic B-splines. The diffusion value on a voxel of the z_c image will be determined in a similar way.

Energy Terms: The constructed graph is associated with an energy, consisting of four pairwise terms:

$$\begin{aligned}
E_{joint}(d_2, \dots, d_m, z_c) = & \\
& \lambda_{inter} \sum_{t=2}^{m-1} \sum_{p \in G_t} V_{inter}(l_p^{d_t}, l_p^{d_{t+1}}) \\
& + \lambda_{intra^1} \sum_{t=2}^m \sum_{p \in G_t} \sum_{q \in (N(p) \cap G_t)} V_{intra^1}(l_p^{d_t}, l_q^{d_t}) \\
& + \lambda_{intra^2} \sum_{p \in G_{m+1}} \sum_{q \in (N(p) \cap G_{m+1})} V_{intra^2}(l_p^{z_c}, l_q^{z_c}) \\
& + \lambda_c \sum_{t=2}^m \sum_{p \in G_t} \sum_{p \in G_{m+1}} V_c(l_p^{d_t}, l_p^{z_c})
\end{aligned} \tag{4.16}$$

where V_{inter} is a potential for temporal regularization (inter-deformation dependency), $V_{intra^n}(\cdot, \cdot)$, $n = 1, \dots, 2$ are the potentials imposing spatial constraints on the deformation fields and the ADC map respectively, whereas V_c is the coupling potential. The constants λ_{inter} , λ_{intra^n} , $n = 1, \dots, 2$ and λ_c are used to weight the different types of potentials.

Coupling term of JointRef1: The coupling term (data term) that penalizes deformations that lead to an increase in the matching error among \mathbf{z}_c and the signal attenuation at a given instant t , based on equation 4.3. Thus the coupling term in our proposed method is computed as follows:

$$\begin{aligned}
V_c(l_p^{d_t}, l_p^{z_c}) = & \int_{\Omega_{s_t}} \bar{\eta}(\|x - p\|) \\
& \left(s_t(x + d^{l_p^{d_t}}) - s_1(x) e^{(b_t - b_1) z_c^{l_p^{z_c}}} \right)^2 dx
\end{aligned} \tag{4.17}$$

It is defined on the image domain Ω and a function $\bar{\eta}$ is used to back project the voxel-wise information on the grids' control points, by determining how

much voxel x influences the control point p .

Spatial and temporal deformation smoothness: We assume that the organs' motion evolves smoothly during image acquisition process therefore we expect the deformation on each DW image to not deviate much from the deformation computed on each immediate neighbor, meaning the image preceding it. In the same time, each deformation field should deform the tissues in a way in which the anatomical information is retained. Therefore in order to impose temporal and spatial smoothness on the deformation fields we penalize the magnitude of displacement vector differences. The pairwise potential would then be:

$$V(l_p^{d_i}, l_q^{d_j}) = \frac{\|\mathbf{d}_p^{d_i} - \mathbf{d}_q^{d_j}\|}{\|p - q\|} \quad (4.18)$$

In case of temporal deformation smoothness (V_{inter}) $p \equiv q$ and $j = i + 1$, whereas in case of spatial deformation smoothness (V_{intra1}) $i \equiv j$. For both cases we are assuming a 8-nodes connectivity.

Spatial smoothness on ADC map: The term in both energy formulations related to the spatial constraints applied within the ADC map of our appearance model (\mathbf{z}) is the squared error between two different appearance labels was used towards this end:

$$V_{intra2}(l_p^z, l_q^z) = (\mathbf{z}_p^z - \mathbf{z}_q^z)^2, \quad (4.19)$$

Again we are assuming a 8-nodes intra-image connectivity.

Implementation Details: Our algorithm follows a coarse-to-fine process that first estimates parameters at a coarse spatial image resolution level and then updates the solution to a finer resolution level. We applied a multi-resolution scheme with 3 resolutions levels; two levels in which the joint problem is solved and one at full image resolution in which only the appearance model is optimized, keeping the previously obtained deformation fields fixed. A fast optimization scheme relying on linear programming and duality [101] is used at each step. Finally, regarding the run-time performance of the method, all the experiments were computed on a 8-cores machine (3.6 GHz processing power) with a memory requirement of 4 GB. It took approximately 26 minutes to co-register the images of a sequence of size of three, using five sub-iterations in each pyramidal level for refining the label space. The number of sub-iterations to be used is a factor that heavily affects the computational time of our method.

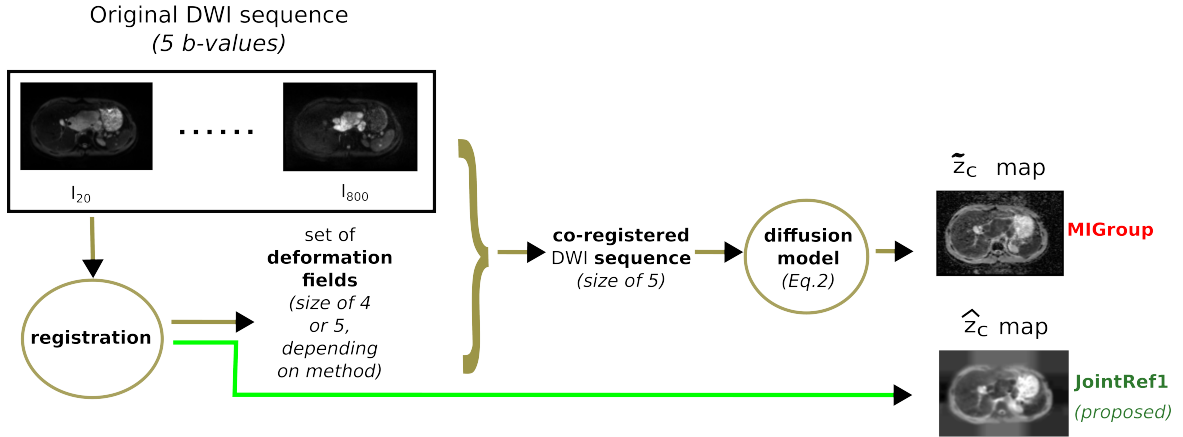


Figure 4.2: The image processing pipeline.

Circles demonstrate each of the computations performed towards computing an ADC map with motion correction. In NoReg case, apparently no registration occurred, therefore the original rather than a deformed version of the DWI sequences was input to the diffusion model to compute the \tilde{z}_c or \hat{z}_v map.

Differentiating features	NoReg	MIGroup [189]	MIRef1 [189]	PhyGroup [104]	PhyRef1 [104]	JointRef1
Deformable registration?	-	yes	yes	yes	yes	yes
Groupwise registration?	-	yes	yes	yes	yes	no
Reference space	-	intermediate	s_1	intermediate	s_1	s_1
Data term	-	MI	MI	Fit.Error on Diff.Model	Fit.Error on Diff.Model	SSE of Eq.4.3
Temporal smoothness?	-	no	no	no	no	yes
Spatial constraints	-	on D	on D	on D	on D	on D and z
Output	-	D	D	D	D	\hat{D} and \hat{z}_c

Table 4.1: Comparative information on the examined registration methods. Since NoReg is not a method rather than a "scenario", only its additional features (ADC maps computed without registration) are mentioned.

4.2.4 Comparison with Other Methods

Besides our proposed method (denoted in the rest of the paper as "JointRef1"), other four fully automated registration methods are examined, which differ on various features MRF-based image registration methods hold (see Table 4.1). The four registration methods examined for comparison in the current study are the following: the original deformable group-wise registration using a physiological model proposed in [104] ("PhyGroup"), a slightly modified version of the latter one in which, similarly to "JointRef1", image s_1 is considered as the reference image ("PhyRef1") and therefore is not deformed, another groupwise registration approach that uses MI for the inter-image matching criterion, inspired by the work of Sotiras et al.[189] ("MIGroup") and the a group-wise registration as the latter one, only again s_1

is preselected as the reference one ("MIRef1"). In the same time, we would refer to the case where no image registration took place as the "NoReg" scenario.

Moreover, based on the registration method, the computation of parametric maps varies too (see "Additional features" row in Table 4.1). In case of NoReg, equation 3.2 is used to compute both a \hat{z}_c and \hat{z}_v map, whereas for the case of a registration method, once all DW images are co-registered, a voxel-wise calculation of a z_c or z_v map (always depending on the b-values set used), would be based on warped DW images:

$$\tilde{z} = \frac{\sum_{t=1}^m (\mathbf{b}_t - \bar{\mathbf{b}}) ((\mathbf{g}_t \circ \mathbf{D}_t) - \bar{\mathbf{g}})}{\sum_{t=1}^m (\mathbf{b}_t - \bar{\mathbf{b}})^2} \quad (4.20)$$

where \tilde{z} the ADC computed through linear regression and based on image registration, $\mathbf{g}_t = \ln \mathbf{s}_t$, \bar{b} the mean b-value and $\bar{\mathbf{g}}$ the mean of $\ln(\mathbf{s}_t \circ \mathbf{D}_t)$. In case of our proposed method JointRef1, as described before, an "extracellular diffusion" map \hat{z}_c is derived explicitly by our joint optimization scheme, whereas an "extravascular diffusion" map is computed through the above equation. Finally, note that for PhyRef1, MIRef1 and JointRef1, D_1 would have only zero values in the above equation. In Figure 4.2 one can see the steps towards computing the parametric maps from the DWI sequence.

4.2.5 Calculation of Optimal Weights of Potentials

The optimal values for the weights on the potentials of the energy formulation in each registration method examined were computed based on the simulated data, described in the next section. Using the simulated deformation fields and ADC map, we computed the potentials of each term in the MRF energy formulation of each method. Let's denote the matrix of the potentials by V . Then we found the optimal weights on these potentials by solving the linear least-squares: $c_{opt} = \min_c \frac{1}{2} \|V \cdot c\|^2$, subject to $\sum_{n=1}^N \lambda_n = 1$, $\lambda_n > 0$, where $c = [\lambda_1 \dots \lambda_N]$ the vector of the weights. In that way, we avoid learning the weights through brute force by running the same experiment many times, which would be a time costly approach.

However, FastPD can be applied only to pair-wise energies and therefore it cannot be used for the case of $E_{MRF_{HOPhyRef1}}$, which includes high-order cliques in its energy formulation. Inference in Markov Random Fields (MRFs) with higher order cliques is possible and a lot of research efforts have been devoted recently to investigate it (see for example [83, 167, 96]). However, the gain of the faithful modeling comes at the expense of significantly increased computational burden. Our discrete high-order MRF-based energy minimization problem was solved using Dual Decomposition (DD).

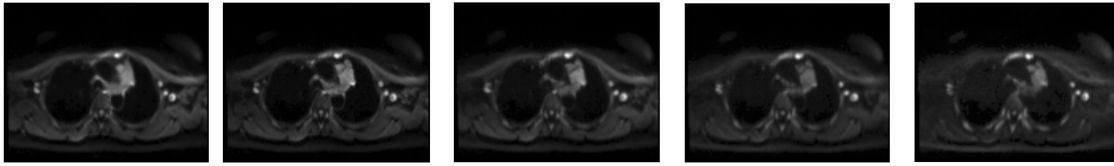


Figure 4.3: Real data.

An axial slice of the 3D image of a patient, with b values of 20, 50, 150, 400 and 800 s/mm^2 (from left to right).

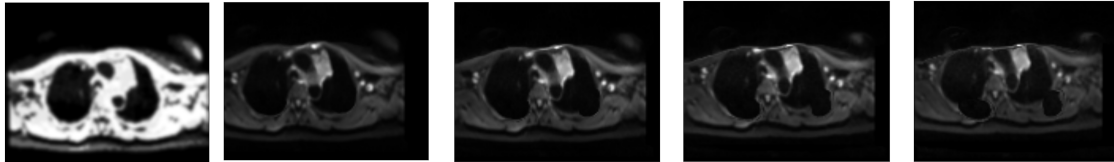


Figure 4.4: Simulated data

An axial slice of the simulated 3D images of the same patient as in the above figure. The very left image is the corresponding slice from the simulated ADC map, whereas next to it from left to right are the slices of the simulated images of b values of 50, 150, 400 and 800 s/mm^2 ("b 20" image was used to simulate the diffusion process).

In our framework, the graph is decomposed into subgraphs that constitute the set of subproblems, such that they cover (at least once) every node and edge in each graph. One slave problem is defined for each line parallel to a coordinate axis in space and time (corresponding to pairwise interactions), and one slave is defined for the higher order clique (related to the data term). Two different optimization schemes are used for the solution of the subproblems: the FastPD optimizer [101], described in Chapter 2, guarantees for an almost optimal solution to such an NP-hard MRF problem, for pairwise interactions and exhaustive search for the higher order clique. In the end, global optimization is achieved through DD, that ensures agreement among the solutions provided by all slaves.

4.3 Experimental Validation

In order to validate the proposed registration method, we used a data set provided by the Centre Hospitalier Universitaire Henri-Mondor, France. The data set consisted of 3D images of thirty-eight (38) different patients with lymphoma, scanned with a 3 Tesla MRI scanner using 5 b values: 20, 50, 150, 400 and 800 (s/mm^2). Therefore, the sequence of the images to be registered was always of size 5 ($m = 5$) per patient. Both male and female patients were included. The image size was $130 \times 106 \times 22$ for every patient, with a pixel resolution of $2.46 \times 2.46 \text{ mm}^2$ in the axial plane and 5 mm^2 in the z-axis. Each image had been manually annotated by experts to indicate the contour of the tumor (see figure 4.3).

As part of the evaluation of the registration methods, simulated data (deformation fields and a z_c map) were created. As a first step, a simulated z_c

map of every patient was generated, based on his/her original s_1 image and the k-means unsupervised image classification algorithm, applied on s_1 in order to segment the image into different regions corresponding most likely to different tissues. A fixed size of 10 segments was used for every patient. The reason s_1 image was chosen for this step, was due to the fact that it has the highest SNR among all the DW images in the original DWI sequence (real data), a fact that facilitates the segmentation process. By assigning different sampled ADC values to the different segments, the final segmented, simulated z_c map was created. Using the same b-values found in the real DWI sequences, we computed simulated DW images of different b-values, based on equation 4.3 (we assume that the mono-exponential diffusion model holds true as the highest b-value of the set is less than $2000s/mm^2$), resulting in simulated DWI sequences. Finally, deformation fields, composed by displacement vectors of various norms, were applied on their simulated images towards deforming each of them except image s_1 . Different combinations of a rigid transformation and a deformation (varying in extend) were applied on each simulated DW image (see an example of a simulated z_c and a simulated DWI sequence figure 4.4).

4.3.1 Evaluation on the Simulated Data

The goal of this experiment is to find out which of the examined registration methods better estimates the simulated deformation fields and z_c image. The Euclidean distance (ED) was used as a distance criterion for the deformation fields, with the mean distance over the entire image region being $ED_t = \frac{1}{|\Omega|} \sum_{x \in |\Omega|} \|D_t(x) - \hat{D}_t(x)\|_2$, and averaged over the deformation fields error being $ED = \frac{1}{m-1} \sum_{t=2}^m ED_t$. On the other hand, the sum of squared errors of prediction (SSE) was used as a measure to define the discrepancy between the simulated z_c image and the one computed or derived through each of the examined registration methods, $SSE = \frac{1}{|\Omega|} \sum_{x \in |\Omega|} (z_c(x) - \hat{z}_c(x))^2$. \hat{D} and \hat{z}_c are general notations of the estimated by each method deformation field and ADC map respectively (for example \hat{z}_c becomes \hat{z}_c in case of JointRef1). Figure 4.5 shows box-plots results on the ED and SSE across the DWI sequences of the population. Note that simulated deformation fields were compared with the inverse deformation fields derived by the examined registration. The results in figure 4.5 were derived by registering sequences of size three (three b-values used). There is a common pattern in both plots of figure 4.5, where JointRef1 method gives the smallest reconstruction error in recovering both the deformation fields and the z_c image. Then in figure 4.6, we plot the same results as in figure 4.5 this time averaged over the entire population and plotted over the number of b-values (size of DWI sequence). There is no consistent pattern on the relationship between the number of b-values and

the reconstruction error.

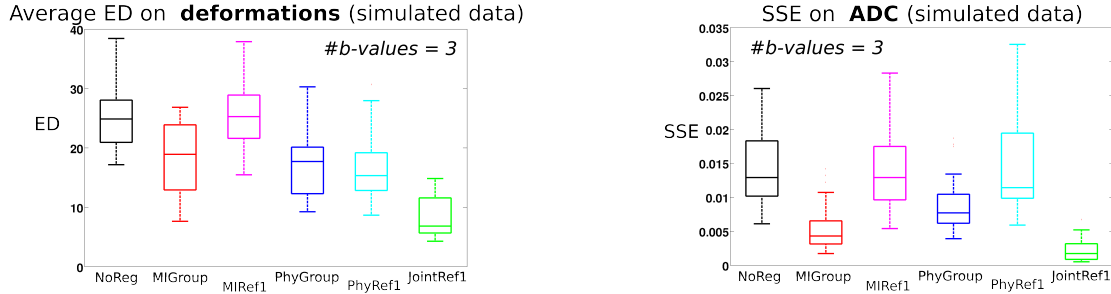


Figure 4.5: The SSE with simulated data on retrieved deformation fields and ADC map.

Box plots across population of the average euclidean distance over the DWI sequence size between simulated deformation fields and the inverse deformation fields derived by the examined method (left image) and the SSE between the simulated \mathbf{z}_c image and the corresponding one calculated based on registered by the different methods (right image). $\hat{\mathbf{z}}_c$ and $\hat{\mathbf{z}}_c$ are the maps compared against the simulated \mathbf{z}_c image for the case of JointRef1 and all the rest registration methods respectively. The specific results were acquired using 3 b-values.

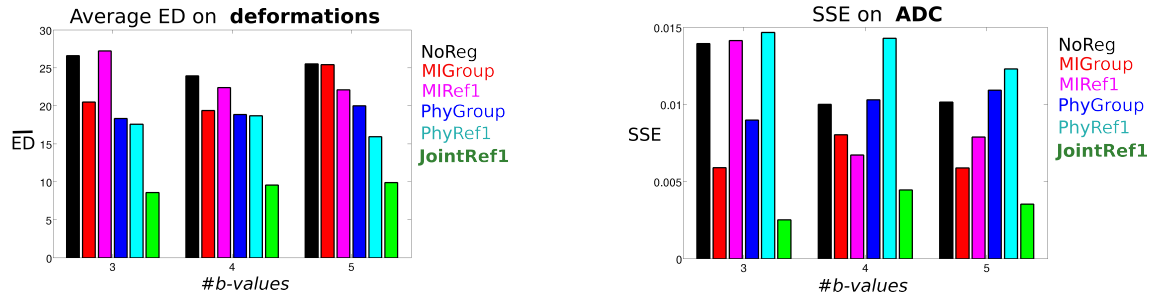


Figure 4.6: Error bars with simulated data on retrieved deformation fields and ADC map over number of b-values.

Same results as in figure 4.5, this time averaged over the entire population and plotted over the size of the DWI sequence (number of b-values).

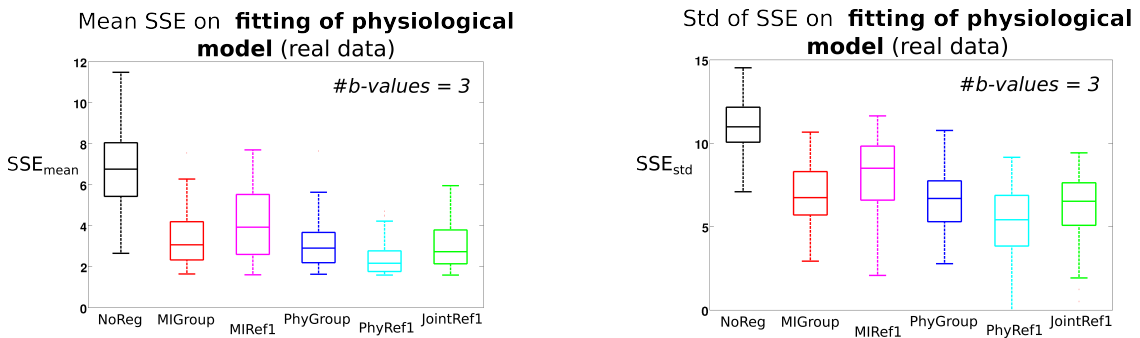


Figure 4.7: The fitting error on the physiological model with real data.

Box plots of the (voxelwise computed) mean sum-squared fitting error (left) and each standard deviation (right) across population. The specific results were acquired using 3 b-values in each case.

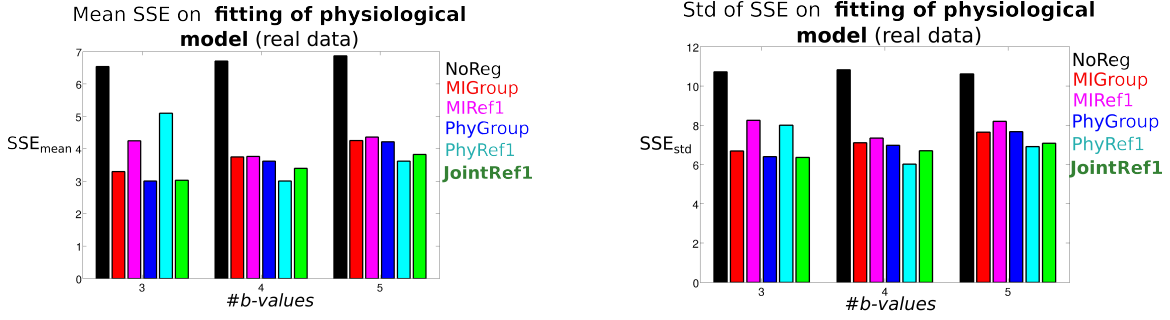


Figure 4.8: Error bars over b-values with real data (fitting error on the physiological model)
Plots of the corresponding results in figure 4.7 over the size of the DWI sequence (number of b-values), in which the plot is coloured differently based on the post-processing scenario.

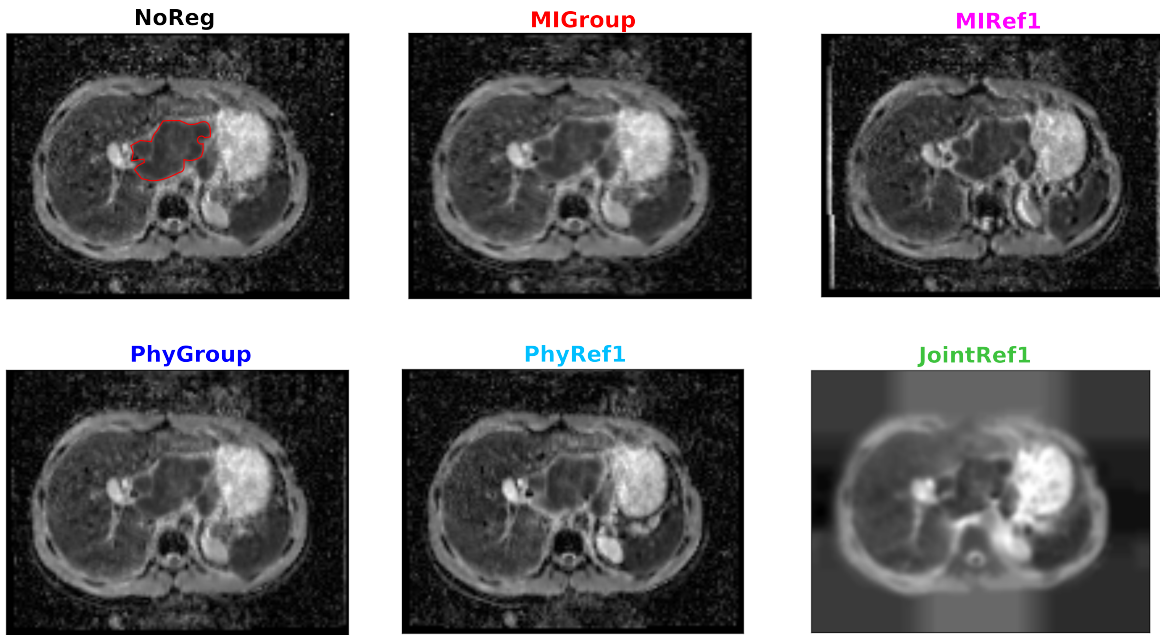


Figure 4.9: Computed ADC maps by applying each of the examined methods.
Same axial slice of the \hat{z}_c ADC map derived by equation 4.4 in case of NoReg and equation 4.20 for all the examined registration methods, except the proposed one, JointRef1 (bottom-right), which was computed explicitly by the joint formulation (\hat{z}_c). The red contour on the first image (up-left) denotes the tumor of the patient, delineated by an expert.

Evaluation on the Real Data

The performance of the five registration approaches was also quantitatively assessed by examining fitting to the diffusion model error, based on the real data. The SSE between the fitted, by the diffusion model (see equation 4.3) and the real data was as the validation criterion. The mean SSE is computed as: $SSE_{mean} = \frac{1}{|\Omega|} \sum_{x \in |\Omega|} (\hat{\mathbf{s}}_t(\mathbf{x}) - \mathbf{s}_t(\mathbf{x}))^2$, in case of NoReg and $SSE_{mean} = \frac{1}{|\Omega|} \sum_{x \in |\Omega|} (\hat{\mathbf{s}}_t(\mathbf{x}) - \mathbf{s}_t(\mathbf{x}) \circ \mathbf{D}_t(\mathbf{x}))^2$ in case of the registration methods, where $\hat{\mathbf{s}}_t(\mathbf{x})$ the fitted value. The standard deviation of SSE is computed as: $SSE_{std} = \frac{1}{|\Omega|} \sum_{x \in |\Omega|} ((\hat{\mathbf{s}}_t(\mathbf{x}) - \mathbf{s}_t(\mathbf{x})) - SSE_{mean})^2$, in case of NoReg and

$SSE_{mean} = \frac{1}{|\Omega|} \sum_{x \in |\Omega|} ((\hat{\mathbf{s}}_t(\mathbf{x}) - \mathbf{s}_t(\mathbf{x}) \circ \mathbf{D}_t(\mathbf{x})) - SSE_{mean})^2$ in case of the registration methods. $\hat{\mathbf{z}}_c$, $\hat{\mathbf{z}}_c$ and $\tilde{\mathbf{z}}_c$ were the ADC maps used in case of NoReg, JointRef1 and the rest of the examined registration methods respectively. The left plot of figure 4.7 is the boxplot of the mean SSE across population and in the right plot of the same figure, a boxplot of the standard deviation of SSE is plotted. Then in figure 4.8 we plot the corresponding results but this time averaged over the population and plotted over the number of b-values used. We notice that JointRef1 has almost equally good performance as PhyGroup and PhyRef1, which actually use the fitting to the diffusion model criterion in their formulation. Regarding the effect of the number of b-values on the fitting to the diffusion model error, again there is no clear pattern, however in most cases it slightly increases as we move to bigger number of b-values. An axial view of the \mathbf{z}_c map derived by each registration method and NoReg can be seen in figure 4.9.

4.4 Discussion

We proposed a novel joint deformable registration based on diffusion modeling that derives an optimal geometrical as well as appearance representation towards more accurately depicting the physiological process taking place during DW image acquisition. Two experiments were designed to evaluate the registration performance, based on simulated and real data respectively. In terms of a reconstruction error experiment using simulated data, JointRef1 outperformed all the rest in recovering more accurately both the simulated deformation fields applied to the simulated DWI sequences, as well as the simulated ADC based on which the simulated sequence was created. Moreover, JointRef1 showed the equally good to PhyGroup and PhyRef1 results on the fitting error to the diffusion model using the real dataset. PhyGroup and PhyRef1 use the fitting to the diffusion model criterion in their energy formulation. Regarding whether a preselection of a reference space is a better approach, we noticed that the methods registering the images into an intermediate reference space gave better results, as MIGroup performed better than MIREf1 in all experiments, and PhyGroup yielded better results than PhyRef1, except on the fitting error.

Chapter 5

Extraction of DW-MR Imaging Biomarkers through the Proposed Registration Methods

DWI is a non-invasive functional imaging technique that explores the extra-, intra-, transcellular and intracapillary motion of water molecules in the body, as a result of their internal thermal energy [155]. The sensitivity of the DWI sequence to water diffusion depends on a parameter called b-value, which is proportional most of the times to the amplitude of the applied diffusion-sensitizing (bipolar) gradients or the duration and the time intervals between the gradients. By scanning the patient with different b-values, quantitative parameters can be computed and displayed as parametric maps (one value per voxel). The main argument towards their use lies on the fact that any quantitative parameter is independent of the magnetic field's strength. Thus by analysing such an image instead of individual DW images, the risk of false-positive caused by the T2 shine-through effect (hyperintensity on high b-values caused by high proton density and not increased cellularity) is decreased. The ADC parameter, which reflects the gradient of water diffusivity in the body, has been broadly acknowledged as an imaging biomarker towards lesion detection and characterization, by assessing its type and stage, as well as prediction of treatment's response [108], [75], [8]. The word "apparent" is added because other factors than random diffusion may influence the mobility of water, such as vascular capillary perfusion, a potential imaging biomarker that hasn't been thoroughly investigated in previous works.

Most of the studies that try to estimate the role of DWI in oncology, don't take into account any misalignment among the images used to compute the ADC map. These misalignments could be caused by movement of the subject during image acquisition or physiological organ or muscles deformation due to respiration and peristalsis. All these factors could result in misregistration of the images acquired with different b-values and adversely

affect the quality of ADC [108]. Motion correction in DWI has been recently studied by some researchers, examining various image registration schemes, as reported in the next section. Nevertheless, to the best of our knowledge, there hasn't been any published work in DWI, on evaluating whether image registration improves the quality of ADC as an imaging biomarker.

In this chapter, we examine the effect of image registration on the potential of diffusion-based parameters to characterize lymphomas based on their types and level of malignancy (disease's stage), as well as assess or predict tumor's resistance to therapy (treatment response).

5.1 Prior Work

The value of whole-body DW-MRI in comparison to other whole-body imaging modalities used for detection characterization of various tumors in the body, as well as for patient management has been the objective of many studies over the last decade [108, 75, 8]. What most of the studies trying to quantitatively assess the role of whole-body DW-MRI in oncology have in common, it's the fact that they don't take into account any misalignment among the images used to compute the ADC map. These misalignments could be caused by the physiological water motion and bulk tissue movements such as respiration and peristalsis. Spatial alignment of the acquired DW-MRIs, could also be lost due to subject's movement(s) during image acquisition. All these factors could result in misregistration of the images acquired with different b -values and adversely affect the quality of ADC, a parameter susceptible to such artifacts [155, 108]. In most studies on DWI, the issues of image quality is addressed by averaging a set of DW images acquired several times [95, 84]. This approach though only improves the SNR of DWI and doesn't correct for motion, while it results in longer acquisition time. Moreover, the solution of a breathholding image acquisition protocol requires short scan time and might deteriorate image quality just by causing irregularity in respiratory pace [90, 204], whereas motion-compensation techniques, such as triggering or gating don't perform well in case of irregular or heavy breathing [34]. Retention of the spatial information underlined on the ADC map requires registration of DW image.

Mazaheri et al. [134] applied a rigid type of registration on a multi- b -value DWI sequence and reported a decrease, through motion correction, on the normalized root-mean-square error (NRMSE) of the proposed by Le Bihan et al. [111], diffusion model. However, non-rigid alignment of the DWI sequence becomes necessary in order to cope with the non-linear nature of motion caused by cardiac pulses or respiration [188]. To this end, Guyader et al.[67] examined the influence of groupwise deformable registration on the uncertainty and reproducibility of the ADC map. A fully automated registration scheme was proposed, consisting of an initial groupwise registration

step among odd and even subvolumes acquired by the same b-value, in order to compensate for observed artifacts between the odd and even slices of their acquired images. As a second step, pairwise registration between volumes of different b-value was performed, resulting in a global alignment into a common image space. In the same time, Veeraraghavan et al. [211] suggested a semi-automated framework in which a user should first identify structures of interest in a reference image (that choice varied). These structures are then volumetrically segmented by a segmentation algorithm and used to guide an affine registration algorithm, which aligns the images in a groupwise manner. In both these studies the "image registration" scenario was assessed as the best among all in improving ADC map's computation, using different evaluation criteria. In fact, in [67], the effects of interpolation and Gaussian blurring, as alternative strategies to reduce motion artifacts, were considered, which were proven to be inferior to the registration approach. The similarity criterion applied in both studies for matching images of different b-value was Mutual Information (MI).

5.2 ADC Calculation based on a Physiological Model

Let us consider a sequence of m DW images acquired by m different b-values, each one described by intensity values $s_t(\mathbf{x})$, $t = 1, \dots, m$, with $x \in \Omega_t$, $\Omega_t \in \mathbf{R}^3$. The intensity values of any DW image are assumed to depend mainly on the amount of signal loss due to microscopic translational motions occurring during the application of the Stejskal–Tanner sequence [15]. This microscopic translational motion, known as intravoxel incoherent motion (IVIM), is quantified by the ADC parameter, which integrates both the effect of molecular water diffusion in biological tissues and perfusion (microcirculation of blood in the capillary network) [111]. Let's also consider an extra image $z(\mathbf{x})$ with $x \in \Omega_z$ which represents the ADC template extracted from the afore-mentioned image sequence, assuming that the images are aligned; the ADC template is regarded as the reference frame of an optimal alignment among the DW images.

Depending on the nature of the desired ADC map, a proper configuration of b-values should be designed. In most studies b-values $> 100s/mm^2$ are applied, due to the fact that above that threshold the effect of vascular capillary perfusion is negligible and a "true or extravascular diffusion" map can be attained. On the the hand, it is assumed that an ADC derived by using small b-values, will not only depict a macroscopic water diffusion but will have a component of "true extracellular diffusion". For the rest of the article, we will use the underscore v and c to refer to these two different types of ADC (z_v and z_c).

The ADC can be calculated using at least two DW images. For a pair

of b-values, each less than $2000s/mm^2$, the relationship between the signal attenuation expressed by the signal intensity s and ADC image z is usually modeled by a mono-exponential function:

$$s_2 = s_1 e^{-(b_2 - b_1) \cdot \hat{z}} \quad (5.1)$$

where s_1 and b_1 the image intensity vector and b-value at an instant $t = 1$, s_2 and b_2 the image intensity vector and b-value at a later instant $t = 2$. Depending on the set of b-values used, \hat{z} would represent either \hat{z}_v (diffusion of extravascular nature) or \hat{z}_c (diffusion of extracellular nature). The reason why the highest of the two b-values should be less than $2000s/mm^2$ is due to the fact that above that limit, the mono-exponential relationship doesn't hold true anymore. There is evidence that the relationship would then be better described by a multi-exponential model [148], though b-values of such high range are beyond practical SNR limits.

The estimation of the ADC is expected to be more accurate in case of using more than just images. Its estimation could be then approached through regression analysis on the DWI sequence. The most common method to carry out regression analysis in DWI is linear regression, in which the ADC is computed as the slope of a line fitted on the logarithm of the relative signal intensities of the tissue against the b-values [104]. In that case the ADC would be:

$$\hat{z} = \frac{\sum_{t=1}^m (b_t - \bar{b})(g_t - \bar{g})}{\sum_{t=1}^m (b_t - \bar{b})^2} \quad (5.2)$$

where \hat{z} the ADC computed through linear regression, $g_t = \ln(s_t)$, \bar{b} the mean b-value and \bar{g} the mean of $\ln(s_t)$. Again depending on the range of b-values used, an ADC map of a different nature can be computed (\hat{z}_v or \hat{z}_c).

5.2.1 Histopathological Classification of Lymphomas and Tumor Staging with Deauville Scores

The classification of lymphomas into Hodgkin (HD) or non-Hodgkin (NH) is based on histopathological, immunophenotypical, molecular/cytogenetic and clinical features extracted through a series of related exams. An overview of the current WHO classification of lymphomas and how we arrived at it can be found in [199].

On the other hand, the stratification of lymphomas into different disease stage, is based in this study on Deauville scores: evaluation scores based on visual interpretation of FDG-uptake in a PET scan. Two reference points of the individual patient are considered, which have demonstrated relatively constant uptake on serial imaging. The two reference organs are the mediastinum (aka blood pool) and the liver. The scale ranges from 1 to 5, where 1 is best and 5 is the worst. Each FDG-avid (or previously FDG-avid)

lesion is rated independently. In our case, the Deauville scores were given to each patient once he/she had completed two cycles of chemotherapy (approximately a year after of the onset of the treatment).

5.2.2 Feature extraction for Lymphoma Characterization

Tumors are known to be heterogeneous, therefore our goal is to compute features extracted by the diffusion- or perfusion-based maps, that could aid us in characterizing the lesions based on intra and inter-tumour heterogeneity [88]. To this end, statistical features over the entire tumour regions of interest (ROIs), were computed based on a histogram analysis on these regions. Therefore, besides the mean, standard deviation and mode of tumors' ROI, first-order histogram parameters (kurtosis, skewness, 75th and 95th percentiles of the tumor's intensity distribution) were extracted.

5.2.3 Classification of Type of Lymphoma

One of our goals in this work was to examine whether the proposed method could improve the potential of DWI in automatically classifying lesions into HD or NH lymphomas, based on the statistical features described in the previous paragraph. A classifier based on Linear Discriminant Analysis (LDA) was designed that would assign labels (HD, NH) to each of the testing feature vectors, classifying them to one of the two classes. The feature vectors were the input to the LDA algorithm. The measure of closeness is the log of the probability density function of the testing vectors, multiplied by the class' prior probabilities. In the same time, the probability density function of the testing vector is based on the number of the neighboring to it vectors in each class. The classification through LDA is based on maximizing the ratio of between-class variance to the within-class variance in the training data set.

Similarly to [103], we trained the classifier by dividing the feature vectors into training and testing sets, using an 75% (training): 25% (test) ratio. This division is repeated M times in order to provide a better estimation of the performance of the classifier. In order to estimate if the differences on the classification results between the compared methods were significant, we chose a large value for M (10^4). The metrics used to evaluate the performance of the classifier were the recall, the precision and the overall accuracy.

5.2.4 Subjects - Real Sequences

Thirty-eight patients, (21 males, 17 females; median age: 45 years, range 19–77) with histologically confirmed lymphomas (12 Diffuse Large B-cells, 8 Follicular, 17 Classical Hodgkin and one Non-Hodgkin that couldn't be classified neither as Diffuse Large B-cells nor as Follicular) were prospectively

recruited between September 2012 and December 2015.

Inclusion criteria were absence of contraindications to MRI (such as claustrophobia and implanted pacemakers or neurostimulators), histologically confirmed newly diagnosed FDG-avid lymphoma, age over 14 and performance status with values from 0 to 2 according to ECOG scale. The study was approved by the Ethics Committee of our hospital and all patients, or their parents if minors, signed written consent forms.

All patients underwent both WB-MRI and [^{18}F]-PET within a maximum of one week difference. A whole-body "respiratory-gated" diffusion MR 1.5 Tesla (T) (Avanto; Siemens Healthcare, Erlangen, Germany) protocol using exclusively a single-shot spin-echo echo-planar, introduced in [118], was applied in order to minimize slice-position mismatch between different b-values and different excitations. Moreover, the applied fat suppression approach of STIR gives more homogeneous fat saturation because of its insensitivity to magnetic field heterogeneity [107]. The entire total body MR imaging with 5 sequences was performed within 7 to 8 stations. However, in order to improve the SNR of the calculated ADC map, measurements in the three orthogonal gradient directions are obtained and the signals are averaged (producing the corresponding b-value trace images).

The data set consisted of 3D images derived by scanning each patient with 5 b-values: 20,50,150,400 and 800 (s/mm^2). Three different combinations of image sequences were examined in each experiment, changing each time the number of b-values in order to assess on the efficient number to be used in clinical settings. Whenever sequences of size three are examined the b-values of 50,400 and 800 (s/mm^2) are used, whereas when the size of sequence is four b-values of 50,150,400 and 800 (s/mm^2) are used. For a sequence of size 5 apparently all the b-values are used. The above configurations hold for every patient. The image size was 130x106x22 for every patient, with a pixel resolution of 2.46x2.46 mm^2 in the axial plane and 5 mm^2 in the z-axis. Each image had been manually annotated by experts (A.R.) to indicate the contour of the tumor (see figure 4.3).

5.3 Results

Automatic Classification of Lymphoma Type

We further examined the potential of automatically classifying by the imaging statistical features the patients into the basic types of lymphoma. The performance of the proposed method JointRef1 was compared against all other examined registration methods and NoReg. In each case, the statistical features were extracted from both z_c and z_v parametric maps (in case of JointRef1 \hat{z}_c map was used as the "extracellular diffusion" map). The best combination of features for all the methods turned out to be a combination

Method	Feature from ADC component	Hodgkin		Non-Hodgkin		overall accuracy
		recall	precision	recall	precision	
NoReg	\hat{z}_c, \hat{z}_v	71.44	65.85	60.14	70.37	65.79
MIGroup	\tilde{z}_c, \tilde{z}_v	65.38	60.38	54.89	62.71	60.14
MIRef1	\tilde{z}_c, \tilde{z}_v	71.95	67.04	61.14	70.34	66.54
PhyGroup	\tilde{z}_c, \tilde{z}_v	73.75	65.74	58.99	72.28	66.37
PhyRef1	\tilde{z}_c, \tilde{z}_v	68.43	68.70	65.96	70.08	67.20
JointRef1	\hat{z}_c, \hat{z}_v	84.26	70.72	62.39	83.09	73.32

Table 5.1: Classification results on patients with HD and NH type of lymphoma, derived by the examined methods using 3 b-values. All the results were derived by the LDA-based classifier in a supervised manner.

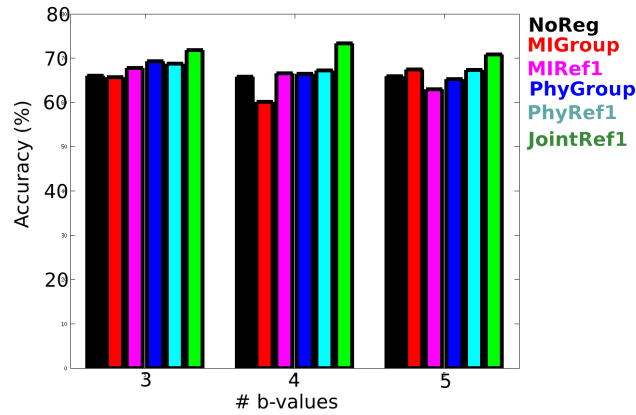


Figure 5.1: The overall classification accuracy for each of the examined methods, over the number of b-values.

of the first-order histogram parameters of both z_c and z_v images.

The specific experiment's goal was to assess the effect of registration on revealing the underlying physiology, that would help us differentiate between HD and NH disease. In each case, classification was performed by the LDA classifier, using the extracted features as its input and the labels derived by biopsy to guide the classifier. In table 5.1 we demonstrate the classification results, where one can see that JointRef1 outperformed all the rest. Note that these results were derived using a sequence of 3 b-values, which was the configuration that gave the best results for PhyRef1. For all the methods, except the proposed method (JointRef1) there was a drop on the classification accuracy over the increase in the number of b-values. However, in case of JointRef1, the classification accuracy increased when 4 b-values were used, whereas the use of 5 b-values derived slightly worst results than in the case of both 3 and 4 b-values (see figure 5.1). For every combination of b-values, the overall classification accuracy was higher with JointRef1 than with any of the rest methods (71.72%, 73.32% and 70.74% with JointRef1, whereas 65.94%, 65.79% and 65.91% with NoReg).

Correlation between Diffusion-based Imaging Biomarkers and Deauville Scores

The last result we sought for was the correlation between DW images and PET scans in characterizing tumor staging. More specifically, we wanted to assess the correlation between the afore-mentioned statistical features extracted by the afore-described diffusion-based parametric maps and the Deauville scores, that are derived by PET scans and consist of an indication of the severity of the disease, or in other words the stage of the tumor. Furthermore, we examined this correlation by using parametric maps computed by data acquired on two different phases of the treatment cycle; after two cycles of chemotherapy and in the end of the treatment. Deauville scores were given to the patients in each of these two phases. Let's denote with F_{2cycl} the feature vector extracted in such a way that is relative to the time instant after two cycles of chemotherapy, and with F_{end} the feature vector extracted in such a way that is relative to the end of the treatment. F_{2cycl} were either the difference in statistical features of the entire tumor region between the onset of the treatment and the day of the exam after 2 cycles of chemotherapy or their actual values the day of that latter exam. Similarly, F_{end} was based on either the difference in the statistical features between the onset of the treatment and the end of the treatment or their values in the end of the treatment, as well as the difference in them between the day of the exam after 2 cycles of chemotherapy and the end of treatment. Furthermore, the corresponding Deauville scores are denoted by $D_{2cycl,real}$ and $D_{end,real}$ respectively. What we want to assess is the ability of the diffusion-based biomarkers to characterize the response to therapy, therefore we are interested in the correlation between F_{2cycl} and $D_{2cycl,real}$, as well the correlation between F_{end} and $D_{end,real}$. The correlation scores were based on Pearson's correlation criterion. We set a threshold of 0.5, above which a correlation score was assumed to indicate clinical significance, in combination to a p -value lower than 0.05.

After two cycles of chemotherapy Significant correlation of diffusion-based features and PET-based staging scores were found at this phase of the treatment for both NoReg and JointRef1 case. In case of NoReg, the difference between the value of the 75 percentile of the histogram of the tumor's region in \hat{z}_c , in the beginning of the treatment and at the study after two cycles of chemotherapy, was found to be the feature giving the best correlation score with $D_{2cycl,real}$. That correlation was above the threshold of 0.5 only for the case of 5 b-values. However, when we tried to predict $D_{2cycl,real}$ using this specific feature, prediction failed. We assess the prediction success by computing the correlation between the predicted ($D_{2cycl,pred}$) and the real, PET-based Deauville scores ($D_{2cycl,real}$). We consider an accurate prediction only the one in which the latter correlation was meeting the requirements of

a clinically significant correlation described above.

On the other hand, the difference between the value in the kurtosis of the tumor's region in \hat{z}_v , in the beginning of the treatment and at the study after two cycles of chemotherapy, was found to be the feature giving the best correlation score with $D_{2cycl,real}$ in case of JointRef1. That significant correlation was found only using more than three b-values, with the case of 4 b-values giving the best results. This finding implies that $b - value = 150s/mm^2$ aids in a more accurate estimation of an diffusion-based parametric map. On the other hand, moving from four to five b-values (adding $b - value = 20s/mm^2$) didn't improve correlation, which might indicate that low b-values might not fit well to the physiological model. In the same time, using this feature to predict $D_{2cycl,real}$ did result in a set of predicted Deauville scores showing significant correlation with the real ones (see table 5.2).

However, we observed that using a combination of some features showing high correlation with $D_{2cycl,real}$ improved the prediction of the Deauville scores and this was the case only for JointRef1. We applied a linear regression model using various combinations of features extracted either from \hat{z}_c or \hat{z}_v or \hat{z}_c or \hat{z}_v . Accurate prediction was achieved only in case of using the parametric maps derived by our method, while no prediction could be attained using the parametric maps derived in the NoReg case. The best prediction score using our method was achieved when using four different features; the mean and mode values of \hat{z}_c after two cycles of chemotherapy, in combination with the difference in value between the skewness, as well as the kurtosis of the tumor's intensity distribution in \hat{z}_c , in the onset of the treatment and two cycles of chemotherapy later, using 4 b-values. In that case, the correlation was $corr = 0.71$ between predicted and actually Deauville scores, with a p -value=0.00005. In the same time, the root mean squared fitting error was 0.57 with a standard deviation of 0.69, and a value of the coefficient of determination $R^2 = 0.68$, which means that linear regression explains 68% of the variability in the Deauville scores. The corresponding number in case of NoReg, using the best combination of features towards prediction in this case, were 1.11, 1.52 and 0.37 respectively. The results on trying to predict Deauville scores after two cycles of chemotherapy can be seen in table 5.3. Finally, prediction was improved improved, in terms of a decreased mean RMSE and an increased R^2 , when using 4 instead of 3 b-values, while it decreased using 5 instead of 4 b-values, still the case of 5 b-values yielded better results than using 3 b-values (see plot left in figures 5.2 and 5.3 respectively).

In the end of the treatment: Significant correlation was found between the mean value of the tumor's region in \hat{z}_c and $D_{end,real}$ ($corr = -0.78$ with p -values 0.039), while no significant correlation was found for any statistical feature extracted by either \hat{z}_c or \hat{z}_v (NoReg case). However, even higher

Method	Feature							
	change in 75 percentile of z_c (5 b-values)				change in kurtosis of z_v (4 b-values)			
	corr.score	p -value	pred.score	p -value	corr.score	p -value	pred.score	p -value
NoReg	0.518	0.0067	0.267	0.1875	-0.377	0.0575	0.307	0.1269
JointRef1	0.295	0.1437	0.435	0.0264	-0.516	0.00070	0.511	0.0076

Table 5.2: Statistical features yielding the highest **correlation scores with tumor staging after two cycles of chemotherapy** (D_{2cycl}), shown along with their p -values, for the case of each method (change in 75 percentile of tumor region’s histogram in z_c for NoReg and change in kurtosis of tumor region’s histogram in z_v for JointRef1). The last two columns show the correlation between the corresponding predicted Deauville scores using the specific diffusion-based features and the real Deauville scores for the patients.

Features		Corr.score	p -value	mean RMSE	std of RMSE	R^2
NoReg	mean/mode of \hat{z}_c and change in skewness and kurtosis of \hat{z}_v	0.278	0.1661	1.112	1.524	0.369
JointRef1	mean/mode of \hat{z}_c and change in skewness and kurtosis of \hat{z}_v	0.709	0.00005	0.570	0.699	0.675

Table 5.3: Results on **prediction of Deauville scores after 2 cycles of chemotherapy** (D_{2cycl}). Corr.score corresponds to the correlation between predicted staging scores and actual PET-based ones. RMSE stands for root mean squared error after applying linear regression between the values of the mentioned features and Deauville scores, while R^2 corresponds to the coefficient of determination. These results were derived using 4 b-values.

Method	Feature											
	mean of z_c (4 b-values)				change in mean of z_c (4 b-values)				change in mode of z_v (4 b-values)			
	corr.score	p -value	pred.score	p -value	corr.score	p -value	pred.score	p -value	corr.score	p -value	pred.score	p -value
NoReg	-0.456	0.3039	0.645	0.1178	-0.258	0.5766	0.643	0.1195	-0.872	0.0105	0.642	0.1195
JointRef1	-0.780	0.0386	0.827	0.0217	-0.786	0.0362	0.877	0.0095	-0.970	0.0003	0.877	0.0095

Table 5.4: Statistical features yielding the highest **correlation scores with tumor staging in the end of the treatment** ($D_{end,real}$), shown along with their p -values. The last two columns again show the correlation between the corresponding predicted Deauville scores using the specific diffusion-based features and the real Deauville scores for the patients.

Features		Corr.score	p -value	mean RMSE	std of RMSE	R^2
NoReg	mean and change of mean in \hat{z}_c and change in mode of \hat{z}_v	0.645	0.1178	1.766	2.3285	0.828
JointRef1	mean and change-1 of mean in \hat{z}_c and change in mode of \hat{z}_v	0.827	0.0217	0.2019	0.2245	0.949
JointRef1	change-2 in skewness and kurtosis of \hat{z}_v	0.880	0.0089	0.1037	0.1327	0.912

Table 5.5: Results on **prediction of Deauville scores in the end of treatment** (D_{end}). As in table 5.3, Corr.score corresponds to the correlation between predicted staging scores and actual PET-based ones. RMSE stands for root mean squared error after applying linear regression between the values of the mentioned features and Deauville scores, while R^2 corresponds to the coefficient of determination. Change-1 corresponds to the change in the values between the onset and the end of the treatment, while change-2 corresponds to the change between the study after two cycles and the end of the treatment. These results were derived using 4 b-values.

correlation was found when examining the correlation using as feature the difference between the mean value in \hat{z}_c in the beginning of the treatment and the corresponding one in the end of the treatment, as well as using as feature the difference between the mode value in \hat{z}_v in the beginning of the treatment and the corresponding one in the end of the treatment ($corr = -0.79$ and $corr = -0.97$ respectively, with corresponding p -values 0.036 and 0.0003). That latter correlation was also found using the corresponding values extracted by \hat{z}_v (NoReg case), though correlation was lower than in case of *JointRef1* (see table 5.4). The negative sign in these correlation scores indicate an inverse relation between the quantities, i.e. when the

mean diffusion value in the parametric maps increase from one study to the other, the staging score should decrease and vice versa. Finally, we examined the correlation to D_{end} using an F_{end} based on the difference in the values of the statistical features extracted by the parametric maps after two cycles of chemotherapy and in the end of the treatment. In this case, no significant correlation was found, though using the difference between the kurtosis of the tumor's histogram in \tilde{z}_v gave a quite high correlation score with the p -value being a bit above the threshold of 0.05 ($corr = 0.71$ with p -value=0.0771).

Prediction of staging scores of the patients in the end of the treatment was successful for the case of JointRef1, using two different combinations of features related to the end of treatment. In the first scenario, using only the difference (between the study in the end of 2 cycles and the study in the end of treatment) in the skewness and the kurtosis of the tumor's intensity distribution in \tilde{z}_v , the correlation between the predicted D_{end} and the actual D_{end} scores was $corr = 0.88$ with p -value=0.009, while no accurate prediction was achieved using any combination of features relative to the difference in values between the study in the end of 2 cycles and the study in the end of treatment in case of NoReg. That successful prediction with *JointRef1*-based features, was accompanied by a root mean squared fitting error of 0.104 (standard deviation of 0.137) and a value for the coefficient of determination of $R^2 = 0.91$, while the corresponding values in case of NoReg were 0.419 (standard deviation of 0.515) and 0.57 respectively. Then, in the second successful scenario, prediction in *JointRef1* case was achieved using the following three features: the difference in the mean tumor value in \hat{z}_c between the onset of the treatment and the end of the treatment, the corresponding difference in the mode value of the tumor in \tilde{z}_v and the actual mean tumor value in \hat{z}_c in the study in the end of the treatment. Again no accurate prediction was attained using any combination of features derived by NoReg. In this second scenario, the root mean squared fitting error was 0.209 (standard deviation of 0.225) and a value for the coefficient of determination of $R^2 = 0.94$, while the corresponding values in case of NoReg were 1.178 (standard deviation of 2.329) and 0.83 respectively. Moreover, all the afore-mentioned results, which were the best achieved, were derived using 4 b-values. Though the coefficient of determination was higher in this second scenario than in the first one, we observed that a highly accurate prediction was achieved in term of the first scenario using 5 b-values as well, which was not the case when using 5 b-values in the second scenario. The best results regarding the prediction of Deauville scores in the end of treatment can be seen in table 5.5.

Regarding the usefulness of using a bigger number of b-values, we noticed again an improvement on the results when we use 4 instead of 3 b-values (when we add b-value = $150s/mm^2$), however in the case of 5 b-values (adding

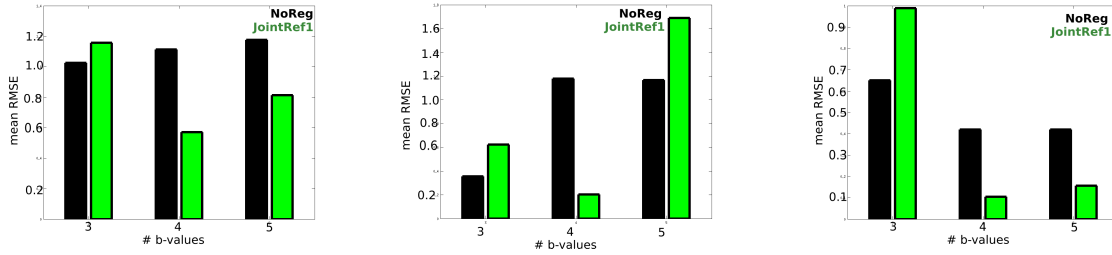


Figure 5.2: Plots of the mean RMSE of predicting Deauville scores.

In the left we plot the results for predicting $D_{2cycl,real}$. In the middle we plot the results of predicting $D_{end,real}$ using as feature combination the mean value in the tumor region a z_c image, together with the change of mean in the same image from the onset of the treatment until its end, as well and change in mode of a z_v image again from the onset of the treatment until its end. Finally in the right plot we show the results of predicting $D_{end,real}$, this time using as a feature combination the change in kurtosis and skewness of the histogram computed in the tumor region in a z_v image, from the study after 2 cycles of therapy until the end of treatment.

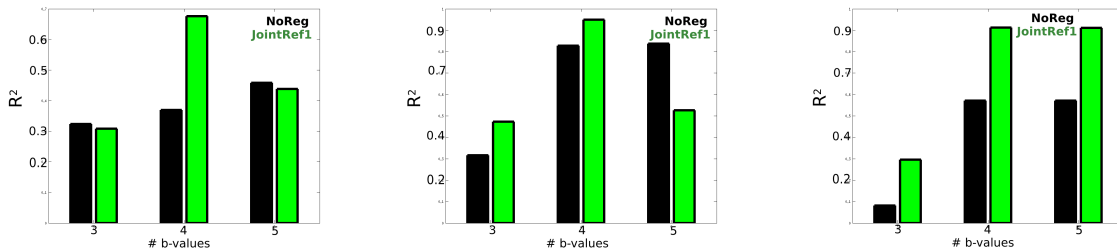


Figure 5.3: Plots of the R^2 value when predicting Deauville scores.

In the left we plot the results for predicting $D_{2cycl,real}$. In the middle we plot the results of predicting $D_{end,real}$ using as feature combination the mean value in the tumor region a z_c image, together with the change of mean in the same image from the onset of the treatment until its end, as well and change in mode of a z_v image again from the onset of the treatment until its end. Finally in the right plot we show the results of predicting $D_{end,real}$, this time using as a feature combination the change in kurtosis and skewness of the histogram computed in the tumor region in a z_v image, from the study after 2 cycles of therapy until the end of treatment.

on top b-value = $20s/mm^2$) no further improvement was observed, though results using 5 b-values were in general better than using 3 b-values (see middle and right plots in figures 5.2 and 5.3, in terms of decreasing mean RMSE and increasing R^2 respectively). These latter results might indicate that on one hand b-values higher than the value of $50s/mm^2$ fit better to the physiological model describing the diffusion process in DWI, while on the other hand small b-values ($<50s/mm^2$) don't fit well on the diffusion model. To sum up, the case of 4 b-values was the one the gave the best correlation results overall.

5.4 Discussion

This study highlights the importance of image registration as a motion correction approach in DWI, towards computing meaningful imaging biomarkers for patients with lymphomas. The proposed registration method is based on an explicit computation of an ADC map of an "extracellular diffusion"

nature (denoted as \hat{z}_c map in our framework), which is a smooth image due to spatial constraints imposed on similar tissue regions. This approach is different to the common way of computing an ADC map (see Eq.2). Two experiments were designed to evaluate the registration performance, based on simulated and real data respectively. In terms of a reconstruction error experiment using simulated data, JointRef1 outperformed all the rest in recovering more accurately both the simulated deformation fields applied to the simulated DWI sequences, as well as the simulated ADC based on which the simulated sequence was created. Moreover, JointRef1 showed the equally good to PhyGroup and PhyRef1 results on the fitting error to the diffusion model using the real dataset. PhyGroup and PhyRef1 use the fitting to the diffusion model criterion in their energy formulation. Regarding whether a preselection of a reference space is a better approach, we noticed that the methods registering the images into an intermediate reference space gave better results, as MIGroup performed better than MIREf1 in all experiments, and PhyGroup yielded better results than PhyRef1, except on the fitting error.

The latter result validated the strength of JointRef1 in correcting motion in DWI by ensuring consistency on the diffusion model. As a next step, we examined the effect of motion correction on deriving meaningful diffusion-based biomarkers. We examined the correlation of such biomarkers with both the histopathological profile of the patients and their PET scans. The former relationship was assessed through a classification experiment, in which patients were automatically classified based on the type of the lymphoma (HD or NH), using statistical features extracted by the derived by JointRegRef1 ADC maps (candidate diffusion-based biomarkers). The results in this experiment, signified the usefulness of our proposed method, as it yielded an increase on the overall classification accuracy of approximately 7.5%, compared to the NoReg case where no image registration occurred. The physiological information retrieved by JointRef1 might thus correspond to some degree with the information extracted by the histopathological analysis on the patient. To the best of our knowledge, no other study had ever looked on this relationship. Those promising results indicate that an accurate ADC map might facilitate physicians to assess the disease in a pre-treatment stage non-invasively. However, further investigation on such a classification ability through DWI should take place. The reproducibility of these results, by adding more patients in the database, is a matter that should be examined, as well the influence feature selection process has on them. For example, one could consider learning the optimal features in a supervised or unsupervised manner, or consider extracting discriminative features by approximating the intrinsic dimensionality from the subspace spanned by the tumor.

Furthermore, in terms of the correlation between DWI and PET, our scope

was to examine whether there is any diffusion-based feature that shows a significant correlation with the PET-based Deauville scores. Two different phases of the patients' treatment process were examined, the first one being the study after two cycles of chemotherapy, while the second one was the assessment of the stage of the patient's tumor after treatment (end of treatment). What we observed was that the Deauville scores were highly correlated with the change in the value of the statistical diffusion-based features, from one study to the next one. Therefore, the Deauville scores after two cycles of therapy were significantly correlated with the difference in the kurtosis of the histogram computed in the tumor's regions in the z_v image, while the same exact feature showed high correlation to the corresponding Deauville scores in the end of the treatment. High correlations were also found for the case of the change in the skewness of the histogram. The importance of these two specific features in assessing tumor's stage was confirmed by a high correlation between predicted based on a combination of these features Deauville scores and the real Deauville scores of the patients, a correlation that was the highest among all the different combinations examined in case of both after two cycles of chemotherapy and end of treatment staging scores. As Deauville scores denote the stage of lymphoma, this result indicates a potential of such biomarkers to assess lymphoma staging non-invasively. This hypothesis though is in contrast to Lin et al. [118], who reported a limited power of DWI in differentiating low-grade from high-grade lymphoma sub-types. However, no registration had been applied on that study (similar to NoReg scenario in our work). Looking though on tables 5.2 and 5.4, one can see that the majority of the features showing good correlation results were derived by JointRef1 instead of NoReg. What is also interesting noticing is the negative correlation between the mean of tumor's intensities and the grade of lymphoma's severity, which is in correspondence with the belief that high malignant tumors show low ADC values. This indication of a correlation between DWI and FDG-avid PET strengthens the argument of using the former one as the non-invasive complementary to the state-of-the-art modality for lymphoma staging, or even replacing it. PET imaging is associated with a non-negligible radiation dose, which is of particular concern for younger patients, because of the risk of radiation-induced secondary malignancies.

There have been studies that, similarly to ours, demonstrated a degree of efficacy of DWI in tumor staging. Specifically, Kwee et al. [109] had compared whole-body DW-MRI to computed tomography (CT) for the initial staging of 31 patients with HD or NH. The authors reported a 75% agreement between these two modalities, whereas in 6 patients DW-MRI classified them correctly to a higher stage than CT. A similar study of 17 patients with HD and aggressive NH was performed by Gu et al.[66] in which the newly-introduced modality was compared to FDG-PET, reporting a very high percentage of agreement (in 88% of the patients) in tumor staging between

these two modalities too. The latter study highlighted the additional value of DWI, as it raised the true-positive detection accuracy of whole-body MRI from 89% to 97%. A comparison of DWI to the FDG-PET/CT gold standard for HD and NH lymphoma pre-treatment staging was made also by Stephane et al.[194] with encouraging findings (Cohen's kappa coefficient of 0.97, with a p-value of less than 0.0001). 23 patients were examined and a size criterion, combined with the mean of ADC were used to consider node involvement. Moreover, Mayerhoefer et al.[133] concluded in their study that DWI was slightly inferior to [^{18}F]-FDG-PET with respect to pre-therapeutic regional assessment and staging in 100 patients with FDG-avid lymphomas. The evaluation of lymph node or lesion involvement was based on visualizing a high signal and an increased high signal in DW images with b-values of 50 and $1000s/mm^2$ respectively or a high signal in the DW image of small b-value, together with a low corresponding value on the ADC map. Even more encouraging results were published by Balbo et al.[11], where the authors assessed the accuracy of whole-body DWI in defining lymphoma disease stage in 41 patients. The criterion used for node-involvement in case of whole-body DWI was only hyperintensity on $b = 1000s/mm^2$ DW images.

Finally, regarding the number of b-values that are adequate for optimally computing the diffusion model, we did observe a significant improvement on the results with the increase of b-values used from three to four, indicating that the additional use of a b-value of a value higher than $50s/mm^2$ results in a better fitting to the physiological model. We didn't observe though a similar patten when adding a fifth b-value of $20s/mm^2$ value. This might be due to the small b-value, that is in the range that the physiological model is sensitive to perfusion, or it could be attributed to the fact that all the examined registration methods only approximate a consistency on the global dependencies among the images in the sequence. For more accurately imposing global consistency on the diffusion model, high-order cliques should be considered in the MRF formulation of the method.

Chapter 6

Conclusion

This thesis is concluded by summarizing the contributions and drawing some potential directions for future work.

6.1 Contributions

The principal contribution of this thesis is the development of a method to efficiently compute spatially smooth parametric maps that depict the physiological or pharmacokinetic process taking place during image acquisition and which could be used as imaging biomarkers to the evaluation of the disease or the response to chemotherapy. The experimental paradigm in this doctoral work was the computation of a map that depicts the gradient of the diffusion of water molecules in the body (ADC value). Our novel method, presented in chapter 4, simultaneously co-registers non-linearly 3D diffusion-weighted MR images and estimates the ADC map by imposing spatial constraints on its calculation. Statistical analysis on the ADC map computed by our method showed some very promising results, presented in chapter 5, that strengthen the belief of promoting the ADC as an imaging biomarker towards evaluating lymphoma patients and their response to therapy.

Our joint deformable group-wise registration and parameter estimation method was built upon our first group-wise deformable registration method, presented in chapter 3, which incorporated a physiological model describing the diffusion process in its framework. That latter registration framework was formulated as an N -layer graphical model, whereas the former one as an $N + 1$ -layer. Intra-layer edges encoded smoothness constraints for each problem while inter-layer imposed consistency between successive images in time. The resulting formulations inherit modularity and scalability. The corresponding objective function in each of the proposed registration methods is modular in the sense that various detectors/similarity metrics can be considered and addressed under a common optimization framework.

The main message of this dissertation is threefold. Firstly, image registration does help to reduce errors in ADC calculation and further improves the quality of the ADC data. Secondly, a model-based objective function instead of a model-free one renders registration more robust with respect to avoiding a sub-optimal solution. That embedded to the registration framework model should be though a valid physiological or pharmacokinetic model and the one we used in our work related to the diffusion process taking place in DWI proved to be one. Thirdly, registration and the estimation of a within tissues smooth quantitative parameter benefit great from each other, as the joint estimation of both derived better results than when estimating them sequentially. As a last more general message, we could say that the discrete formulations coupled with efficient but not restrictive approximate schemes could lead to powerful and versatile algorithms that can tackle with accuracy the registration problem.

6.2 Future Work

During this thesis we have provided promising responses, yet various extensions are under consideration to push forward the scope of our work. Let us discuss briefly, five of them.

1. The success of our joint registration and parameter estimation framework can be attributed to the imposition of a term that ensures spatial within tissue smoothness on the ADC map. However, that term tends to oversmooth the image in some cases, i.e. the borders among the various tissues become blurred in some patients. Incorporating a term that encourages intra-tissue smoothing in preference to inter-tissue smoothing seems a promising way to improve the obtained results. Perona and Malik [156] proposed a scale-space technique using a diffusion process that results images with sharp region boundaries, while a high quality edge detector can be obtained which successfully exploits global information. Such a technique could be potentially incorporated into our framework in order to achieve the afore-mentioned goal.
2. Another rational extension of our group-wise registration framework would be the use of spatial priors on the deformation fields, as well as on the parametric map, that would have a high-order dependency, instead of a pair-wise that is the case in the current implementation. Especially in the case of the ADC variables such an addition would be very beneficial since higher order interactions in image models allow for abstracting beyond pixels or voxels, building upon larger scale image attributes like edges, and for context and complex structures to be

captured. An energy formulation that would include high-order data term (as it is the case in the current formulation), as well as high-order regularization terms could be solved through Dual Decomposition by assigning the regularization terms to a slave using an optimization scheme that could tackle high-order regularization, like the Parsimonius labeling scheme proposed by Dokania and Pawan Kumar [48].

3. The validation of our non-linear group-wise registration methods had been difficult since a gold standard is not easily attainable. Researchers are forced to use a variety of surrogates, from simplified computer simulated images, to difficult experiments involving implantation of fiducials into the subject [231, 231]. An examination of different validation criteria than the ones used in this doctoral thesis, such as the Cramér–Rao lower bound (CRLB) [32], would strengthen even more the evaluation of our methods.
4. In chapter 5 we presented results on the correlation between PET-based recommendation scores and features extracted by the ADC map. These results indicate a correlation between the two modalities (PET and DWI) on the patient level. A more detailed analysis could involve multi-modal registration among PET and DW images of the same patient, in order to fuse metabolic with anatomic information derived by the two modalities respectively. To this end, a first step would be to create whole body images of the ADC, which can be achieved by applying the stitching algorithm proposed by Glocker et al. [59]. Then the multi-modal registration could be approached by the method proposed by Wachinger and Navab [216] which is based on the creation of entropy of laplacian images of both modalities, in order to allow the use of simple similarity measures, such as the intensity difference, and thus avoid the use of more sophisticated metric that would increase computational complexity.
5. Incorporating a learning process into our frameworks is another promising direction. For example, based on the groundtruth on the tumor location and shape (tumor masks) as well as the groundtruth on the type of lymphoma present in the image (disease labels), provided by the experts, we could incorporate a segmentation task in the registration framework. Assuming a probability function on the candidate labeling for each control point of the form $\pi_x(l)$ where $l \in 0, \dots, M-1$, M denoting the number of different types of lymphomas, we would wish to penalize all segmentations that go against prior information on the frequency of appearance of a specific type of tumor on the body. Such probabilities can be learned using either a machine learning method, such as

support vector machines (SVM) or a deep learning technique, such as Convolutional Neural Networks (CNNs).

Bibliography

- [1] Adluru, G., DiBella, E. V., and Schabel, M. C. (2006). Model-based registration for dynamic cardiac perfusion mri. *Journal of Magnetic Resonance Imaging*, 24(5):1062–1070.
- [2] Alam, F. and Rahman, S. U. (2016). Intrinsic registration techniques for medical images: A state-of-the-art review. *Journal of Postgraduate Medical Institute (Peshawar-Pakistan)*, 30(2).
- [3] Albano, D., Patti, C., La Grutta, L., Agnello, F., Grassedonio, E., Mulè, A., Cannizzaro, G., Ficola, U., Lagalla, R., Midiri, M., et al. (2016). Comparison between whole-body mri with diffusion-weighted imaging and pet/ct in staging newly diagnosed fdg-avid lymphomas. *European journal of radiology*, 85(2):313–318.
- [4] Alchatzidis, S., Sotiras, A., and Paragios, N. (2014). Discrete multi atlas segmentation using agreement constraints. In *British Machine Vision Conference*.
- [5] Alchatzidis, S., Sotiras, A., and Paragios, N. (2015). Local atlas selection for discrete multi-atlas segmentation. In *International Symposium on Biomedical Imaging*.
- [6] Alchatzidis, S., Sotiras, A., Zacharaki, E. I., and Paragios, N. (2016). A discrete mrf framework for integrated multi-atlas registration and segmentation. *International Journal of Computer Vision*, pages 1–13.
- [7] Andres, B., Kappes, J. H., Beier, T., Köthe, U., and Hamprecht, F. A. (2012). The lazy flipper: Efficient depth-limited exhaustive search in discrete graphical models. In *European Conference on Computer Vision*, pages 154–166. Springer.
- [8] Attariwala, R. and Picker, W. (2013). Whole body mri: improved lesion detection and characterization with diffusion weighted techniques. *Journal of Magnetic Resonance Imaging*, 38(2):253–268.
- [9] Avants, B. and Gee, J. C. (2004). Geodesic estimation for large deformation anatomical shape averaging and interpolation. *Neuroimage*, 23:S139–S150.

- [10] Baillard, C., Hellier, P., and Barillot, C. (2001). Segmentation of brain 3d mr images using level sets and dense registration. *Medical image analysis*, 5(3):185–194.
- [11] Balbo-Mussetto, A., Cirillo, S., Bruna, R., Gueli, A., Saviolo, C., Petracchini, M., Fornari, A., Lario, C., Gottardi, D., De Crescenzo, A., et al. (2015). Whole-body mri with diffusion-weighted imaging: a valuable alternative to contrast-enhanced ct for initial staging of aggressive lymphoma. *Clinical radiology*.
- [12] Balci, S. K., Golland, P., Shenton, M., and Wells, W. M. (2007a). Free-form b-spline deformation model for groupwise registration. In *Medical image computing and computer-assisted intervention: MICCAI... International Conference on Medical Image Computing and Computer-Assisted Intervention*, volume 10, page 23. NIH Public Access.
- [13] Balci, S. K., Golland, P., and Wells, W. (2007b). Non-rigid groupwise registration using b-spline deformation model. *Open source and open data for MICCAI*, pages 105–121.
- [14] Baloch, S. and Davatzikos, C. (2009). Morphological appearance manifolds in computational anatomy: Groupwise registration and morphological analysis. *NeuroImage*, 45(1):S73–S85.
- [15] Bammer, R. (2003). Basic principles of diffusion-weighted imaging. *European journal of radiology*, 45(3):169–184.
- [16] Bauer, S., Berkels, B., Hornegger, J., and Rumpf, M. (2011). Joint of image denoising and registration with a ct surface in radiation therapy. In *International Conference on Scale Space and Variational Methods in Computer Vision*, pages 98–109. Springer.
- [17] Besag, J. (1993). Statistical analysis of dirty pictures. *Journal of applied statistics*, 20(5-6):63–87.
- [18] Besl, P. J. and McKay, N. D. (1992). Method for registration of 3-d shapes. In *Robotics-DL tentative*, pages 586–606. International Society for Optics and Photonics.
- [19] Bhatia, K. K., Hajnal, J. V., Puri, B. K., Edwards, A. D., and Rueckert, D. (2004). Consistent groupwise non-rigid registration for atlas construction. In *Biomedical Imaging: Nano to Macro, 2004. IEEE International Symposium on*, pages 908–911. IEEE.
- [20] Bhushan, M., Schnabel, J. A., Risser, L., Heinrich, M. P., Brady, J. M., and Jenkinson, M. (2011). Motion correction and parameter estimation in dcemri sequences: application to colorectal cancer. In *International Conference on Medical Image Computing and Computer-Assisted Intervention*, pages 476–483. Springer.

- [21] Bidaut, L. M. and Vallée, J.-P. (2001). Automated registration of dynamic mr images for the quantification of myocardial perfusion. *Journal of magnetic resonance imaging*, 13(4):648–655.
- [22] Black, M. J., Fleet, D. J., and Yacoob, Y. (1998). A framework for modeling appearance change in image sequences. In *Computer Vision, 1998. Sixth International Conference on*, pages 660–667. IEEE.
- [23] Boldea, V., Sharp, G. C., Jiang, S. B., and Sarrut, D. (2008). 4d-ct lung motion estimation with deformable registration: quantification of motion nonlinearity and hysteresis. *Medical physics*, 35(3):1008–1018.
- [24] Bookstein, F. L. (1991). Thin-plate splines and the atlas problem for biomedical images. In *Biennial International Conference on Information Processing in Medical Imaging*, pages 326–342. Springer.
- [25] Bouzebda, S., Elhattab, I., Keziou, A., and Lounis, T. (2013). New entropy estimator with an application to test of normality. *Communications in Statistics-Theory and Methods*, 42(12):2245–2270.
- [26] Boykov, Y. and Kolmogorov, V. (2004). An experimental comparison of min-cut/max-flow algorithms for energy minimization in vision. *IEEE transactions on pattern analysis and machine intelligence*, 26(9):1124–1137.
- [27] Boykov, Y., Veksler, O., and Zabih, R. (2001). Fast approximate energy minimization via graph cuts. *IEEE Transactions on pattern analysis and machine intelligence*, 23(11):1222–1239.
- [28] Brown, L. G. (1992). A survey of image registration techniques. *ACM computing surveys (CSUR)*, 24(4):325–376.
- [29] Buonaccorsi, G. A., O'Connor, J. P., Counce, A., Roberts, C., Cheung, S., Watson, Y., Davies, K., Hope, L., Jackson, A., Jayson, G. C., et al. (2007). Tracer kinetic model-driven registration for dynamic contrast-enhanced mri time-series data. *Magnetic Resonance in Medicine*, 58(5):1010–1019.
- [30] Bystrov, D., Vik, T., Schulz, H., Klinder, T., and Schmidt, S. (2009). Local motion analysis in 4d lung ct using fast groupwise registration. In *Image Processing (ICIP), 2009 16th IEEE International Conference on*, pages 1749–1752. IEEE.
- [31] Castillo, E., Castillo, R., Martinez, J., Shenoy, M., and Guerrero, T. (2009). Four-dimensional deformable image registration using trajectory modeling. *Physics in medicine and biology*, 55(1):305.
- [32] Cavassila, S., Deval, S., Huegen, C., Van Ormondt, D., and Graveron-Demilly, D. (2001). Cramér-rao bounds: an evaluation tool for quantitation. *NMR in Biomedicine*, 14(4):278–283.

- [33] Chan, M., Herman, G. T., and Levitan, E. (1995). Bayesian image reconstruction using a high-order interacting mrf model. In *International Conference on Image Analysis and Processing*, pages 608–614. Springer.
- [34] Chavhan, G. B., Babyn, P. S., and Vasanawala, S. S. (2013). Abdominal mr imaging in children: motion compensation, sequence optimization, and protocol organization. *Radiographics*, 33(3):703–719.
- [35] Cheson, B. D., Pfistner, B., Juweid, M. E., Gascoyne, R. D., Specht, L., Horning, S. J., Coiffier, B., Fisher, R. I., Hagenbeek, A., Zucca, E., et al. (2007). Revised response criteria for malignant lymphoma. *Journal of Clinical Oncology*, 25(5):579–586.
- [36] Christensen, G. E. and Johnson, H. J. (2001). Consistent image registration. *IEEE transactions on medical imaging*, 20(7):568–582.
- [37] Collignon, A., Maes, F., Delaere, D., Vandermeulen, D., Suetens, P., and Marchal, G. (1995). Automated multi-modality image registration based on information theory. In *Information processing in medical imaging*, volume 3, pages 263–274.
- [38] Cootes, T. F., Marsland, S., Twining, C. J., Smith, K., and Taylor, C. J. (2004). Groupwise diffeomorphic non-rigid registration for automatic model building. In *European conference on computer vision*, pages 316–327. Springer.
- [39] Cootes, T. F. and Taylor, C. J. (1999). A mixture model for representing shape variation. *Image and Vision Computing*, 17(8):567–573.
- [40] Cootes, T. F., Twining, C. J., Petrovic, V. S., Babalola, K. O., and Taylor, C. J. (2010). Computing accurate correspondences across groups of images. *IEEE transactions on pattern analysis and machine intelligence*, 32(11):1994–2005.
- [41] Cordero-Grande, L., Merino-Caviedes, S., Aja-Fernández, S., and Alberola-López, C. (2013). Groupwise elastic registration by a new sparsity-promoting metric: application to the alignment of cardiac magnetic resonance perfusion images. *IEEE transactions on pattern analysis and machine intelligence*, 35(11):2638–2650.
- [42] CRD, G. (2000). Statistical methods for tomographic image reconstruction.
- [43] Crum, W. R., Modo, M., Vernon, A. C., Barker, G. J., and Williams, S. C. (2013). Registration of challenging pre-clinical brain images. *Journal of neuroscience methods*, 216(1):62–77.
- [44] Davies, R. H., Twining, C. J., and Taylor, C. (2008). Groupwise surface correspondence by optimization: Representation and regularization. *Medical image analysis*, 12(6):787–796.

- [45] Davis, B. C., Fletcher, P. T., Bullitt, E., and Joshi, S. (2010). Population shape regression from random design data. *International journal of computer vision*, 90(2):255–266.
- [46] De Craene, M., Camara, O., Bijnens, B. H., and Frangi, A. F. (2009). Large diffeomorphic ffd registration for motion and strain quantification from 3d-us sequences. In *International Conference on Functional Imaging and Modeling of the Heart*, pages 437–446. Springer.
- [47] Dietrich, O., Biffar, A., Baur-Melnyk, A., and Reiser, M. F. (2010). Technical aspects of mr diffusion imaging of the body. *European journal of radiology*, 76(3):314–322.
- [48] Dokania, P. K. and Pawan Kumar, M. (2015). Parsimonious labeling. In *Proceedings of the IEEE International Conference on Computer Vision*, pages 1760–1768.
- [49] Droske, M. and Rumpf, M. (2007). Multiscale joint segmentation and registration of image morphology. *IEEE transactions on pattern analysis and machine intelligence*, 29(12):2181–2194.
- [50] Durrleman, S., Pennec, X., Trouvé, A., Gerig, G., and Ayache, N. (2009). Spatiotemporal atlas estimation for developmental delay detection in longitudinal datasets. In *International Conference on Medical Image Computing and Computer-Assisted Intervention*, pages 297–304. Springer.
- [51] Eastwood, J. D., Lev, M. H., Wintermark, M., Fitzek, C., Barboriak, D. P., Delong, D. M., Lee, T.-Y., Azhari, T., Herzau, M., Chilukuri, V. R., et al. (2003). Correlation of early dynamic ct perfusion imaging with whole-brain mr diffusion and perfusion imaging in acute hemispheric stroke. *American Journal of Neuroradiology*, 24(9):1869–1875.
- [52] Ehman, R. L., McNamara, M., Pallack, M., Hricak, H., and Higgins, C. (1984). Magnetic resonance imaging with respiratory gating: techniques and advantages. *American journal of Roentgenology*, 143(6):1175–1182.
- [53] Ferrante, E. (2016). *Graph-based deformable registration: slice-to-volume mapping and context specific methods*. PhD thesis, Université Paris-Saclay.
- [54] Geman, S. and Geman, D. (1984). Stochastic relaxation, gibbs distributions, and the bayesian restoration of images. *IEEE Transactions on pattern analysis and machine intelligence*, (6):721–741.
- [55] Geng, X., Christensen, G. E., Gu, H., Ross, T. J., and Yang, Y. (2009). Implicit reference-based group-wise image registration and its application to structural and functional mri. *Neuroimage*, 47(4):1341–1351.
- [56] Glocker, B. (2009). drop-user guide version 1.05.
- [57] Glocker, B., Komodakis, N., Tziritas, G., Navab, N., and Paragios, N. (2008). Dense image registration through mrfs and efficient linear programming. *Medical image analysis*, 12(6):731–741.

- [58] Glocker, B., Sotiras, A., Komodakis, N., and Paragios, N. (2011). Deformable medical image registration: Setting the state of the art with discrete methods*. *Annual review of biomedical engineering*, 13:219–244.
- [59] Glocker, B., Wachinger, C., Zeltner, J., Paragios, N., Komodakis, N., Hansen, M., and Navab, N. (2009). Mri composing for whole body imaging. In *Bildverarbeitung für die Medizin 2009*, pages 420–424. Springer.
- [60] Goodall, C. (1991). Procrustes methods in the statistical analysis of shape. *Journal of the Royal Statistical Society. Series B (Methodological)*, pages 285–339.
- [61] Gooya, A., Pohl, K. M., Bilello, M., Biros, G., and Davatzikos, C. (2011). Joint segmentation and deformable registration of brain scans guided by a tumor growth model. In *International Conference on Medical Image Computing and Computer-Assisted Intervention*, pages 532–540. Springer.
- [62] Gooya, A., Pohl, K. M., Bilello, M., Cirillo, L., Biros, G., Melhem, E. R., and Davatzikos, C. (2012). Glistr: glioma image segmentation and registration. *IEEE transactions on medical imaging*, 31(10):1941–1954.
- [63] Goshtasby, A. A. (2012). *Image registration: Principles, tools and methods*. Springer Science & Business Media.
- [64] Gray, A. J., Kay, J., and Titterington, D. (1994). An empirical study of the simulation of various models used for images. *IEEE Transactions on pattern analysis and machine intelligence*, 16(5):507–513.
- [65] Gray, G. A. and Kolda, T. G. (2004). Appspack 4.0: Asynchronous parallel pattern search for derivative-free optimization. *Sandia Report SAND2004-6391*, Sandia National Laboratories, Livermore, CA.
- [66] Gu, J., Chan, T., Zhang, J., Leung, A. Y., Kwong, Y.-L., and Khong, P.-L. (2011). Whole-body diffusion-weighted imaging: the added value to whole-body mri at initial diagnosis of lymphoma. *American Journal of Roentgenology*, 197(3):W384–W391.
- [67] Guyader, J.-M., Bernardin, L., Douglas, N. H., Poot, D. H., Niessen, W. J., and Klein, S. (2015). Influence of image registration on apparent diffusion coefficient images computed from free-breathing diffusion mr images of the abdomen. *Journal of Magnetic Resonance Imaging*, 42(2):315–330.
- [68] Haioun, C., Itti, E., Rahmouni, A., Brice, P., Rain, J.-D., Belhadj, K., Gaulard, P., Garderet, L., Lepage, E., Reyes, F., et al. (2005). [18f] fluoro-2-deoxy-d-glucose positron emission tomography (fdg-pet) in aggressive lymphoma: an early prognostic tool for predicting patient outcome. *Blood*, 106(4):1376–1381.

- [69] Hamm, J., Davatzikos, C., and Verma, R. (2009). Efficient large deformation registration via geodesics on a learned manifold of images. In *International Conference on Medical Image Computing and Computer-Assisted Intervention*, pages 680–687. Springer.
- [70] Hampel, F. R., Ronchetti, E. M., Rousseeuw, P. J., and Stahel, W. A. (2011). *Robust statistics: the approach based on influence functions*, volume 114. John Wiley & Sons.
- [71] Hamrouni, S., Rougon, N., and Prêteux, F. (2011). Multi-feature information-theoretic image registration: application to groupwise registration of perfusion mri exams. In *2011 IEEE International Symposium on Biomedical Imaging: From Nano to Macro*, pages 574–577. IEEE.
- [72] Hamy, V., Dikaios, N., Punwani, S., Melbourne, A., Latifoltojar, A., Makanyanga, J., Chouhan, M., Helbren, E., Menys, A., Taylor, S., et al. (2014). Respiratory motion correction in dynamic mri using robust data decomposition registration—application to dce-mri. *Medical image analysis*, 18(2):301–313.
- [73] Hamza, A. B. and Krim, H. (2003). Jensen-rényi divergence measure: theoretical and computational perspectives. In *IEEE International Symposium on Information Theory*, pages 257–257.
- [74] Han, J., Berkels, B., Rumpf, M., Hornegger, J., Droske, M., Fried, M., Scorzin, J., and Schaller, C. (2006). A variational framework for joint image registration, denoising and edge detection. In *Bildverarbeitung für die Medizin 2006*, pages 246–250. Springer.
- [75] Heijmen, L., Verstappen, M. C., Ter Voert, E. E., Punt, C. J., Oyen, W. J., de Geus-Oei, L.-F., Hermans, J. J., Heerschap, A., and van Laarhoven, H. W. (2012). Tumour response prediction by diffusion-weighted mr imaging: ready for clinical use? *Critical reviews in oncology/hematology*, 83(2):194–207.
- [76] Hill, D. L., Batchelor, P. G., Holden, M., and Hawkes, D. J. (2001). Medical image registration. *Physics in medicine and biology*, 46(3):R1.
- [77] Hoffman, E. J., Phelps, M. E., Wisenberg, G., Schelbert, H. R., and Kuhl, D. E. (1979). Electrocardiographic gating in positron emission computed tomography. *Journal of computer assisted tomography*, 3(6):733–hyhen.
- [78] Holden, M. (2008). A review of geometric transformations for nonrigid body registration. *Medical Imaging, IEEE Transactions on*, 27(1):111–128.
- [79] Horn, B. K. and Schunck, B. G. (1981). Determining optical flow. *Artificial intelligence*, 17(1-3):185–203.
- [80] Huang, X., Paragios, N., and Metaxas, D. N. (2006). Shape registration in implicit spaces using information theory and free form deformations. *IEEE transactions on pattern analysis and machine intelligence*, 28(8):1303–1318.

- [81] Huizinga, W., Poot, D. H., Guyader, J.-M., Smit, H., van Kranenburg, M., van Geuns, R.-J. M., Uitterdijk, A., van Beusekom, H. M., Coolen, B. F., Leemans, A., et al. (2014). Non-rigid groupwise image registration for motion compensation in quantitative mri. In *International Workshop on Biomedical Image Registration*, pages 184–193. Springer.
- [82] Iglesias, J. E., Sabuncu, M. R., and Van Leemput, K. (2013). A unified framework for cross-modality multi-atlas segmentation of brain mri. *Medical image analysis*, 17(8):1181–1191.
- [83] Ishikawa, H. (2009). Higher-order clique reduction in binary graph cut. In *Computer Vision and Pattern Recognition, 2009. CVPR 2009. IEEE Conference on*, pages 2993–3000. IEEE.
- [84] Ivancevic, M. K., Kwee, T. C., Takahara, T., Ogino, T., Hussain, H. K., Liu, P. S., and Chenevert, T. L. (2009). Diffusion-weighted mr imaging of the liver at 3.0 tesla using tracking only navigator echo (tron): A feasibility study. *Journal of Magnetic Resonance Imaging*, 30(5):1027–1033.
- [85] Jia, H., Wu, G., Wang, Q., and Shen, D. (2010). Absorb: Atlas building by self-organized registration and bundling. *NeuroImage*, 51(3):1057–1070.
- [86] Jia, H., Wu, G., Wang, Q., Wang, Y., Kim, M., and Shen, D. (2012). Directed graph based image registration. *Computerized Medical Imaging and Graphics*, 36(2):139–151.
- [87] Joshi, S., Davis, B., Jomier, M., and Gerig, G. (2004). Unbiased diffeomorphic atlas construction for computational anatomy. *NeuroImage*, 23:S151–S160.
- [88] Just, N. (2014). Improving tumour heterogeneity mri assessment with histograms. *British journal of cancer*, 111(12):2205–2213.
- [89] Juweid, M. E., Stroobants, S., Hoekstra, O. S., Mottaghy, F. M., Dietlein, M., Guermazi, A., Wiseman, G. A., Kostakoglu, L., Scheidhauer, K., Buck, A., et al. (2007). Use of positron emission tomography for response assessment of lymphoma: consensus of the imaging subcommittee of international harmonization project in lymphoma. *Journal of Clinical Oncology*, 25(5):571–578.
- [90] Kandpal, H., Sharma, R., Madhusudhan, K. S., and Kapoor, K. S. (2009). Respiratory-triggered versus breath-hold diffusion-weighted mri of liver lesions: comparison of image quality and apparent diffusion coefficient values. *American Journal of Roentgenology*, 192(4):915–922.
- [91] Kappes, J., Andres, B., Hamprecht, F., Schnorr, C., Nowozin, S., Batra, D., Kim, S., Kausler, B., Lellmann, J., Komodakis, N., et al. (2013). A comparative study of modern inference techniques for discrete energy minimization problems. In *Proceedings of the IEEE Conference on Computer Vision and Pattern Recognition*, pages 1328–1335.

- [92] Kaus, M. R., Netsch, T., Kabus, S., Pekar, V., McNutt, T., and Fischer, B. (2004). Estimation of organ motion from 4d ct for 4d radiation therapy planning of lung cancer. In *International Conference on Medical Image Computing and Computer-Assisted Intervention*, pages 1017–1024. Springer.
- [93] Kirkpatrick, S., Gelatt, C. D., Vecchi, M. P., et al. (1983). Optimization by simulated annealing. *science*, 220(4598):671–680.
- [94] Klein, A., Andersson, J., Ardekani, B. A., Ashburner, J., Avants, B., Chiang, M.-C., Christensen, G. E., Collins, D. L., Gee, J., Hellier, P., et al. (2009). Evaluation of 14 nonlinear deformation algorithms applied to human brain mri registration. *Neuroimage*, 46(3):786–802.
- [95] Koh, D.-M. and Collins, D. J. (2007). Diffusion-weighted mri in the body: applications and challenges in oncology. *American Journal of Roentgenology*, 188(6):1622–1635.
- [96] Komodakis, N. and Paragios, N. (2009). Beyond pairwise energies: Efficient optimization for higher-order mrfs. In *Computer Vision and Pattern Recognition, 2009. CVPR 2009. IEEE Conference on*, pages 2985–2992. IEEE.
- [97] Komodakis, N., Paragios, N., and Tziritas, G. (2011). Mrf energy minimization and beyond via dual decomposition. *Pattern Analysis and Machine Intelligence, IEEE Transactions on*, 33(3):531–552.
- [98] Komodakis, N. and Tziritas, G. (2005). A new framework for approximate labeling via graph cuts. In *Computer Vision, 2005. ICCV 2005. Tenth IEEE International Conference on*, volume 2, pages 1018–1025. IEEE.
- [99] Komodakis, N. and Tziritas, G. (2007). Approximate labeling via graph cuts based on linear programming. *IEEE transactions on pattern analysis and machine intelligence*, 29(8):1436–1453.
- [100] Komodakis, N., Tziritas, G., and Paragios, N. (2007). Fast, approximately optimal solutions for single and dynamic mrfs. In *Computer Vision and Pattern Recognition, 2007. CVPR'07. IEEE Conference on*, pages 1–8. IEEE.
- [101] Komodakis, N., Tziritas, G., and Paragios, N. (2008). Performance vs computational efficiency for optimizing single and dynamic mrfs: Setting the state of the art with primal-dual strategies. *Computer Vision and Image Understanding*, 112(1):14–29.
- [102] Korin, H. W., Ehman, R. L., Riederer, S. J., Felmlee, J. P., and Grimm, R. C. (1992). Respiratory kinematics of the upper abdominal organs: a quantitative study. *Magnetic resonance in medicine*, 23(1):172–178.
- [103] Kornaropoulos, E. N., Niazi, M., Lozanski, G., and Gurcan, M. N. (2014). Histopathological image analysis for centroblasts classification through dimensionality reduction approaches. *Cytometry Part A*, 85(3):242–255.

- [104] Kornaropoulos, E. N., Zacharaki, E. I., Zerbib, P., Lin, C., Rahmouni, A., and Paragios, N. (2016). Deformable group-wise registration using a physiological model: application to diffusion-weighted mri. In *IEEE International Conference on Image Processing (ICIP)*.
- [105] Kubo, H. D. and Hill, B. C. (1996). Respiration gated radiotherapy treatment: a technical study. *Physics in medicine and biology*, 41(1):83.
- [106] Kwee, T. C., Takahara, T., Ochiai, R., Katahira, K., Van Cauteren, M., Imai, Y., Nievelstein, R. A., and Luijten, P. R. (2009a). Whole-body diffusion-weighted magnetic resonance imaging. *European journal of radiology*, 70(3):409–417.
- [107] Kwee, T. C., Takahara, T., Ochiai, R., Nievelstein, R. A., and Luijten, P. R. (2008). Diffusion-weighted whole-body imaging with background body signal suppression (dwibs): features and potential applications in oncology. *European radiology*, 18(9):1937–1952.
- [108] Kwee, T. C., Takahara, T., Vermoolen, M. A., Bierings, M. B., Mali, W. P., and Nievelstein, R. A. (2010). Whole-body diffusion-weighted imaging for staging malignant lymphoma in children. *Pediatric radiology*, 40(10):1592–1602.
- [109] Kwee, T. C., van Ufford, H. M. Q., Beek, F. J., Takahara, T., Uiterwaal, C. S., Bierings, M. B., Ludwig, I., Fijnheer, R., and Nievelstein, R. A. (2009b). Whole-body mri, including diffusion-weighted imaging, for the initial staging of malignant lymphoma: comparison to computed tomography. *Investigative radiology*, 44(10):683–690.
- [110] Lauenstein, T. C. and Semelka, R. C. (2006). Emerging techniques: Whole-body screening and staging with mri. *Journal of Magnetic Resonance Imaging*, 24(3):489–498.
- [111] Le Bihan, D., Breton, E., Lallemand, D., Aubin, M., Vignaud, J., and Laval-Jeantet, M. (1988). Separation of diffusion and perfusion in intravoxel incoherent motion mr imaging. *Radiology*, 168(2):497–505.
- [112] Learned-Miller, E. G. (2006). Data driven image models through continuous joint alignment. *IEEE Transactions on Pattern Analysis and Machine Intelligence*, 28(2):236–250.
- [113] Leordeanu, M. and Hebert, M. (2005). A spectral technique for correspondence problems using pairwise constraints. In *Computer Vision, 2005. ICCV 2005. Tenth IEEE International Conference on*, volume 2, pages 1482–1489. IEEE.
- [114] Levitan, E., Chan, M., and Herman, G. T. (1995). Image-modeling gibbs priors. *Graphical models and image processing*, 57(2):117–130.
- [115] Li, C., Sun, Y., and Chai, P. (2011). Pseudo ground truth based nonrigid registration of myocardial perfusion mri. *Medical image analysis*, 15(4):449–459.

- [116] Li, G., Citrin, D., Camphausen, K., Mueller, B., Burman, C., Mychalczak, B., Miller, R. W., and Song, Y. (2008). Advances in 4d medical imaging and 4d radiation therapy. *Technology in cancer research & treatment*, 7(1):67–81.
- [117] Liao, S., Jia, H., Wu, G., and Shen, D. (2011). A novel longitudinal atlas construction framework by groupwise registration of subject image sequences. In *Information Processing in Medical Imaging*, pages 283–295. Springer.
- [118] Lin, C., Luciani, A., Itti, E., Haioun, C., Safar, V., Meignan, M., et al. (2012). Whole-body diffusion magnetic resonance imaging in the assessment of lymphoma. *Cancer Imaging*, 12(2):403–408.
- [119] Ling, C. C., Humm, J., Larson, S., Amols, H., Fuks, Z., Leibel, S., and Koutcher, J. A. (2000). Towards multidimensional radiotherapy (md-crt): biological imaging and biological conformality. *International Journal of Radiation Oncology* Biology* Physics*, 47(3):551–560.
- [120] Lorenzen, P. J. and Joshi, S. C. (2003). High-dimensional multimodal image registration. In *International Workshop on Biomedical Image Registration*, pages 234–243. Springer.
- [121] Lorenzo-Valdés, M., Sanchez-Ortiz, G. I., Mohiaddin, R., and Rueckert, D. (2002). Atlas-based segmentation and tracking of 3d cardiac mr images using non-rigid registration. In *International Conference on Medical Image Computing and Computer-Assisted Intervention*, pages 642–650. Springer.
- [122] Lu, C., Chelikani, S., Jaffray, D. A., Milosevic, M. F., Staib, L. H., and Duncan, J. S. (2012). Simultaneous nonrigid registration, segmentation, and tumor detection in mri guided cervical cancer radiation therapy. *IEEE transactions on medical imaging*, 31(6):1213–1227.
- [123] Luenberger, D. G. (1973). *Introduction to linear and nonlinear programming*, volume 28. Addison-Wesley Reading, MA.
- [124] Maes, F., Collignon, A., Vandermeulen, D., Marchal, G., and Suetens, P. (1997). Multimodality image registration by maximization of mutual information. *IEEE transactions on medical imaging*, 16(2):187–198.
- [125] Mahapatra, D. (2012). Groupwise registration of dynamic cardiac perfusion images using temporal dynamics and segmentation information. In *SPIE Medical Imaging*, pages 83141X–83141X. International Society for Optics and Photonics.
- [126] Mahapatra, D. (2013). Joint segmentation and groupwise registration of cardiac perfusion images using temporal information. *Journal of digital imaging*, 26(2):173–182.

- [127] Mahapatra, D., Li, Z., Vos, F., and Buhmann, J. (2015). Joint segmentation and groupwise registration of cardiac dce mri using sparse data representations. In *Biomedical Imaging (ISBI), 2015 IEEE 12th International Symposium on*, pages 1312–1315. IEEE.
- [128] Mahapatra, D. and Sun, Y. (2010). Joint registration and segmentation of dynamic cardiac perfusion images using mrfs. In *International Conference on Medical Image Computing and Computer-Assisted Intervention*, pages 493–501. Springer.
- [129] Mahapatra, D. and Sun, Y. (2012). Integrating segmentation information for improved mrf-based elastic image registration. *IEEE Transactions on Image Processing*, 21(1):170–183.
- [130] Maintz, J. A. and Viergever, M. A. (1998). A survey of medical image registration. *Medical image analysis*, 2(1):1–36.
- [131] Marsland, S., Twining, C. J., and Taylor, C. J. (2003). Groupwise non-rigid registration using polyharmonic clamped-plate splines. In *International Conference on Medical Image Computing and Computer-Assisted Intervention*, pages 771–779. Springer.
- [132] Marsland, S., Twining, C. J., and Taylor, C. J. (2008). A minimum description length objective function for groupwise non-rigid image registration. *Image and Vision Computing*, 26(3):333–346.
- [133] Mayerhoefer, M. E., Karanikas, G., Kletter, K., Prosch, H., Kiesewetter, B., Skrabs, C., Porpaczy, E., Weber, M., Pinker-Domenig, K., Berzaczy, D., et al. (2014). Evaluation of diffusion-weighted mri for pretherapeutic assessment and staging of lymphoma: results of a prospective study in 140 patients. *Clinical Cancer Research*, 20(11):2984–2993.
- [134] Mazaheri, Y., Do, R. K., Shukla-Dave, A., Deasy, J. O., Lu, Y., and Akin, O. (2012). Motion correction of multi-b-value diffusion-weighted imaging in the liver. *Academic radiology*, 19(12):1573–1580.
- [135] McInerney, T. and Terzopoulos, D. (1996). Deformable models in medical image analysis: a survey. *Medical image analysis*, 1(2):91–108.
- [136] Melbourne, A., Atkinson, D., White, M., Collins, D., Leach, M., and Hawkes, D. (2007). Registration of dynamic contrast-enhanced mri using a progressive principal component registration (ppcr). *Physics in medicine and biology*, 52(17):5147.
- [137] Melbourne, A., Hipwell, J., Modat, M., Mertzaniidou, T., Huisman, H., Ourselin, S., and Hawkes, D. (2011). The effect of motion correction on pharmacokinetic parameter estimation in dynamic-contrast-enhanced mri. *Physics in medicine and biology*, 56(24):7693.

- [138] Metz, C., Klein, S., Schaap, M., van Walsum, T., and Niessen, W. J. (2011). Nonrigid registration of dynamic medical imaging data using nd+ t b-splines and a groupwise optimization approach. *Medical image analysis*, 15(2):238–249.
- [139] Mikolajczyk, K. and Schmid, C. (2005). A performance evaluation of local descriptors. *IEEE transactions on pattern analysis and machine intelligence*, 27(10):1615–1630.
- [140] Miller, E. G., Matsakis, N. E., and Viola, P. A. (2000). Learning from one example through shared densities on transforms. In *Computer Vision and Pattern Recognition, 2000. Proceedings. IEEE Conference on*, volume 1, pages 464–471. IEEE.
- [141] Milles, J., van der Geest, R. J., Jerosch-Herold, M., Reiber, J. H., and Lelieveldt, B. P. (2008). Fully automated motion correction in first-pass myocardial perfusion mr image sequences. *IEEE Transactions on Medical Imaging*, 27(11):1611–1621.
- [142] Modat, M., Ridgway, G. R., Taylor, Z. A., Lehmann, M., Barnes, J., Hawkes, D. J., Fox, N. C., and Ourselin, S. (2010). Fast free-form deformation using graphics processing units. *Computer methods and programs in biomedicine*, 98(3):278–284.
- [143] Murphy, K. P., Weiss, Y., and Jordan, M. I. (1999). Loopy belief propagation for approximate inference: An empirical study. In *Proceedings of the Fifteenth conference on Uncertainty in artificial intelligence*, pages 467–475. Morgan Kaufmann Publishers Inc.
- [144] Myronenko, A. and Song, X. (2010). Intensity-based image registration by minimizing residual complexity. *IEEE Transactions on Medical Imaging*, 29(11):1882–1891.
- [145] Nakanishi, K., Kobayashi, M., Nakaguchi, K., KYAKUNO, M., HASHIMOTO, N., ONISHI, H., MAEDA, N., NAKATA, S., KUWABARA, M., MURAKAMI, T., et al. (2007). Whole-body mri for detecting metastatic bone tumor: diagnostic value of diffusion-weighted images. *Magnetic Resonance in Medical Sciences*, 6(3):147–155.
- [146] Orchard, J. and Mann, R. (2010). Registering a multisensor ensemble of images. *IEEE Transactions on Image Processing*, 19(5):1236–1247.
- [147] Padera, T. P., Stoll, B. R., Rooredman, J. B., Capen, D., et al. (2004). Cancer cells compress intratumour vessels. *Nature*, 427(6976):695.
- [148] Padhani, A. R., Liu, G., Mu-Koh, D., Chenevert, T. L., Thoeny, H. C., Takahara, T., Dzik-Jurasz, A., Ross, B. D., Van Cauteren, M., Collins, D., et al. (2009). Diffusion-weighted magnetic resonance imaging as a cancer biomarker: consensus and recommendations. *Neoplasia*, 11(2):102–125.

- [149] Paragios, N., Ferrante, E., Glocker, B., Komodakis, N., Parisot, S., and Zacharaki, E. I. (2016). (hyper)-graphical models in biomedical image analysis.
- [150] Paragios, N. and Komodakis, N. (2014). Discrete visual perception. In *Pattern Recognition (ICPR), 2014 22nd International Conference on*, pages 18–25. IEEE.
- [151] Parisot, S., Duffau, H., Chemouny, S., and Paragios, N. (2012). Joint tumor segmentation and dense deformable registration of brain mr images. In *Medical Image Computing and Computer-Assisted Intervention–MICCAI 2012*, pages 651–658. Springer.
- [152] Parisot, S., Wells, W., Chemouny, S., Duffau, H., and Paragios, N. (2013). Uncertainty-driven efficiently-sampled sparse graphical models for concurrent tumor segmentation and atlas registration. In *Proceedings of the IEEE International Conference on Computer Vision*, pages 641–648.
- [153] Park, H., Bland, P. H., Hero III, A. O., and Meyer, C. R. (2005). Least biased target selection in probabilistic atlas construction. In *International Conference on Medical Image Computing and Computer-Assisted Intervention*, pages 419–426. Springer.
- [154] Park, S. C., Park, M. K., and Kang, M. G. (2003). Super-resolution image reconstruction: a technical overview. *Signal Processing Magazine, IEEE*, 20(3):21–36.
- [155] Patterson, D. M., Padhani, A. R., and Collins, D. J. (2008). Technology insight: water diffusion mri—a potential new biomarker of response to cancer therapy. *Nature Clinical Practice Oncology*, 5(4):220–233.
- [156] Perona, P. and Malik, J. (1990). Scale-space and edge detection using anisotropic diffusion. *IEEE Transactions on pattern analysis and machine intelligence*, 12(7):629–639.
- [157] Petrovic, V., Cootes, T., Twining, C., and Taylor, C. (2007). Simultaneous registration, segmentation and modelling of structure in groups of medical images. In *Biomedical Imaging: From Nano to Macro, 2007. ISBI 2007. 4th IEEE International Symposium on*, pages 1–4. IEEE.
- [158] Pierpaoli, C. (2010). Quantitative brain mri. *Topics in magnetic resonance imaging: TMRI*, 21(2):63.
- [159] Pižurica, A. and Philips, W. (2006). Estimating the probability of the presence of a signal of interest in multiresolution single- and multiband image denoising. *Image Processing, IEEE Transactions on*, 15(3):654–665.
- [160] Pluim, J. P., Maintz, J. A., and Viergever, M. A. (2003). Mutual-information-based registration of medical images: a survey. *IEEE transactions on medical imaging*, 22(8):986–1004.

- [161] Pohl, K. M., Fisher, J., Grimson, W. E. L., Kikinis, R., and Wells, W. M. (2006). A bayesian model for joint segmentation and registration. *NeuroImage*, 31(1):228–239.
- [162] Pohl, K. M., Fisher, J., Levitt, J. J., Shenton, M. E., Kikinis, R., Grimson, W. E. L., and Wells, W. M. (2005). A unifying approach to registration, segmentation, and intensity correction. In *International Conference on Medical Image Computing and Computer-Assisted Intervention*, pages 310–318. Springer.
- [163] Rajan, D. and Chaudhuri, S. (2003). Simultaneous estimation of super-resolved scene and depth map from low resolution defocused observations. *Pattern Analysis and Machine Intelligence, IEEE Transactions on*, 25(9):1102–1117.
- [164] Rao, A., Sanchez-Ortiz, G. I., Chandrashekara, R., Lorenzo-Valdés, M., Mohiaddin, R., and Rueckert, D. (2002). Comparison of cardiac motion across subjects using non-rigid registration. In *International Conference on Medical Image Computing and Computer-Assisted Intervention*, pages 722–729. Springer.
- [165] Reinhardt, J. M., Ding, K., Cao, K., Christensen, G. E., Hoffman, E. A., and Bodas, S. V. (2008). Registration-based estimates of local lung tissue expansion compared to xenon ct measures of specific ventilation. *Medical image analysis*, 12(6):752–763.
- [166] Roche, A. (2011). A four-dimensional registration algorithm with application to joint correction of motion and slice timing in fmri. *IEEE transactions on medical imaging*, 30(8):1546–1554.
- [167] Rother, C., Kohli, P., Feng, W., and Jia, J. (2009). Minimizing sparse higher order energy functions of discrete variables. In *Computer Vision and Pattern Recognition, 2009. CVPR 2009. IEEE Conference on*, pages 1382–1389. IEEE.
- [168] Rother, C., Kolmogorov, V., Lempitsky, V., and Szummer, M. (2007). Optimizing binary mrfs via extended roof duality. In *Computer Vision and Pattern Recognition, 2007. CVPR'07. IEEE Conference on*, pages 1–8. IEEE.
- [169] Roy, A. S., Gopinath, A., and Rangarajan, A. (2007). Deformable density matching for 3d non-rigid registration of shapes. In *International Conference on Medical Image Computing and Computer-Assisted Intervention*, pages 942–949. Springer.
- [170] Royuela-del Val, J., Cordero-Grande, L., Simmross-Wattenberg, F., Martín-Fernández, M., and Alberola-López, C. (2015). Nonrigid groupwise registration for motion estimation and compensation in compressed sensing reconstruction of breath-hold cardiac cine mri. *Magnetic resonance in medicine*.

- [171] Rudin, M. (2007). Imaging readouts as biomarkers or surrogate parameters for the assessment of therapeutic interventions. *European radiology*, 17(10):2441–2457.
- [172] Rueckert, D., Aljabar, P., Heckemann, R. A., Hajnal, J. V., and Hammers, A. (2006). Diffeomorphic registration using b-splines. In *Medical Image Computing and Computer-Assisted Intervention–MICCAI 2006*, pages 702–709. Springer.
- [173] Rueckert, D., Sonoda, L. I., Hayes, C., Hill, D. L., Leach, M. O., and Hawkes, D. J. (1999). Nonrigid registration using free-form deformations: application to breast mr images. *IEEE transactions on medical imaging*, 18(8):712–721.
- [174] Sagel, S. S., Weiss, E. S., Gillard, R. G., Hounsfield, G. N., Jost, R. G. T., Stanley, R. J., and Ter-pogossian, M. M. (1977). Gated computed tomography of the human heart. *Investigative Radiology*, 12(6):563–566.
- [175] Schnabel, J. A., Heinrich, M. P., Papież, B. W., and Brady, J. M. (2016). Advances and challenges in deformable image registration: From image fusion to complex motion modelling.
- [176] Seghers, D., D’Agostino, E., Maes, F., Vandermeulen, D., and Suetens, P. (2004). Construction of a brain template from mr images using state-of-the-art registration and segmentation techniques. In *International Conference on Medical Image Computing and Computer-Assisted Intervention*, pages 696–703. Springer.
- [177] Shakeri, M., Ferrante, E., Tsogkas, S., Lippe, S., Kadoury, S., Kokkinos, I., and Paragios, N. (2016a). Prior-based coregistration and cosegmentation. In *International Conference on Medical Image Computing and Computer-Assisted Intervention*, pages 529–537. Springer.
- [178] Shakeri, M., Lombaert, H., Lippé, S., and Kadoury, S. (2014). Group-wise shape analysis of the hippocampus using spectral matching. In *SPIE Medical Imaging*, pages 90340W–90340W. International Society for Optics and Photonics.
- [179] Shakeri, M., Tsogkas, S., Ferrante, E., Lippe, S., Kadoury, S., Paragios, N., and Kokkinos, I. (2016b). Sub-cortical brain structure segmentation using f-cnn’s. In *Biomedical Imaging (ISBI), 2016 IEEE 13th International Symposium on*, pages 269–272. IEEE.
- [180] Shanno, D. F. (1970). Conditioning of quasi-newton methods for function minimization. *Mathematics of computation*, 24(111):647–656.
- [181] Shannon, C. E. (2001). A mathematical theory of communication. *ACM SIGMOBILE Mobile Computing and Communications Review*, 5(1):3–55.
- [182] Shen, D. and Davatzikos, C. (2002). Hammer: hierarchical attribute matching mechanism for elastic registration. *IEEE transactions on medical imaging*, 21(11):1421–1439.

- [183] Shen, D. and Davatzikos, C. (2004). Measuring temporal morphological changes robustly in brain mr images via 4-dimensional template warping. *NeuroImage*, 21(4):1508–1517.
- [184] Shimizu, S., Shirato, H., Aoyama, H., Hashimoto, S., Nishioka, T., Yamazaki, A., Kagei, K., and Miyasaka, K. (2000). High-speed magnetic resonance imaging for four-dimensional treatment planning of conformal radiotherapy of moving body tumors. *International Journal of Radiation Oncology* Biology* Physics*, 48(2):471–474.
- [185] Shimony, S. E. (1994). Finding maps for belief networks is np-hard. *Artificial Intelligence*, 68(2):399–410.
- [186] Shirato, H., Shimizu, S., Kitamura, K., Nishioka, T., Kagei, K., Hashimoto, S., Aoyama, H., Kunieda, T., Shinohara, N., Dosaka-Akita, H., et al. (2000). Four-dimensional treatment planning and fluoroscopic real-time tumor tracking radiotherapy for moving tumor. *International Journal of Radiation Oncology* Biology* Physics*, 48(2):435–442.
- [187] Soatto, S. and Yezzi, A. J. (2002). Deformation deforming motion, shape average and the joint registration and segmentation of images. In *European Conference on Computer Vision*, pages 32–47. Springer.
- [188] Sotiras, A., Davatzikos, C., and Paragios, N. (2013). Deformable medical image registration: A survey. *Medical Imaging, IEEE Transactions on*, 32(7):1153–1190.
- [189] Sotiras, A., Komodakis, N., Glocker, B., Deux, J.-F., and Paragios, N. (2009a). Graphical models and deformable diffeomorphic population registration using global and local metrics. In *Medical Image Computing and Computer-Assisted Intervention–MICCAI 2009*, pages 672–679. Springer.
- [190] Sotiras, A., Komodakis, N., Langs, G., and Paragios, N. (2009b). Atlas-based deformable mutual population segmentation. In *Biomedical Imaging: From Nano to Macro, 2009. ISBI'09. IEEE International Symposium on*, pages 5–8. IEEE.
- [191] Spiclin, Ž., Likar, B., and Pernus, F. (2012). Groupwise registration of multimodal images by an efficient joint entropy minimization scheme. *IEEE Transactions on Image Processing*, 21(5):2546–2558.
- [192] Stegmann, M. B. and Larsson, H. B. (2003). Motion-compensation of cardiac perfusion mri using a statistical texture ensemble. In *International Workshop on Functional Imaging and Modeling of the Heart*, pages 151–161. Springer.
- [193] Stejskal, E. O. and Tanner, J. E. (1965). Spin diffusion measurements: spin echoes in the presence of a time-dependent field gradient. *The journal of chemical physics*, 42(1):288–292.

- [194] Stéphane, V., Samuel, B., Vincent, D., Joelle, G., Remy, P., Francois, G. G., and Jean-Pierre, T. (2013). Comparison of pet-ct and magnetic resonance diffusion weighted imaging with body suppression (dwibs) for initial staging of malignant lymphomas. *European journal of radiology*, 82(11):2011–2017.
- [195] Studholme, C. (2003). Simultaneous population based image alignment for template free spatial normalisation of brain anatomy. In *International Workshop on Biomedical Image Registration*, pages 81–90. Springer.
- [196] Studholme, C. and Cardenas, V. (2004). A template free approach to volumetric spatial normalization of brain anatomy. *Pattern Recognition Letters*, 25(10):1191–1202.
- [197] Studholme, C., Hill, D. L., and Hawkes, D. J. (1999). An overlap invariant entropy measure of 3d medical image alignment. *Pattern recognition*, 32(1):71–86.
- [198] Sundar, H., Litt, H., and Shen, D. (2009). Estimating myocardial motion by 4d image warping. *Pattern recognition*, 42(11):2514–2526.
- [199] Swerdlow, S. H. (2013). Lymphoma classification and the tools of our trade: an introduction to the 2012 uscap long course. *Modern Pathology*, 26:S1–S14.
- [200] Syeda-Mahmood, T., Wang, F., Beymer, D., London, M., and Reddy, R. (2007). Characterizing spatio-temporal patterns for disease discrimination in cardiac echo videos. In *International Conference on Medical Image Computing and Computer-Assisted Intervention*, pages 261–269. Springer.
- [201] Szeliski, R. (2006). Image alignment and stitching: A tutorial. *Foundations and Trends® in Computer Graphics and Vision*, 2(1):1–104.
- [202] Takahara, T., Imai, Y., Yamashita, T., Yasuda, S., Nasu, S., and Van Cauteren, M. (2004). Diffusion weighted whole body imaging with background body signal suppression (dwibs): technical improvement using free breathing, stir and high resolution 3d display. *Matrix*, 160(160):160.
- [203] Tanner, C., Schnabel, J. A., Chung, D., Clarkson, M. J., Rueckert, D., Hill, D. L., and Hawkes, D. J. (2000). Volume and shape preservation of enhancing lesions when applying non-rigid registration to a time series of contrast enhancing mr breast images. In *International Conference on Medical Image Computing and Computer-Assisted Intervention*, pages 327–337. Springer.
- [204] Taouli, B., Sandberg, A., Stemmer, A., Parikh, T., Wong, S., Xu, J., and Lee, V. S. (2009). Diffusion-weighted imaging of the liver: Comparison of navigator triggered and breathhold acquisitions. *Journal of Magnetic Resonance Imaging*, 30(3):561–568.
- [205] Thirion, J.-P. (1998). Image matching as a diffusion process: an analogy with maxwell’s demons. *Medical image analysis*, 2(3):243–260.

- [206] Tofts, P. S., Brix, G., Buckley, D. L., Evelhoch, J. L., Henderson, E., Knopp, M. V., Larsson, H. B., Lee, T.-Y., Mayr, N. A., Parker, G. J., et al. (1999). Estimating kinetic parameters from dynamic contrast-enhanced t₁-weighted mri of a diffusable tracer: standardized quantities and symbols. *Journal of Magnetic Resonance Imaging*, 10(3):223–232.
- [207] Tofts, P. S. and Kermode, A. G. (1991). Measurement of the blood-brain barrier permeability and leakage space using dynamic mr imaging. 1. fundamental concepts. *Magnetic resonance in medicine*, 17(2):357–367.
- [208] Tu, H.-K., Matheny, A., Goldgof, D. B., and Bunke, H. (1995). Left ventricular boundary detection from spatio-temporal volumetric computed tomography images. *Computerized Medical Imaging and Graphics*, 19(1):27–46.
- [209] Twining, C. J., Cootes, T., Marsland, S., Petrovic, V., Schestowitz, R., and Taylor, C. J. (2005). A unified information-theoretic approach to groupwise non-rigid registration and model building. In *Biennial International Conference on Information Processing in Medical Imaging*, pages 1–14. Springer.
- [210] Twining, C. J., Marsland, S., and Taylor, C. J. (2004). Groupwise non-rigid registration: The minimum description length approach. In *BMVC*, pages 1–10.
- [211] Veeraraghavan, H., Do, R. K., Reidy, D. L., and Deasy, J. O. (2015). Simultaneous segmentation and iterative registration method for computing adc with reduced artifacts from dw-mri. *Medical physics*, 42(5):2249–2260.
- [212] Vercauteren, T., Pennec, X., Perchant, A., and Ayache, N. (2008). Symmetric log-domain diffeomorphic registration: A demons-based approach. In *International Conference on Medical Image Computing and Computer-Assisted Intervention*, pages 754–761. Springer.
- [213] Vercauteren, T., Pennec, X., Perchant, A., and Ayache, N. (2009). Diffeomorphic demons: Efficient non-parametric image registration. *NeuroImage*, 45(1):S61–S72.
- [214] Vilanova, J. C. and Barceló, J. (2008). Diffusion-weighted whole-body mr screening. *European journal of radiology*, 67(3):440–447.
- [215] Viola, P. and Wells III, W. M. (1997). Alignment by maximization of mutual information. *International journal of computer vision*, 24(2):137–154.
- [216] Wachinger, C. and Navab, N. (2012). Entropy and laplacian images: Structural representations for multi-modal registration. *Medical image analysis*, 16(1):1–17.
- [217] Wachinger, C. and Navab, N. (2013). Simultaneous registration of multiple images: Similarity metrics and efficient optimization. *IEEE transactions on pattern analysis and machine intelligence*, 35(5):1221–1233.

- [218] Wainwright, M. J., Jaakkola, T. S., and Willsky, A. S. (2005). Map estimation via agreement on trees: message-passing and linear programming. *IEEE transactions on information theory*, 51(11):3697–3717.
- [219] Wang, C., Komodakis, N., and Paragios, N. (2013). Markov random field modeling, inference & learning in computer vision & image understanding: A survey. *Computer Vision and Image Understanding*, 117(11):1610–1627.
- [220] Wang, C., Teboul, O., Michel, F., Essafi, S., and Paragios, N. (2010a). 3d knowledge-based segmentation using pose-invariant higher-order graphs. In *International Conference on Medical Image Computing and Computer-Assisted Intervention*, pages 189–196. Springer.
- [221] Wang, F., Syeda-Mahmood, T., Vemuri, B. C., Beymer, D., and Rangarajan, A. (2009a). Closed-form jensen-renyi divergence for mixture of gaussians and applications to group-wise shape registration. In *International Conference on Medical Image Computing and Computer-Assisted Intervention*, pages 648–655. Springer.
- [222] Wang, F., Vemuri, B., and Syeda-Mahmood, T. (2009b). Generalized l2-divergence and its application to shape alignment. In *International Conference on Information Processing in Medical Imaging*, pages 227–238. Springer.
- [223] Wang, F. and Vemuri, B. C. (2005). Simultaneous registration and segmentation of anatomical structures from brain mri. In *International Conference on Medical Image Computing and Computer-Assisted Intervention*, pages 17–25. Springer.
- [224] Wang, F., Vemuri, B. C., Rangarajan, A., and Eisenschenk, S. J. (2008). Simultaneous nonrigid registration of multiple point sets and atlas construction. *IEEE transactions on pattern analysis and machine intelligence*, 30(11):2011–2022.
- [225] Wang, Q., Wu, G., Yap, P.-T., and Shen, D. (2010b). Attribute vector guided groupwise registration. *NeuroImage*, 50(4):1485–1496.
- [226] Wells, W. M., Viola, P., Atsumi, H., Nakajima, S., and Kikinis, R. (1996). Multi-modal volume registration by maximization of mutual information. *Medical image analysis*, 1(1):35–51.
- [227] Wierzbicki, M., Drangova, M., Guiraudon, G., and Peters, T. (2004). Validation of dynamic heart models obtained using non-linear registration for virtual reality training, planning, and guidance of minimally invasive cardiac surgeries. *Medical Image Analysis*, 8(3):387–401.
- [228] Willett, C. G., Linggood, R. M., Stracher, M. A., Goitein, M., Doppke, K., Kushner, D. C., Morris, T., Pardy, J., and Carroll, R. (1987). The effect of the respiratory cycle on mediastinal and lung dimensions in hodgkin's disease. implications for radiotherapy gated to respiration. *Cancer*, 60(6):1232–1237.

- [229] Wollny, G., Kellman, P., Santos, A., and Ledesma-Carbayo, M. J. (2012). Automatic motion compensation of free breathing acquired myocardial perfusion data by using independent component analysis. *Medical image analysis*, 16(5):1015–1028.
- [230] Wollny, G., Ledesma-Carbayo, M. J., Kellman, P., and Santos, A. (2010). Exploiting quasiperiodicity in motion correction of free-breathing myocardial perfusion mri. *IEEE Transactions on Medical Imaging*, 29(8):1516–1527.
- [231] Woods, R. P., Grafton, S. T., Holmes, C. J., Cherry, S. R., and Mazziotta, J. C. (1998). Automated image registration: I. general methods and intrasubject, intramodality validation. *Journal of computer assisted tomography*, 22(1):139–152.
- [232] Wu, G., Jia, H., Wang, Q., and Shen, D. (2011). Sharpmean: groupwise registration guided by sharp mean image and tree-based registration. *NeuroImage*, 56(4):1968–1981.
- [233] Wu, G., Wang, Q., Jia, H., and Shen, D. (2012a). Feature-based groupwise registration by hierarchical anatomical correspondence detection. *Human brain mapping*, 33(2):253–271.
- [234] Wu, G., Wang, Q., Shen, D., Initiative, A. D. N., et al. (2012b). Registration of longitudinal brain image sequences with implicit template and spatial-temporal heuristics. *Neuroimage*, 59(1):404–421.
- [235] Wu, G., Yap, P.-T., Wang, Q., and Shen, D. (2010). Groupwise registration from exemplar to group mean: extending hammer to groupwise registration. In *2010 IEEE International Symposium on Biomedical Imaging: From Nano to Macro*, pages 396–399. IEEE.
- [236] Wyatt, P. P. and Noble, J. A. (2003). Map mrf joint segmentation and registration of medical images. *Medical Image Analysis*, 7(4):539–552.
- [237] Xiaohua, C., Brady, M., Lo, J. L.-C., and Moore, N. (2005). Simultaneous segmentation and registration of contrast-enhanced breast mri. In *Biennial International Conference on Information Processing in Medical Imaging*, pages 126–137. Springer.
- [238] Xiong, G., Chen, C., Chen, J., Xie, Y., and Xing, L. (2012). Tracking the motion trajectories of junction structures in 4d ct images of the lung. *Physics in medicine and biology*, 57(15):4905.
- [239] Xue, Z., Wong, K., and Wong, S. T. (2010). Joint registration and segmentation of serial lung ct images for image-guided lung cancer diagnosis and therapy. *Computerized Medical Imaging and Graphics*, 34(1):55–60.
- [240] Yeo, B. T., Sabuncu, M. R., Desikan, R., Fischl, B., and Golland, P. (2008). Effects of registration regularization and atlas sharpness on segmentation accuracy. *Medical image analysis*, 12(5):603–615.

- [241] Yezzi, A., Zollei, L., and Kapur, T. (2001). A variational framework for joint segmentation and registration. In *Mathematical Methods in Biomedical Image Analysis, 2001. MMBIA 2001. IEEE Workshop on*, pages 44–51. IEEE.
- [242] Yezzi, A., Zöllei, L., and Kapur, T. (2003). A variational framework for integrating segmentation and registration through active contours. *Medical Image Analysis*, 7(2):171–185.
- [243] Yigitsoy, M., Wachinger, C., and Navab, N. (2011). Temporal groupwise registration for motion modeling. In *Information Processing in Medical Imaging*, pages 648–659. Springer.
- [244] Yin, Y., Hoffman, E. A., Ding, K., Reinhardt, J. M., and Lin, C.-L. (2010). A cubic b-spline-based hybrid registration of lung ct images for a dynamic airway geometric model with large deformation. *Physics in medicine and biology*, 56(1):203.
- [245] Ying, S., Wu, G., Wang, Q., and Shen, D. (2014). Hierarchical unbiased graph shrinkage (hugs): a novel groupwise registration for large data set. *NeuroImage*, 84:626–638.
- [246] Yoshikawa, K., Nakata, Y., Yamada, K., and Nakagawa, M. (2004). Early pathological changes in the parkinsonian brain demonstrated by diffusion tensor mri. *Journal of Neurology, Neurosurgery & Psychiatry*, 75(3):481–484.
- [247] Zhang, L., Chédotel, C., and Bousquet, G. (2010). Group-wise motion correction of brain perfusion images. In *2010 IEEE International Symposium on Biomedical Imaging: From Nano to Macro*, pages 832–835. IEEE.
- [248] Zheng, Y., Maidment, A. D., and Gee, J. C. (2010). Accurate registration of dynamic contrast-enhanced breast mr images with robust estimation and linear programming. In *2010 IEEE International Symposium on Biomedical Imaging: From Nano to Macro*, pages 536–539. IEEE.
- [249] Zitova, B. and Flusser, J. (2003). Image registration methods: a survey. *Image and vision computing*, 21(11):977–1000.
- [250] Zöllei, L., Learned-Miller, E., Grimson, E., and Wells, W. (2005). Efficient population registration of 3d data. In *International Workshop on Computer Vision for Biomedical Image Applications*, pages 291–301. Springer.
- [251] Zöllner, F. G., Sance, R., Rogelj, P., Ledesma-Carbayo, M. J., Rørvik, J., Santos, A., and Lundervold, A. (2009). Assessment of 3d dce-mri of the kidneys using non-rigid image registration and segmentation of voxel time courses. *Computerized Medical Imaging and Graphics*, 33(3):171–181.

Titre : Recalage d'images déformées en groupe pour l'estimation du mouvement en imagerie médicale 4D

Mots-clés : champ aléatoire de Markov, recalage d'image en groupe, diffusion, imagerie médicale, résonance magnétique, biomarqueurs d'imagerie

Résumé : La présente thèse propose des méthodes pour l'estimation du mouvement des organes d'un patient au travers de l'imagerie tomographique. Le but est la correction du mouvement spatio-temporel sur les images médicales tomographiques. En tant que paradigme expérimental, nous considérons le problème de l'estimation du mouvement dans l'imagerie IRM de diffusion, une modalité d'imagerie sensible à la diffusion des molécules d'eau dans le corps. Le but de ces travaux de thèse est l'évaluation des patients atteints de lymphome, car l'eau diffuse différemment dans les tissus biologiques sains et dans les lésions. L'effet de la diffusion de l'eau peut être mieux représenté par une image paramétrique, grâce au coefficient de diffusion apparente (image à ADC), créé sur la base d'une série d'images DWI du même patient (séquence d'images 3D), acquises au moment de la numérisation. Une telle image paramétrique a la possibilité de devenir un biomarqueur d'imagerie d'IRM et de fournir aux médecins des informations complémentaires concernant l'image de FDG-PET qui est la méthode d'imagerie de base pour le lymphome et qui montre la quantité de glucose métabolisée.

Nos principales contributions sont au nombre de trois. Tout d'abord, nous proposons une méthode de recalage d'image déformable en groupe spécialement conçue pour la correction de mouvement dans l'IRM de diffusion, car elle est guidée par un modèle physiologique décrivant le processus de diffusion qui se déroule lors de l'acquisition de l'image. Notre méthode détermine une image à ADC de plus grande précision en termes de représentation du gradient de la diffusion des molécules d'eau par rapport à l'image correspondante obtenue par pratique courante ou par d'autres méthodes de recalage d'image non basé sur un modèle. Deuxièmement, nous montrons qu'en imposant des contraintes spatiales sur le calcul de l'image à ADC, les tumeurs de l'image peuvent être encore mieux caractérisées en les classant dans les différentes catégories liées à la maladie. Troisièmement, nous montrons qu'une corrélation entre DWI et FDG-PET doit exister en examinant la corrélation entre les caractéristiques statistiques extraites par l'image à ADC lisse découlant de notre méthode du recalage d'image déformable et les scores de recommandation sur la malignité des lésions, donnés par des experts basés sur une évaluation des images FDG-PET correspondantes du patient.

Title: Deformable Group-wise Image Registration for Motion Estimation in 4D Medical Imaging

Keywords: Markov Random Fields, group-wise registration, diffusion, Medical Imaging, Magnetic Resonance, imaging biomarkers

Abstract: This doctoral thesis develops methods to estimate patient's motion, voluntary and involuntary (organs' motion), in order to correct for motion in spatiotemporal tomographic medical images. As an experimental paradigm we consider the problem of motion estimation in Diffusion-Weighted Magnetic Resonance Imaging (DWI), an imaging modality sensitive to the diffusion of water molecules in the body. DWI is used for the evaluation of lymphoma patients, since water diffuses differently in healthy tissues and in lesions. The effect of water diffusion can be better depicted through a parametric map, the so-called apparent diffusion coefficient (ADC map), created based on a series of DW images of the same patient (3D image sequence), acquired in time during scanning. Such a parametric map has the potentiality to become an imaging biomarker in DWI and provide physicians with complementary information to current state-of-the-art FDG-PET imaging reflecting quantitatively glucose metabolism.

Our contributions are three fold. First, we propose a group-wise deformable image registration method especially designed for motion correction in DWI, as it is guided by a physiological model describing the diffusion process taking place during image acquisition. Our method derives an ADC map of higher accuracy in terms of depicting the gradient of the water molecules' diffusion in comparison to the corresponding map derived by common practice or by other model-free group-wise image registration methods. Second, we show that by imposing spatial constraints on the computation of the ADC map, the tumours in the image can be even better characterized in terms of classifying them into the different types of the disease. Third, we show that a correlation between DWI and FDG-PET should exist by examining the correlation between statistical features extracted by the smooth ADC map derived by our deformable registration method, and recommendation scores on the malignancy of the lesions, given by experts based on an evaluation of the corresponding FDG-PET images of the patient.

